Dilepton spectroscopy with HADES

Vom Fachbereich Physik
der Technischen Universität Darmstadt

zur Erlangung des Grades
eines Doktors der Naturwissenschaften
(Dr. rer. nat.)

genehmigte Dissertation von

Jaroslav Bielčík

aus Kokava nad Rimavicou

Darmstadt 2004
D 17

Referent: Prof. Dr. P. Braun-Munzinger
Koreferent: Prof. Dr. W. Nörenberg

Tag der Einreichung: 23. January 2004
Tag der Prüfung: 29. April 2004

Declaration of Originality

This doctoral thesis contains the results of my research carried out in the GSI in Darmstadt between January 1999 and December 2003.

Excluding introductory parts the research described in this thesis is original unless where an explicit reference is made to work of others. I further state that no part of this thesis or anything substantially the same has been submitted for any qualification other than the degree Dr.rer.nat. at the Technical University in Darmstadt.

3.8.2004 Jaroslav Bielčík

Abstract

The dilepton spectrometer HADES (**H**igh **A**cceptance **Die**lectron **S**pectrometer) has started recently its operation at the SIS accelerator in Gesellschaft für Schwerionenforschung (GSI), Darmstadt, and several commissioning beamtimes have been performed. In this work, the analysis of data measured in November 2001, where collisions of ^{12}C projectiles on a carbon target at a beam energy of 2 AGeV have been studied, is presented. About 35 millions of events with multiplicity of charged particles larger or equal to one have been selected for the analysis.

The main motivation of this work is to reconstruct the invariant-mass spectrum of the produced $\mathrm{e}^+\mathrm{e}^-$ pairs. The main sources of dilepton production are π^0 decays. The highest branching ratio has: a) $\pi^0 \rightarrow \gamma + \gamma$ (BR = 98.8 %) and b) $\pi^0 \rightarrow \gamma + e^+ + e^-$ (BR = 1.2%). In matter the produced photons can convert to $\mathrm{e}^+\mathrm{e}^-$ pairs: $\gamma \rightarrow e^+ + e^-$. Due to small opening angles ($\langle \alpha_{\mathrm{e}^+\mathrm{e}^-} \rangle = 2.4°$) most of the conversion pairs are not resolved as two individual tracks in the detectors in the front of the HADES magnet. These unresolved pairs contribute as single tracks to the combinatorial background.

Full-scale simulations based on the UrQMD model have been performed to study the detector properties and analysis performance. The lepton tracks have been identified. The topology of the MDC hits has been studied for lepton tracks and unresolved close pairs tracks. A method of close pairs rejection has been developed. The analysis steps for lepton and dilepton identification are discussed in detail, and spectra for each analysis step are presented. The reconstructed $\mathrm{e}^+\mathrm{e}^-$ spectrum from measured data is compared with the spectrum from the analysis of simulated data.

Kurzfassung

Das Dielektronenspektrometer HADES (**H**igh **A**cceptance **Die**lectron **S**pectrometer) ist vor kurzem am Schwerionensynchrotron (SIS) der Gesellschaft für Schwerionenforschung (GSI) in Darmstadt in Betrieb genommen worden und es wurden mehrere Inbetriebnahmestrahlzeiten durchgeführt. In der vorliegenden Arbeit wird die Untersuchung von C+C Daten, gemessen im November 2001 bei einer Einschussenergie von 2 AGeV präsentiert. Für die Datenanalyse wurden Ungefähr 35 Millionen Ereignisse mit der Multiplizität von geladenen Teilchen grösser oder gleich eins ausgewählt.

Die Hauptmotivation für diese Arbeit ist die Rekonstruktion des invariantes Massenspektrums von erzeugten $\mathrm{e}^+\mathrm{e}^-$ -Paaren. Die Hauptquellen für die Dileptonproduktion sind π^0 Zerfälle. Das höchste Verzweigungsverhältnis hat: a) $\pi^0 \rightarrow \gamma + \gamma$ (BR = 98.8 %) und b) $\pi^0 \rightarrow \gamma + e^+ + e^-$ (BR = 1.2%). So erzeugten Photonen können dann in der Materie in $\mathrm{e}^+\mathrm{e}^-$ Paare konvertieren: $\gamma \rightarrow e^+ + e^-$. Aufgrund deren kleiner Öffnungswinkel ($\langle \alpha_{\mathrm{e}^+\mathrm{e}^-} \rangle = 2.4°$) sind die meisten Konversionspaare in Detektoren vor dem HADES Magnetfeld nicht als zwei einzelne Spuren aufgelöst. Diese nicht aufgelösten Paare tragen dann als einzelne Spuren zum kombinatorischem Untergrund bei.

Die Simulationen sind aufgebaut auf dem UrQMD Modell und wurden durchgeführt, um die Eigenschaften des Detektorsystems und der Analysesoftware zu studieren. Die Leptonenspuren wurden identifiziert. Die Topologie der MDC Hits wurde für Leptonenspuren und nicht aufgelöste naheliegenden Paarspuren untersucht. Eine Methode für die Unterdrückung naheliegende Paarspuren wurde entwickelt. Die einzelnen Analyseschritte für die Lepton- und Dileptonerkennung

sind ausführlich diskutiert und für jeden Analyseschritt werden die Massenspektren präsentiert. Das $\mathrm{e^+e^-}$ Massenspektrum, rekonstruiert aus den gemessen Daten, wird mit dem aus der Analyse der simulierten Daten verglichen.

Contents

List of Figures

List of Tables

1

Introduction

The topic of this work, the study of nuclear matter under the conditions of high density and high temperature, has been during the last decades one of the central topics of nuclear physics. This became possible with heavy ion collisions that allow to study properties of such systems in laboratory conditions. This form of matter plays an important role in astrophysical processes. For example, the stability of neutron stars and the mechanism of supernova explosions are strongly related to the properties of dense and hot nuclear matter. Shortly after the big bang (a few μs) the universe also passed through such a hadronic phase. The density and temperature of the matter of the universe in this very early stage was so high that it was in a phase of free quarks and gluons, a so called quark gluon plasma. During the following expansion it came to hadronisation, and mesons and baryons have been created in hot medium.

Nuclear matter under normal conditions is a multiparticle system that consists primarily of protons and neutrons that interact with each other via strong interaction. The density of normal nuclear matter is $\rho_0 = 0.17$ fm^{-3}. The theory of the strong interaction is quantum chromodynamics (QCD). The interaction between quarks, that are bound in the nucleons (confinement) and can not be observed as free particles, is realized via gluon exchange. The coupling constant of the strong interaction depends on the momentum transfer in the process and only at very high energies does the coupling gets week enough so that perturbation theory can be applied. Indeed this is not possible at lower energies. For the description in this region various effective models have been developed in which the mesonic and baryonic degrees of freedom are taken into account, fulfilling the basic symmetries of QCD. For example chiral symmetry is fulfilled in the limit of massless u, d and s quarks, but is spontaneously broken for quarks with nonzero mass in the vacuum. The partial restoration of chiral symmetry in the hot and dense matter environment has consequences for the hadron properties. The quark condensate expectation value decreases with increasing nuclear matter temperature and density as it is suggested by several models, for a review see [1]. It was also suggested that the decrease in the condensate in nuclear matter can be related to the hadron massses by a simple scaling law [2].

From the experimental point of view, the most suitable hadron probe to observe the partial restoration of the chiral symmetry turns out to be vector mesons in general and the ρ meson in particular. The vector mesons have short lifetime and decay partially (mostly for ρ because of τ_ρ=1.3 fm/c) during the hot and dense phase of the heavy ion collision. Additionally the interactions of the vector mesons embedded in nuclear matter have been studied by various hadronic models based on effective hadron-meson Lagrangians and mean field theories [3]. The vector meson spectral functions change in the nuclear medium. An important role plays the coupling to particle-hole excitations in nuclear matter. The calculations predict a dramatic increase of the ρ meson width and decrease the ρ meson effective mass even at normal nuclear density.

The most probable decay of vector mesons is via hadronic channels. With a branching ratio of typically $\approx 10^{-4}$ vector mesons decay also into dilepton channel. The $\mathrm{e}^+\mathrm{e}^-$ pairs are an ideal probe to study the vector meson properties, because they leave the collision zone without strong interactions and they convey undistorted information on the in-medium mass and width of vector mesons. Several experiments focused during the last years on the measurement of the dilepton signal from heavy ion collisions. The DLS at BEVALAC has been a pioneering experiment and delivered the first $\mathrm{e}^+\mathrm{e}^-$ spectra for beam energies of 1-2 AGeV. The other $\mathrm{e}^+\mathrm{e}^-$ experiment was CERES that over the last decade operated at the SPS. Both experiments observed a dilepton excess of pair invariant masses over expectations from hadronic decays in the region of 200-600 $\mathrm{MeV/c^2}$. The experiments NA38/NA50 and NA38/HELIOS-3 at SPS investigated dilepton production via dimuon decays and observed similar effects. The High Acceptance DiElectron Spectrometer (HADES) has been proposed to measure $\mathrm{e}^+\mathrm{e}^-$ pairs at SIS (SchwerIonenSynchrotron) energies of 1-2 AGeV as a second generation dilepton spectrometer. Due to its high acceptance, high invariant mass resolution, and high data taking rate, it offers the unique possibility for intensive and systematic study of in-medium changes of the vector mesons.

The HADES spectrometer has been built and it was under commissioning and recently came to operation at GSI (Die Gesellschaft für SchwerIonenforschung) Darmstadt. The results from the commissioning beamtime from November 2001 are presented in this work. The measured collision system was C+C at 2 AGeV. The analysis strategy for lepton track identification was developed and leptons were identified. An invariant mass spectrum of $\mathrm{e}^+\mathrm{e}^-$ pairs was reconstructed. The limited statistics allows investigation of the most dominant part of the spectrum from π^0 and η decays. The combinatorial background was reconstructed with like-sign pairs method. A method to suppress the combinatorial background based on rejection of unresolved close pairs in the detectors in the front of the HADES magnet was also investigated and applied. Full scale simulations of HADES detector response were performed. The simulated data were analyzed and compared with measured ones. The results were discussed with respect to DLS data.

1.1 Relativistic heavy ion collisions

Heavy ion collisions allow via the kinetic energy of the projectile creation compressed and hot nuclear matter. The energy of the projectile is large enough to overcome the Coulomb potential barrier between the nuclei. Then in the volume where both nuclei overlap the collision zone is created for a limited time. The *Fig. 1.1* shows schematically an example of a simulation of a heavy collision within the UrQMD model for a central Au+Au collision at an energy of 2 AGeV. The gold nucleus consists of 79 protons and 118 neutrons. If one of the nuclei is in the laboratory system at rest then the energy of the nuclei in center of mass (c.m.) system corresponds to 0.41 AGeV. The collision of the projectile and target nuclei is characterized by the projectile energy in AGeV (energy per nucleon), the radii of the nuclei (related to the nucleon number) and an impact parameter. The impact parameter is the shortest distance between the centers of the projectile and target nuclei. With decreasing impact parameter, the overlap collision zone enlarges and the number of nucleons that take part in the collision (participants) increases.

The central Au+Au collision on *Fig. 1.1* is shown in 3 successive phases. The first phase is the deceleration of the target and projectile nuclei. In this phase bremsstrahlung is emitted and the density of the overlap zone increases up to $3\rho_0$. This takes up to 5 fm/c (1 fm/c = 3.3·10^{-24} s). In the second phase the system stays in a dense phase for time up to 15 fm/c. In the case of thermalization a temperature of the system of about 100 MeV is reached. In this phase same of the nucleons are excited to resonances. Mostly $\Delta(1232)$ are produced and they decay with pion emission. The excitation of the higher energetic resonances leads to the production of heavier mesons. The pions (and also other mesons), nucleons and resonances can interact further with each other in multistep processes. The production of mesons for which the threshold energy of the production is larger than the energy of the nucleons from collision, can take place in this dense phase via multistep processes. The third phase is the expansion of the system. During this phase, baryons and mesons scatter and interact, therefore their observables change. The photons and leptons from particle decays are not influenced by strong interaction and leave the collision zone with undistorted observables that carry unique information from the dense phase.

The kinetic energy of the projectile nucleus is transformed during the collision to compression energy (system gets dense), heat (system gets hot), but also to exciting internal degrees of freedom of the nucleons. The baryonic resonances are created. In the energy region of SIS, the most populated resonance is $\Delta(1232)$ with mass of 1232 MeV/c^2. The main decay channel of the $\Delta(1232)$ is almost 100% going back to nucleons N and π:

$$N + N \rightarrow N + \Delta \rightarrow N + N + \pi \tag{1.1}$$

As shown in [5] the pion density may reach up to 30% of baryon density at 2 AGeV, which implies that up to 30% of the nucleons are excited to the Δ resonance during the dense phase of the collision. In the following the π can collide with nucleons, producing resonances that decay subsequently. During the heavy ion collision several cycles of emissions and absorptions of π take place. The channel given by Eq. (1.1) is the main pro-

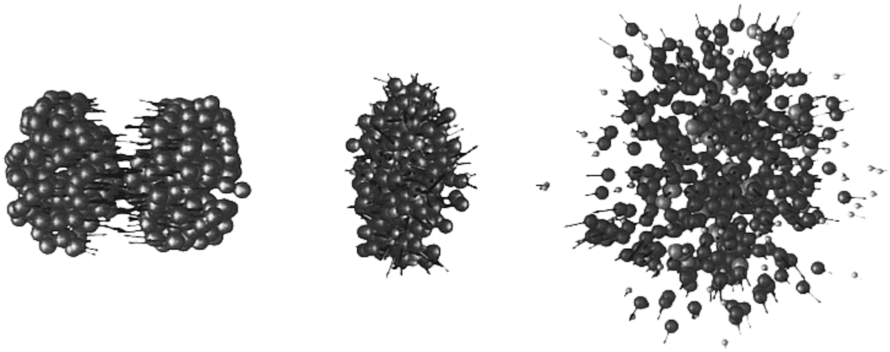

Figure 1.1: The simulation of a central Au+Au collision according to the transport model QMD [4]. The collision shown is 3 time steps of $3 \cdot 10^{-23}$ s in center of mass system. The nuclei are shown shortly before the collision (left), Lorentz contracted (the single nucleons are also contracted, that is not shown on the picture). The arrows show the vectors of the nucleon momenta. In the second phase (middle) of the collision the nuclei overlap and dense and energetic fireball is created. The last phase is the expansion of the system. The dark large balls are nucleons, the large light balls are resonances and small the light balls are mesons.

duction channel for pions. When the particles leave the reaction zone without any further interactions, the system freezes-out. The mesons of higher nominal masses are produced by decays of higher lying resonances. The η meson with mass m_η = 547 MeV/c^2 is produced in the decay of $N^*(1535)$. This is the lowest lying resonance that has significant decay ($30-55\%$) to η [6].

$$N+N \rightarrow N+N^*(1535) \rightarrow N+N+\eta \tag{1.2}$$

The resonance $N^*(1535)$ also can be producedin multistep inelastic processes, when a nucleon collides with other resonance $N+B^* \rightarrow N+N^*(1535)$. The baryon resonances work as an energy reservoir. After several inelastic collisions also very high lying resonances can be produced even in a collision with low beam energy. For η production in middle and heavier mass collision systems meson-baryon collisions also are possible:

$$\Delta+\pi \rightarrow N^*+N \tag{1.3}$$

and:

$$N+\pi \rightarrow N^*(1535) \rightarrow N+\eta. \tag{1.4}$$

In similar way like π, also η can be reabsorbed and produces $N^*(1535)$ which can decay to another channel: [6] :

$$N^*(1535) \rightarrow N+\pi \tag{1.5}$$

or it can interact with another nucleon:

$$N^*(1535)+N \rightarrow N+N. \tag{1.6}$$

There are several other additional resonances that decay to η, also for example $N^*(1650)$ that decays with $3-16\%$ to $N\eta$ channel or $N^*(1720)$ with 16% $N\eta$ channel [6]. But these higher lying resonances do not play a role for η production at SIS energies because of their relatively low yield. For the production of the vector meson ω with large mass m_ω = 782MeV/c^2 one has to excite even heavier resonances. Because of the isospin conservation it should be N^*. In the UrQMD model the production of the ω meson is described via the $N^*(1900)$ resonance with 55% probability to decay to channel $N+\omega$ [4]. The ρ meson is produced mainly through the channel $\pi+\pi\rightarrow\rho$ and ϕ through channel $K^++K^-\rightarrow\phi$. The threshold energies for production of various types of the particles in heavy ion collision at 1-2 AGeV are listed in *Tab. 1.1*. These are the threshold energies for production of the particles at rest in the c.m. system. For the production of the particles with higher momentum, higher energy is needed. The production of particles is also possible with energies under the threshold, because of the Fermi motion of the nucleons, that is about 270 MeV/c. The Fermi energy increases the free energy available for production of the new particles in the system. The subthreshold particle production is also possible through multistep processes, as described above, or by the reduction of the effective mass of the nucleons M_N^* or the particle effective mass, that reduces the energy necessary for particle production in simple N+N collision.

Particle	Process N+N $\rightarrow$	E_{thr} [AGeV]	$E_{thr}^{c.m.}$ [GeV]
π	N+N+ π	0.29	0.140
η	N+N+η	1.26	0.550
ρ	N+N+ρ	1.86	0.770
ω	N+N+ω	1.89	0.782
ϕ	N+N+ϕ	2.59	1.019

Table 1.1: The threshold energies needed to produce the particle in single NN collision $N+N\rightarrow N+N+particle$. $E_{thr}^{c.m.}$ is the kinetic energy of the pair needed for particle production. E_{thr} is the threshold energy of the beam projectiles in lab. system for particle production.

This work studies the reconstruction of the $\mathrm{e^+e^-}$ pairs produced during heavy ion collision and in the reactions in and around the target. The π^0 decays are the dominant source of dileptons. The $\mathrm{e^+e^-}$ pairs from γ conversion can be largely rejected due to their topology. Other important sources are the η and the Δ. The π and η mesons have long lifetimes and they decay outside of the dense and hot phase. The π are considered to be Goldstone bosons and they are not expected to be modified substantially in the nuclear medium [7]. The $\mathrm{e^+e^-}$ pairs from π^0 Dalitz can be used for normalization of the dilepton spectrum. The lifetime of the vector mesons ρ, ω, ϕ is short enough that they decay inside the dense phase of the collision. The changes of their properties can therefore be reconstructed via detected $\mathrm{e^+e^-}$ pairs from their decays.

1.2 Overview of dilepton sources in heavy ion collisions.

In the heavy ion collisions at SIS energies the main dilepton sources are electromagnetic decays of hadrons and products of their collisions. In the low invariant dilepton mass region ($M_{inv} < 1GeV$) dominant mechanisms are Dalitz decays ($A \rightarrow Be^+e^-$) of the neutral mesons π^0, η, ω and $\Delta(1232)$ resonance:

$$\pi^0, \eta \rightarrow \gamma e^+ e^-, \tag{1.7}$$

$$\omega \rightarrow \pi^0 e^+ e^-, \tag{1.8}$$

$$\Delta \rightarrow e^+ e^- N. \tag{1.9}$$

At their mass peaks the direct decays ($A \rightarrow e^+e^-$) of the vector mesons ρ, ω and ϕ are expected to dominate the spectrum.

$$\rho, \omega, \phi \rightarrow e^+ e^- \tag{1.10}$$

At low beam energies, pn bremsstrahlung also contributes significantly to the spectrum. Other sources like Dalitz decays of heavier resonances, $pp, \pi N$ bremsstrahlung are considered to be negligible [8]. The *Tab.1.2* summaries the properties of the main dilepton sources and branching ratios (BR) to the dilepton channels according [6]

			Mass	Decay width		Product			e^+e^-
Source	J^P	I	[MeV/c^2]	[MeV/c^2]	[fm/c]		[%]	e^+e^-	BR
Dalitz-Decays of the pseudoscalar mesons									
π^0	0^-	1	135	0.78	251	$\gamma\gamma$	98.8	γe^+e^-	1.2%
η	0^-	0	547	0.001	$\gg 30$	$\gamma\gamma$	39.4	γe^+e^-	0.5%
Direct decays of the vector mesons									
ρ	1^-	1	771	149	1.3	$\pi^+\pi^-$	100	e^+e^-	$4.6 \cdot 10^{-5}$
ω	1^-	0	782	8.44	23.4	$\pi^+\pi^-\pi^0$	89	e^+e^-	$7 \cdot 10^{-5}$
ϕ	1^-	0	1019	4.26	44.4	K^+K^-:	49	e^+e^-	10^{-5}-10^{-4}
Δ-Dalitz-Decay									
Δ	$(3/2)^+$	3/2	1232	115	1.7	Nπ	>99	N e^+e^-	$4 \cdot 10^{-3}$
Proton-Neutron-Bremsstrahlung: pn → pn e^+e^-									

Table 1.2: The most important sources of dileptons in heavy ion collisions with decay width, decay rates *in Vacuum*. $J =$Spin, $P =$Parity, $I =$Isospin.

1.3 The DLS puzzle

The DLS collaboration measured e$^+$e$^-$ spectra from collisions produced at beam energies of 1-2 AGeV. Therefore their results are of the interest for HADES program. Two generations of the data have been presented. The first generation of the data [9] from p+Be, Ca+Ca and Nb+Nb collisions has suffered to unrecognized trigger inefficiencies and it has been suggested not to compare these results with theoretical models. The first generation of the DLS data was reasonably described by several models [10–13] without incorporating any medium effects. These various models in similar way describe the dilepton spectrum up to 400 $\mathrm{MeV/c^2}$ primarily by hadronic sources such as the Dalitz decays of π^0, Δ, η and pn bremsstrahlung, whereas for masses larger than 400 $\mathrm{MeV/c^2}$ the dominant channel is $\pi^+\pi^-$ annihilation and direct decays of vector mesons.

The second generation of the data from Ca+Ca, C+C, He+Ca and d+Ca reactions at 1 AGeV [14] has been measured after improvement of the DLS trigger and the data analysis was corrected for dead time losses. The new data set shows a considerable increase in the cross section, more than factor 6-7 in comparison to the previous data set. Therefore, the new spectrum can not be explained by hadronic sources without any medium effects.

There have been several attempts to explain the second generation DLS data in similar way as CERES data at SPS energies. In [15] Hadron String Dynamics (HSD) transport model [16] has been used to study the dilepton production at BEVALAC energies. In particular, the contribution from direct decays of ρ mesons produced from πN scattering through $N^*(1520)$ has been also taken into account. It dominates the spectrum from 350-750 $\mathrm{MeV/c^2}$. The model fails to describe the DLS data in region 200-500 $\mathrm{MeV/c^2}$. Allowing the reduction of the ρ mass in dense matter and keeping the baryons unchanged, enhances dilepton production from other ρ production channels, but reduces the production of ρ via $N^*(1520)$ channel and leads to a total dilepton spectrum similar to that without dropping hadron masses and fail to describe the data.

Another approach within HSD model [17] employed momentum dependent ρ spectral functions that included the pion modifications in the nuclear medium as well as the polarization of the ρ meson due to resonant ρN scattering. The DLS data can not be described in region 150-500 $\mathrm{MeV/c^2}$ with 'free' spectral functions. Discrepancy between data and calculations is about factor of 3-5. The description of the data is slightly improved when including the in-medium ρ spectral functions, but in the region 150-400 $\mathrm{MeV/c^2}$ the new DLS data are underestimated at least by a factor of 3. The speculations of the possible scaling of the η mass by the Brown-Rho law [2] can lead to significant enhancement of the η production in heavy ion collisions. The DLS data would be well described in this scenario. However, the dropping η mass scenario does not yield the observed m_T scaling observed by TAPS (see also *Chapter 3*). Also η photon production as it is discussed in [17] excludes a dramatic change of the η properties in medium.

In [18] the dilepton production in heavy ion collisions has been studied in framework of the extended QMD transport model for the inclusion of nucleon resonances with masses up to 2 AGeV. At small invariant masses the experimental data are underestimated by factor of 2-3. The in-medium effects has been discussed concerning the problem of quantum interference. The proposed scheme of decoherence improved the agreement with the DLS data in low region but the magnitude of this effect is not sufficient to describe the data.

The calculation of the DLS spectra within UrQMD model [19] underestimates the

DLS dilepton spectrum for heavy ion collisions in range from 150-600 $\mathrm{MeV/c^2}$ by factor 2-3. Additional artificial enhancement of the η yield by factor 10 (C+C) and factor 20 (Ca+Ca) would lead to description of the data. The simple scaling of the vector meson masses within UrQMD is also not sufficient to describe the DLS heavy ion data.

The TAPS collaboration has measured the π^0 and η production in C+C and Ca+Ca at 1 AGeV at SIS. The contribution of the π^0 Dalitz and η Dalitz to the DLS spectra has been estimated [20], see *Fig1.2*. The good agreement of the spectra for masses up to 150 $\mathrm{MeV/c^2}$, dominated by π^0 Dalitz , is obtained. However, in the mass range 150-500 $\mathrm{MeV/c^2}$, dominated by η Dalitz , the DLS data exceed the calculated TAPS η Dalitz yield by a factor 4-10 in all systems. Additional physical processes should be accounted for in order to describe the DLS dilepton yield.

Thus, unlike the enhancement of low invariant mass dileptons observed in heavy ion collisions at SPS, the DLS result can be explained neither by changes of hadrons in medium, nor by changes of the ρ spectral functions and remains a puzzle. It is one of the first tasks of the HADES experimental program to revisit the DLS spectrum.

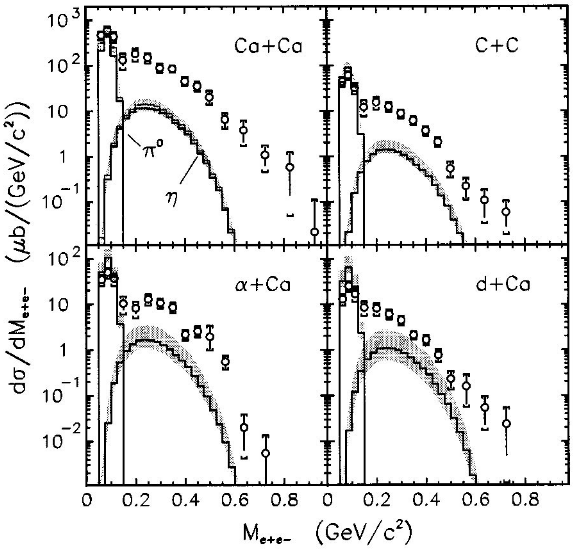

Figure 1.2: The invariant mass spectrum of e^+e^- pairs measured for Ca+Ca, C+C, He+Ca and d+Ca reactions at 1 AGe with DLS spectrometer (black circles). The contribution of the π^0 Dalitz and η Dalitz decays as it was measured by TAPS filtered with DLS response is shown as solid line.

2

Description of the HADES spectrometer

2.1 Design requirements

The HADES experimental program is focusing on the study of the properties of neutral vector mesons via rare dilepton decays. This put several constrains to design of the spectrometer:

- **Large acceptance:** The reconstruction of the $\mathrm{e}^{+}\mathrm{e}^{-}$ pairs requires the acceptance of the both leptons in the pair. HADES covers has full acceptance in azimuthal angles (except the dead space due magnet coils) and in polar angles it covers space from 18° to 85°. Total pairs acceptance is 40%.

- **Lepton trigger:** For selection of the collisions with enhanced dilepton content, dedicated 3 level dilepton trigger has been design. The full design rejection power is 10^{4}.

- **High counts rates:** The operation with high beam intensities of 10^{8} particles per second require tape speed of 10^{6} minimum bias events per second.

- **High invariant mass resolution:** 1% invariant mass resolution for dileptons in omega mass region is required to disentangle expected mass and width changes

- **Lepton identification:** A separation of the rare lepton tracks from dominated hadrons is needed.

From the momenta of the $\mathrm{e}^{+}\mathrm{e}^{-}$ pairs emitted from collision zone, the invariant mass spectrum of the dileptons can be constructed:

$$M_{e^{+}e^{-}}c^{2} = \sqrt{(E_{e^{+}} + E_{e^{-}})^{2} - (\overrightarrow{p}_{e^{+}}c + \overrightarrow{p}_{e^{-}}c)^{2}} \tag{2.1}$$

Where $E_{e^\pm}$ is total energy and $p_{e^\pm}$ is momentum of electron resp. positron in laboratory system and c is velocity of light. The Eq. 2.1 can be for leptons with large energy $E_{e^\pm} \gg m_{e^\pm}$ =0.511 MeV/c^2 simplified to:

$$M_{e^+e^-}c^2 \cong 2\sin\frac{\alpha}{2}\sqrt{p_{e^+}cp_{e^-}c}, \tag{2.2}$$

where α is opening angle of the pair.

The decay width of the ω meson with mass 782 $\mathrm{MeV/c^2}$ is about 8$\mathrm{MeV/c^2}$, see *Tab. 1.2*. In the same part of the invariant mass spectrum is also ρ meson with width about 150 $\mathrm{MeV/c^2}$. For ability to measure the changes of the width and peak of the invariant mass it is important that invariant mass resolution in this region is about 8/782 1%. The invariant mass resolution depends on momentum and pair opening angle resolution:

$$\frac{\Delta M_{e^+e^-}}{M_{e^+e^-}} \cong \sqrt{(\frac{\Delta p_{e^+}}{2p_{e^+}})^2 + (\frac{\Delta p_{e^-}}{2p_{e^-}})^2 + (\frac{\Delta\alpha}{2\tan\frac{\alpha}{2}})^2}. \tag{2.3}$$

Therefore momentum and pair opening angle resolution should be maximized. For large opening angles is the contribution of the angle resolution to invariant mass resolution negligible [21]. The momentum resolution of the leptons depends on the position resolution of the detectors before and after magnetic field. For necessary 1% invariant mass resolution, position resolution better than 100μm is needed.

HADES spectrometer, see *Fig. 2.1*, consists of 6 identical sectors. It contains RICH (Ring Imaging Cherenkov) detector for lepton identification, a set of 4 MDC (Multiwire Drift Chambers) places in the front and after magnetic field created by coils of superconducting magnet. From the outer side are detectors covered with META (Multiplicity and Electron Trigger Array). The META is build from TOFINO and PreSHOWER detectors (for polar angles up to $45°$) and TOF (Time of Flight) detector (for angles above $45°$). The META brings additional lepton identification and it is part of the first level trigger. A two diamond detectors (START, VETO) are used for triggering of the events.

2.2 Start and veto detectors

During the experiment it is necessary to read out the information from the electronics of the data acquisition for all detectors short after the moment when the heavy ion collision took place in the target. As a start signal for the acquisition of the HADES spectrometer signals from fast diamond START and VETO detectors are used, see *Fig. 2.2* .

START and VETO detectors are two identical 8-strip diamond detectors of an octagonal shape, which are placed 75 cm downstream and 75 cm upstream of the HADES target, respectively. The diamond detectors are polycrystalline carbon substrates synthesized using the Chemical Vapor Decomposition (CVD) method to grow in controlled way. The signal is read from the strips after amplification of the signal with low noise broad band amplifiers. If there is a signal on the START detector strip and no signal on three

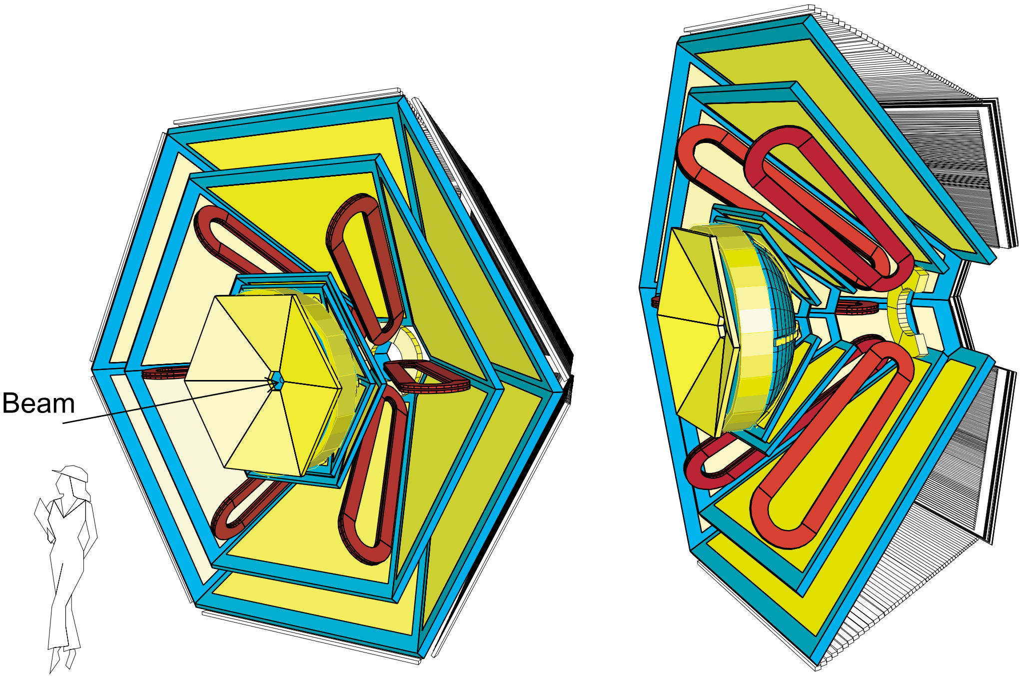

(a) Frontview 6 HADES-Sectors (b)Sideview; the beam comes from left

Figure 2.1: A 3-dimensional artistic view of the HADES spectrometer.

corresponding VETO detector strips, a collision took place, because the products of the collision scatter with an angle larger than one needed to hit the strips in the veto detector in a case of straight trajectory.

The downstream VETO detector vetoes all particles with no reaction with target nuclei and provides thus a start signal with the rate of more than 10^7 particles/s. The widths of the strips are optimized such that a coincidence of one start strip with three veto strips is sufficient for the veto efficiency of 96.5 %. The outer dimensions of the detectors are 25 mm and 15 mm matching the beam spot in this position. The multiple scattering and secondary reactions is kept at low level because of the detectors thickness of 100 μm. The time resolution of the start detector was determined to be below 50 ps for C+C collisions at 1.5 AGeV. The start detector gives a reference for the measurement of the time of flight between the target and the TOF and TOFINO detectors.

2.3 Ring Imaging Cherenkov Detector

The RICH detector [22], see *Fig. 2.3* is designed to identify $\mathrm{e}^+\mathrm{e}^-$ pairs in the high multiplicity environment of up to 200 charged particles created in a central heavy ion collision

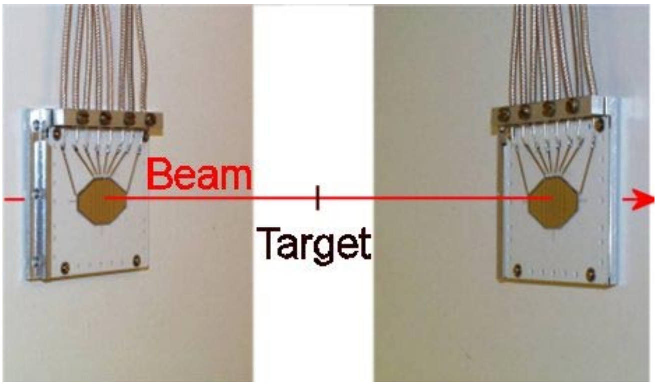

Figure 2.2: The START and VETO diamond detectors placed 75cm down and up stream the beam line.

and at the rate of $10^5\mathrm{s}^{-1}$. The RICH detector is placed around the target to achieve the full polar acceptance. In addition, it is a part of the trigger system (LVL2 trigger), to be able to select only collisions that produced a lepton or $\mathrm{e}^+\mathrm{e}^-$ pair in the HADES acceptance and therefore also corresponding signal in RICH. The HADES RICH detector is built to be a hadron blind. Only particles with very high velocities produce a signal. This is fulfilled only for electrons and positrons.

The detector consists of three main parts: a) a gas radiator, where a fast particle passing the radiator emits Cherenkov photons, b) a spherical vacuum ultra-violet mirror (VUV mirror) that reflects photons onto photon-detector, c) the photon-detector detecting reflected photons. Each electron that passes the radiator and it produces photons, gives finally on the pad plane a signal in the shape of rings with a constant diameter of 5.5 cm as it will be explained later. The signal from pads is analyzed and rings are reconstructed. From the position of the ring on the photon-detector it is possible to determine the position of the electron where it passed the mirror and assuming that particle comes from the target also polar θ and azimuthal ϕ angles of the track.

2.3.1 Cherenkov effect

When a charged particle is moving with the speed larger than the velocity of light in medium passes dielectricum, excited atoms of the material emit photons with visible frequency in a form of shock wave. The emitted photons build a cone with an angle θ_{cher} with respect to the particle trajectory. This velocity is given by

$$v > v_{th} = \frac{c}{n} \tag{2.4}$$

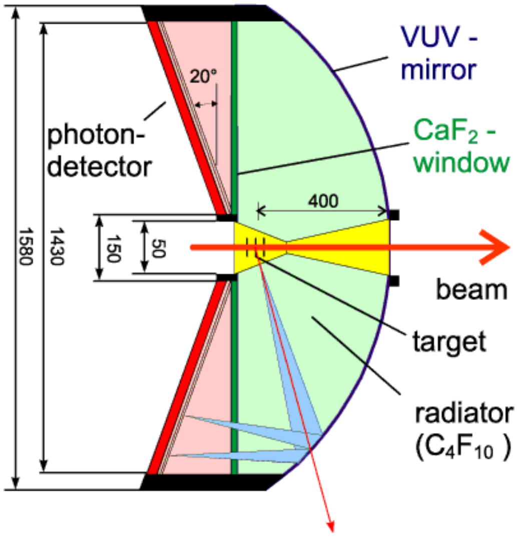

Figure 2.3: Schematic cross section of the HADES RICH. The spherical mirror reflects Cherenkov photons from radiator to a segmented CsI-based photon detector upstream the target (the size is given in [mm]).

or

$$\beta > \beta_{th} = \frac{1}{n} = \sqrt{1 - \frac{1}{\gamma_{th}^2}}, \tag{2.5}$$

where n is the refractive index of the medium and v_{th} the threshold velocity - the phase velocity of light in a given medium. The threshold can be expressed also using the second equation and the Lorentz-factor γ_{th}. The RICH detector is a threshold detector. It can be blind to specific particles by selecting the proper material of radiator with particular refractive index n, such that particles that do not fulfill the previous conditions are not seen. The angle of the photon emission with respect to the particle trajectory is

$$\cos\theta_{cher} = \frac{1}{\beta n(\omega)}. \tag{2.6}$$

This angle depends on the speed of the particle and the frequency ω of the emitted light. The formula above is a simplification for the infinite radiating medium.

One can choose such materials with the refraction index n that all slow particles will not fulfill the threshold condition and mostly only electrons (positrons) will produce the Cherenkov light. The slow hadrons do not produce a signal. The electrons produced in heavy ion collisions have velocities close to the speed of light and $\beta \approx 1$. The number of photons with wavelengths from λ_1 to λ_2 per unit length emitted in the radiator is given by

$$\frac{dN}{dx} = 2\pi Z^2 \alpha \sin^2\theta_{cher} \int\limits_{\lambda_1}^{\lambda_2} \frac{d\lambda}{\lambda^2}. \tag{2.7}$$

The number of photons that are emitted in the radiator is larger than number of detected photons in a photo-detector due to an absorption of the Cherenkov photons in the radiator and in the gas of the photon-detector and due to the limited reflectivity of the mirror. Number of the detected photons is expressed as

$$N_{det} = N_0 \frac{l_{rad}}{\gamma_{th}^2}, \tag{2.8}$$

where l_{rad} is the length which the particle passed in the radiator and N_0 is called the figure of merit of the detector and contains various instrumental parameters of the detector. The figure of merit of the HADES RICH contains detector specific values of transmission and efficiencies, i.e.

$$N_0 = \frac{4\pi^2\alpha^2}{hc} T_{det}\, \varepsilon_e \int_{\lambda_1}^{\lambda_2} T_{rad}\, R\, T_F\, \varepsilon_q \frac{d\lambda}{\lambda^2}, \tag{2.9}$$

where T_{det} is the transmission of the wire chamber of the photon detector, ε_e the efficiency of the wire chamber of the photon detector for a single electron, $R(\lambda)$ the reflectivity of the mirror, $T_{rad}(\lambda)$ the transmissivity of the radiator, $T_F(\lambda)$ the transmissivity of the window between radiator and photon detector, and $\varepsilon_q(\lambda)$ is the quantum efficiency of photon-detector. The overall performance of the HADES RICH reads figure of merit $N_0 = 70 - 80cm^{-1}$ that corresponds to 8-16 detected photons per ring depending on the length of trajectory in radiator.

2.3.2 RICH components

A schematic view of the RICH detector is shown in *Fig. 2.3*. Leptons with the momenta of our interest 100 MeV/c < p$_e$ < 1500 MeV/c will produce Cherenkov light in gaseous C_4F_{10} radiator. The light is reflected from the carbon mirror (in the commissioning beam-times some parts of the mirror are produced from glass) and focused on the position sensitive photon detector with a CsI photon convertor. The radiator gas and the gas of the photon detector are separated by a thin CaF$_2$ window. All materials were chosen to have optimal efficiency and transmission for photons in the ultra-violet region of 145 nm$<\lambda<$ 210 nm.

2.3.3 Radiator gas

One of the most important parts of Cherenkov detectors is the radiator gas, where the production of Cherenkov light takes place. The radiator gas should have a high transmissivity for the UV light and a small threshold factor γ_{thr}. The Cherenkov radiator is C_4F_{10}. This gas has the index of refraction of n = 1,00151 which corresponds to the Cherenkov radiation threshold γ_{thr} = 18.3. Only particles with the velocity $\beta >$ 0.9985 produce Cherenkov light. The gas is transparent down to wavelengths λ = 145 nm and does not show any significant scintillation from charged particles. The radiator container is built up from an CaF_2 entrance window of the photon-detector and a forward shell made of 0.4 mm carbon fiber laminate. The gas operates under the pressure of 1000–1200 hPa. The minimal electron momentum to produce a signal is 9.3 MeV/c. For pions this minimal momentum is 2.55 GeV/c and for protons 17.1 GeV/c. This makes the detector hadron blind. The photons are emitted under an angle of 3.15° with respect to the track and with a very small dispersion because all electrons have velocity β close to 1. Therefore, the corresponding uncertainty in the emission angle is less than 0.05°. The yield of the Cherenkov photons for one charge particle track depends on the length of the trajectory in the radiator. This length varies in HADES RICH from 38 to 68 cm depending on the track polar angle. But on average the lepton with the momentum of 100 MeV/c produces about 110 photons in the radiator.

2.3.4 VUV mirror

Cherenkov photons produced in the radiator are reflected to the up-stream position of the photon-detector by a spherical mirror. The material of this mirror should fulfill several constraints. It should have a high reflectivity, a minimal multiple scattering and photon conversion probability. A design based on pure carbon reaches these requirements. It has low $Z = 6$ and that is the reason for the small multiple scattering and photon conversion probability. The density of the pure carbon is low, $\rho_{carbon} \approx$ 1.45 g/cm^3 and the radiation length is large - $X_0 \approx$ 28 cm. The mirror has a high reflectivity in the vacuum ultraviolet (VUV) wavelength region 150 nm $< l <$ 250 nm. The average reflectivity obtained is $R \sim$ 80%. The mirror has a radius with a curvature $R =$ 871 mm and a diameter $D =$ 1.50 m. For technical reasons it is segmented into 6 sectors with 3 panels each. The panels are machined to a thickness of $d =$ 2 mm, polished, and coated with a thin Al+MgF_2 layer. The spherical shape of the mirror is such that photons emitted under the same azimuthal angle are reflected to the same point on the photon detector. Therefore, all photons from one trajectory build a shape of a ring on the photon-detector. In reality it is an ellipse but the pad sizes of the photon-detector correct for this effect.

During the beam-time in November 2001 not all panels of the mirror were ready due to their difficult production and therefore a part of the mirror was built from glass with the density $\rho_{glass} \approx$ 2.45 g/cm^3 and the radiation length $X_0 \approx$ 14 cm. The glass mirror has a thickness d = 1.9 mm. The stability of the glass mirror material is not as good as of carbon and therefore the shape of rings can be influenced.

2.3.5 Photon detector

The photon detector consists of six multi-wire proportional chambers (MWPC) with three wire layers and a cathode pad plane (see *Fig. 2.4*). CH_4 is used as the detector gas for its good VUV transmission down to λ = 142 nm. The chamber is operated at U_A = 2550 V with a gain of G = 10^5. The Cherenkov photons enter through the CaF_2 window and are converted to photo-electrons in a solid CsI photocathode evaporated onto the pad plane.

The electrons are drifted to the anode wire where an avalanche effect sets in. The mirror charge induces the signal on the pads. The chamber is photo sensitive only in the VUV wavelength region 145 nm$< l <$ 210 nm. The detection efficiency for single photo electrons is $\epsilon > 95\%$. The size of the 28272 pads varies from A = 7 x 6.6 mm^2 (inner part) to A = 4 x 6.6 mm^2 (outer part) to compensate the spherical aberration of the mirror.

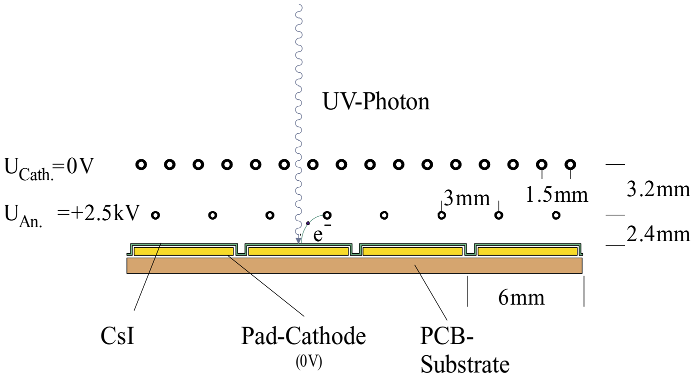

Figure 2.4: Schematic view of photo sensitive multiwire proportional chamber (MWPC) with a pad cathode covered by CsI

2.3.6 CaF_2 entrance window

It is necessary to separate the radiator gas and the gas of the photon detector by an entrance window. This separation should be done with a specific material which has a high transition in the VUV wavelength region. The entrance window of the photon detector was produced from CaF_2. CaF_2 has been chosen due to its high transmission in the VUV wavelength region. At λ = 140 nm the average transmission is T = 70% .The window has a diameter of D = 1.5 m and thickness of 5 mm. It is assembled from altogether 64 single crystals of hexagonal shape. All the crystals have been extensively polished and individually checked for their VUV transmission.

2.3.7 Ring finding in RICH detector

There are two methods used for ring reconstruction in RICH [23]. After the cleaning of the isolated noise hits on the pad plane, the hit clusters are identified and labeled. The first of the method, the pattern matrix method shown in *Fig. 2.5*, is an algorithm that overlays a mask of the ring image on the pad plane. The mask is divided in cells with positive or negative weight. The cells correspond to the pads on the pad plane. The positive values of the weight in the mask correspond to the ring. The pad plane is scanned with the mask and for each pad the measured charge is multiplied with the weight on the mask and then all these products from all pads are summed up to one number A_{pm} (pattern matrix parameter). This parameter is used as selection criterion. If the A_{pm} is larger than a given threshold value a ring is found. True rings have larger A_{pm} values than fake ones.

The second used method is Hough transformation shown schematically in *Fig. 2.6*. This is a mathematical transformation of the space of pad combinations (rings) on the pad plane into space of the points (centers of the rings). Each combination of the three pads is fitted with ring of the given radius and the center of the ring gives a point in transformed space. The pads from a true ring will be transformed to the points that lay close to each other. If the centers are filled into a histogram, than a peak is built in a place of the center of the ring. The ring finding problem is modified to simpler task of peak finding.

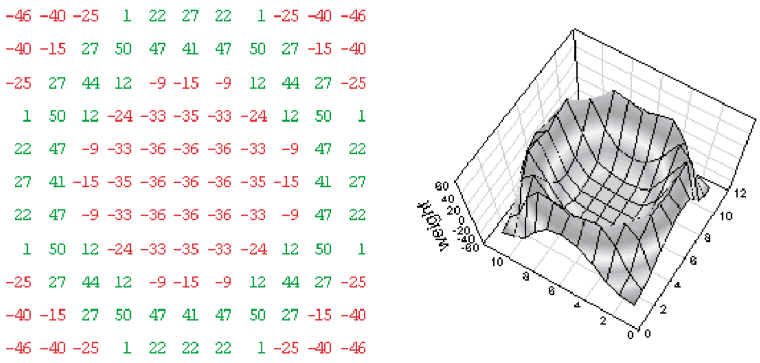

-46	-40	-25	1	22	27	22	1	-25	-40	-46
-40	-15	27	50	47	41	47	50	27	-15	-40
-25	27	44	12	-9	-15	-9	12	44	27	-25
1	50	12	-24	-33	-35	-33	-24	12	50	1
22	47	-9	-33	-36	-36	-36	-33	-9	47	22
27	41	-15	-35	-36	-36	-36	-35	-15	41	27
22	47	-9	-33	-36	-36	-36	-33	-9	47	22
1	50	12	-24	-33	-35	-33	-24	12	50	1
-25	27	44	12	-9	-15	-9	12	44	27	-25
-40	-15	27	50	47	41	47	50	27	-15	-40
-46	-40	-25	1	22	22	22	1	-25	-40	-46

Figure 2.5: Principle of pattern matrix method for ring finding.

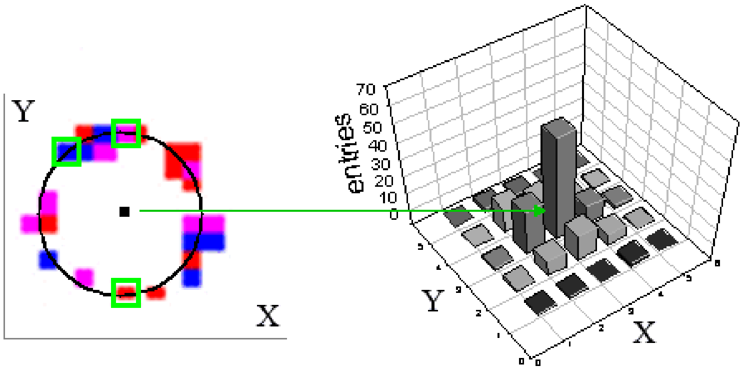

Figure 2.6: Principle of the hough transformation method for ring finding.

2.4 MDC detector

As has been explained in the beginning of this chapter only good momentum resolution of the lepton tracks allows to obtain precise invariant mass measurement of the $\mathrm{e}^+\mathrm{e}^-$ pairs. The tracking of the particles in HADES in the front and behind magnetic field is done with a set of 4 MDC detectors in each of six sectors, see *Fig. 2.8*.

2.4.1 Principle of the drift chambers

The drift chamber is a gaseous detector designed to measure the trajectory of the charged particles. The main used physics phenomenon in the drift chamber is ionization of the gas when charged particle passes it. The crossing particle ionizes the gas, kicking one or several electrons from atoms. These electrons are called primary electrons. The primary electrons have enough energy to interact with the other molecules in the gas and secondary electrons are emitted, until primary electrons loose completely their energy during these collisions. For He gas the energy of 25 eV is necessary to free an electron from an atom. The gas is put in the magnetic field and electrons drift to anode and produce a signal.

The energy loss of a particle per unit length is expressed by the Bethe-Bloch formula [6]:

$$-\left(\frac{dE}{dx}\right) = (4\pi N_A r_e^2 m_e c^2)\frac{Z}{A}\frac{z^2}{\beta^2}\left[\frac{1}{2}ln\frac{2m_e c^2\beta^2\gamma^2 T_{max}}{I^2} - \beta^2 - \frac{\delta}{2}\right], \tag{2.10}$$

where $\beta = \frac{v}{c}$, $\gamma = \frac{1}{1-\beta^2}$, N_A is the Avogadro constant, r_e the classic electron radius, $m_e c^2$ mass energy of the electron, Z atomic number, A atomic mass of absorber, T_{max} is the maximum kinetic energy that can be imparted to a free electron in a single collision,I mean excitation energy, δ density effects correction to ionization energy loss.

From Eq. 2.10 we can see that the ionization energy loss is proportional to the electron density in medium, to the square of the projectile charge and to the 1/velocity of the projectile particle.

The energy loss, see *Fig. 2.7* decreases as $1/\beta^2$ with increasing momentum of particle, until minimum ionization is reached around $\beta\gamma$= 3-4. After reaching its minimum, the energy loss rises logarithmically up to the constant value called Fermi plateau. The energy loss in the minimum is $\frac{dE}{\rho dx} \sim$ 2 MeVcm^2/g.

Along the track of passing particle, primary electrons are produced. The secondary electrons are produced in the vicinity of primary electrons and small clusters are built and they drift to the anode wire. The signal is read from the anode wires.

2.4.2 HADES drift chambers

The HADES tracking system was designed to fulfill the following requirements. It should provide a) good position resolution (especially in the direction where particle trajectories

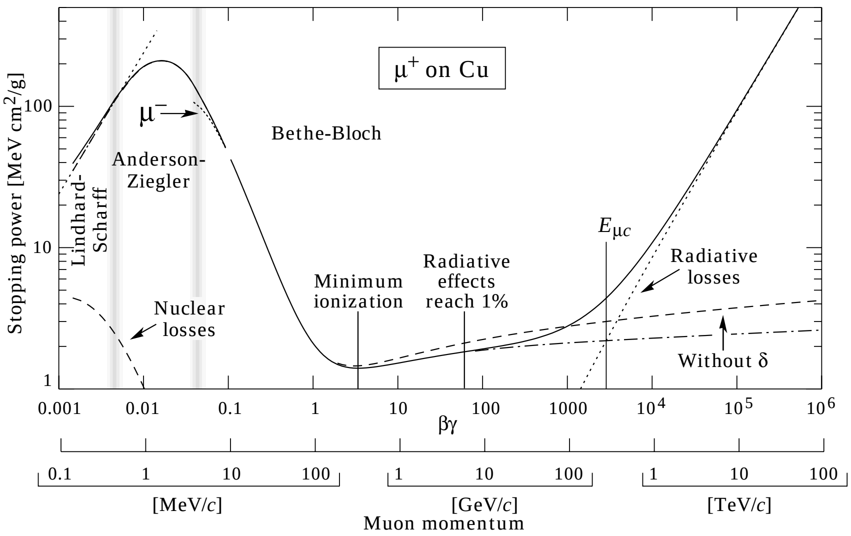

Figure 2.7: The energy loss (stopping power) for positive muons in copper as a function of β, γ [6].

are bent by the magnetic field), b) it should be built from low mass materials to minimize the multiple scattering of electrons, c) it should provide ability for a good two-track resolution to reduce the combinatorial background, d) it should be able to handle high particle multiplicities up to 200 charged particles for central Au+Au collisions, and e) last but not least, it should cover a large acceptance, therefore the frames were reduced to minimum and read out electronics was placed to this tight zone.

For the tracking of the charged particles in HADES, four modules of MDC (modules 0-3 or I-IV) are placed in each of six sectors of the spectrometer. Two of them are placed in the front of the magnetic field and the other two behind the magnetic field. The arrangement of the modules in the sector is demonstrated in *Fig. 2.8.* The chambers in the front of the magnetic field are called inner modules and those on the outer side of the magnet are called outer modules. This setting allows an independent position determination before and after the magnetic field. This is very important for determination of angle of kick that particle undergoes in the magnetic field. The precise determination of the position of the track before and after the magnet is directly related to the precision of the momentum determination.

The chambers cover full acceptance in the azimuthal angle and in the polar angle they cover range from 18° to 85°. The module sizes range from 88 cm x80 cm to 280 cm x 230 cm (height times larger baseline). The width of the frames that hold the wires was chosen such that the frames overlap with zone generated by the cages of 6 superconducting coils and therefore they do not reduce additionaly acceptance in azimuthal angle.

The tracks with the shortest trajectory between the target and the hit in MDC module

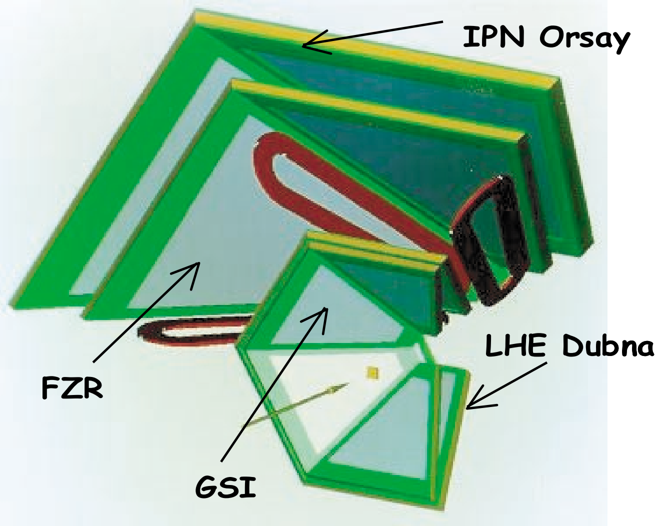

Figure 2.8: The arrangement of the tracking system in one sector. Tracking system consists of 4 drift chamber modules and one coil of the magnet toroid.

are the tracks that are perpendicular to the plane of the wires in the module. This minimum distance from the target to module 0 is 56 cm and to module 3 is 166 cm. The separation of the modules 0 and 1 varies from 10 cm to 30 cm, because of an inclination angle between them. The modules 2 and 3 are parallel with a constant separation of 30 cm.

A chamber module is composed of six independent layers of sense and field wires and seven cathode planes surrounding them. The wires in each layer are rotated with respect to the other layers with some angle to optimize the space resolution. The orientation of the wires is as following +40°, -20°, +0°, -0°, +20°, -40° as it is shown on *Fig. 2.9*. Two inner 0° layers are shifted with respect to each other by a half of the wire separation.

The sense wires are grounded to potential 0 V, the field and cathode wires have potential -1850 V. The cathode and field wires build around each sense wire a drift cell. The structure of the drift cells for 3 layers of wires is shown in *Fig. 2.10*. The plane defined by the drift cell is perpendicular to the wire layers. The cell sizes varies from 5x5 mm^2 to 14x10 mm^2 for the modules 0 to 3 in order to achieve a constant granularity. The total number of the drift cells is 27000. Because of the small dimensions of the drift cells, the maximum drift length for the largest cells is 17 mm. Selected material for the field and cathode wires was bare aluminum and for sense wires with gold vapored tungsten, to reach the goal to build the low mass chambers. The diameters of the wires are 100 μ m for field, 80 μm for cathode and 20 μm for sense wires. The wires are glued to the Stesalit frames, where they are soldered to the electrical connections of read out. The Stesalit frames are glued together and bolted to the aluminum frames.

In the HADES drift chambers, He-Isobutane mixture in the ratio of 60:40 has been

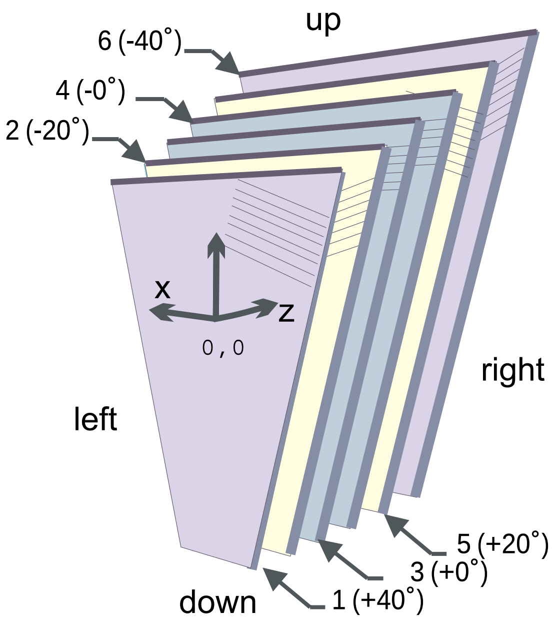

Figure 2.9: The schema of the MDC module with six layers. The wires in each layer have different orientations to achieve the optimal resolution in y direction.

used as an ionization gas. The gas volume is closed by 12 μm thick aluminized Mylar foils. When charged particles pass the drift cell about 35 clusters/cm are produced. In each cluster are 2-3 electrons. These ionization electrons drift in the electric field towards the sense wire. They produce additional secondary electrons. The positive ions drift to cathodes. The electric field is formed by potentials on the wires and it has been simulated by the GARFIELD simulations in [24]. In *Fig. 2.11* one can see the GARFIELD simulation of the passage of the charged particle through the cell under 30°. Few field lines (red) show the structure of the electric field. Because of the inhomogeneous field close to the sense wire and the edge of the cell, the trajectories are not straight lines. The clusters created at different places in the cell arrive to the sense wire at different time. The isochrone connects the places in the cell from where is the drift time to the sense wire constant. When the electrons arrive close to the sense wire, they come to a region with a very strong field gradient. They accelerate and produce additional secondary electrons. This leads to an avalanche effect. MDC works in the proportional mode, where the charge of the electron avalanche is proportional to the original charge in the electron cluster. The total gain factor of the HADES drift-chambers is $2\text{-}3{\cdot}10^5$ [25]. The avalanche region starts about 50 μm from the sense wire and the avalanche lives about 1 ns. During the avalanche the atoms of the gas are excited and emit later high energetic photons. These photons can by photo-effect eject from cathodes additional photo-electrons, which can drift to the sense wire and initiate an additional avalanche. This would made the measure-

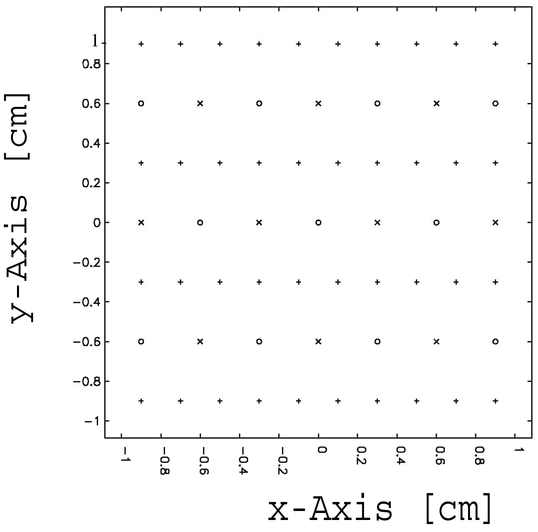

Figure 2.10: The cross section of the 3 layers of the MDC module, with sense wires, cathodes and field wires. o= sense wires, += cathode wires,x=field wires.

ment of next particle impossible. To avoid this, Isobutane is added to the noble He gas of the HADES chambers. Isobutane works as a quencher. Vibration and rotation modes of Isobutane molecules absorb the produced photons. Then is this energy distributed in elastic collisions.

Since the signal amplitude depends on the deposited charge, it is in principle possible to observe differences between various particle species, because the particles with different $\beta\gamma$ factor have different energy loss. For example e^+/e^- with momenta larger than 100 MeV/c have 15% larger energy loss than pions with the same momentum.

The signal from the wire is read out by a TDC (time-digital-convertor). The signal is read only if it crosses some minimal value set as a TDC threshold. The time between the TDC signal and the common-stop-signal (from delayed time from the START detector) is called in the HADES analysis software $time1$. TDC delivers also a second time, $time2$, when the TDC threshold is crossed again. TDC can work in two modes, either leading and trailing mode, than $time1$ and $time2$ mean rise and decrease of the signal, or two leading edges mode, where times are signals from two different particles that pass the cell within defined time. In the first case, is the time2-time1 difference, so called time above threshold, related to the charge deposited on the sense wire. The measured time $time1$ consists of the time that particle needs to arrive from the target to the MDC module and drift time that the first clouds of ionization electrons need for drift to the sense wire, the so called drift-time. From this drift time we can calculate the minimum distance to the

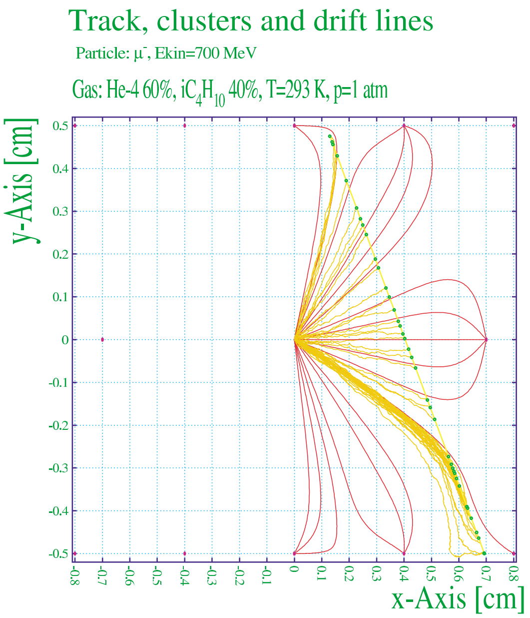

Figure 2.11: The track that pass the MDC drift cell with the inclination angle 30 degree builds in gas clusters of electrons. These clusters drift in electric field to the anode following the yellow line. The cluster that arrives to sense wires determines the begging of the signal at the moment TDC threshold is overcome. Red lines are field lines.The simulation with GARFIELD from [24].

wire of the particle track. For this calculation we need to know the drift velocity in the cells. This drift velocity is constant in the most of the cell area, where the electric field is also constant. For example, for the module 1 it is v_{drift}= 49 μm/ns. The value of the drift velocity in various places in the cell was simulated [24] and is shown is *Fig. 2.12*. The drift velocity depends also on temperature, pressure and purity of the gas. Ions drift with much slower velocity to the cathodes, because of their large mass. The precision of measuring this distance to the wire has been deduced from a MDC prototype being about 70 μm (spatial resolution) [26]. This value corresponds to the time resolution of the individual cell of about 1.7 ns. Note that this resolution gets worse close to the sense wire (due to the statistics of the ionization) and close to the field wires (field inhomogeneities).

2.4.3 Hit finding in MDC

As it was described in the previous section, the main task of the HADES drift chambers is the high resolution tracking. The measured variables are set of the fired wires in events and for each fired wire the TDC information in channels is read out. These raw data are calibrated to get the drift times and distances to wires in two steps of calibrations. The detection efficiency of the one layer of the MDC module is estimated to be 0.98%.

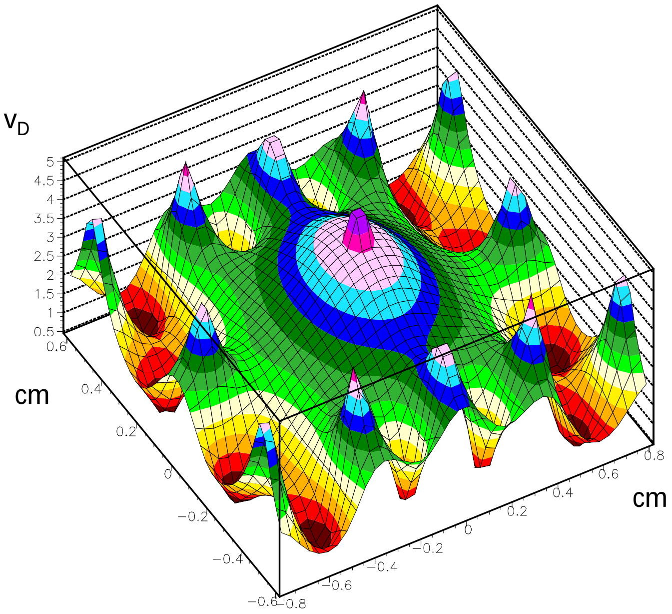

Figure 2.12: The shape of the amplitude of the drift velocity in the MDC cell as it was simulated with GARFIELD [24].

Therefore, for each track, at least one wire gives signal (is fired) in each layer. The aim of the offline tracking software is to reconstruct from this information the position of the hit in MDC (the place where particle passed the chamber). Hits are defined as a (x, y) points in the local MDC module coordinate system defined by the layer in the middle of the module parallel to the wire layers in the module. The center of the local module coordinate system is so called physical center of the chamber. It is the point where the track starting from the target is incident to layers of the module. The multiple scattering and magnetic field between the inner modules is low enough to allow to assume the track is a straight line. This makes possible to use both modules together to look for the particle track. However, usually the multiplicity of the particles in the module is larger than 1, especially for higher mass collision systems. Therefore, it is necessary to apply an algorithm to assign the fired wires properly to the different tracks. The piece of the track that connects the two corresponding hits in two modules is a MDC segment. One can in principle look for segments directly using information from both modules or look for hits separately and then combine the hits from different modules. First method has an advantage, that the secondary particles, that are created between the modules and belong to the background of the hits from tracks from the target, are not reconstructed. There are two independent MDC hit finder algorithms developed in HADES. Both are named by the institutions where they were developed. One is the Dubna/GSI tracking and second one is the Santiago tracking. For the data analysis presented in this work the Dubna/GSI

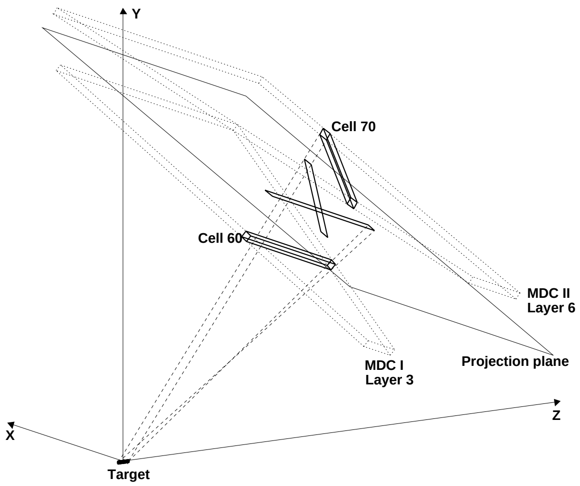

Figure 2.13: The principle of the projecting of the wires on the projection plane in the MDC cluster finder.

tracking has been used and therefore the second strategy will not be discussed. Whenever we speak about the MDC tracking, it is implicitly meant the Dubna/GSI tracking.

The tracking works in two main modes. The cluster finding and cluster fitting. As it was mentioned above it can be switched to use single chambers separately or both chambers together. In the analysis of data here cluster finding method in the common mode was chosen to suppress the particles which are not produced in the target. The fitting method was still under testing and has not been applied in present analysis, details can be found in [24]. The cluster finding method does not use the time information from wires. The fired wires from both modules are projected from the target on the common projection plane which is in the middle between the inner modules, see *Fig. 2.13*. The projection plane has a finite binning. The places where the single projections cross correspond presumably to tracks that passed the chambers, see *Fig. 2.14*. One can visualize the clusters candidates in a way that in the third dimension the multiplicity of the participation of the bin in projection from all fired wires in event is plotted. In such approach, the cluster candidates build peaks of pyramid shape, see *Fig. 2.14* and only few bins belong to maximal multiplicity. If the multiplicity of the tracks in the module is large enough, the projections of the wires can overlap accidentally. To separate the clusters corresponding to the true tracks , minimum multiplicity of occurrence of the bins in projections (in 3D visualization minimum hight of pyramid peak) is required. This minimum was optimized for three multiplicity groups of the fired wires in the module. For multiplicities smaller or equal 10 minimum of occurrence 4 is required. It means that at least 4 wires in different layers should contain the bin in their projection, and then the bin can belong to a cluster candidate. For multiplicities more than 50 minimum 6 is required, otherwise it is 5. In the following text for simplicity it is spoken about levels 4,5,6 of the cluster finder. Algorithm switches in each event to the corresponding setting according to the multiplicity of the fired wires in the event. For the C+C collisions at 2 AGeV the most probable level is 5 (in 70% of lepton tracks).

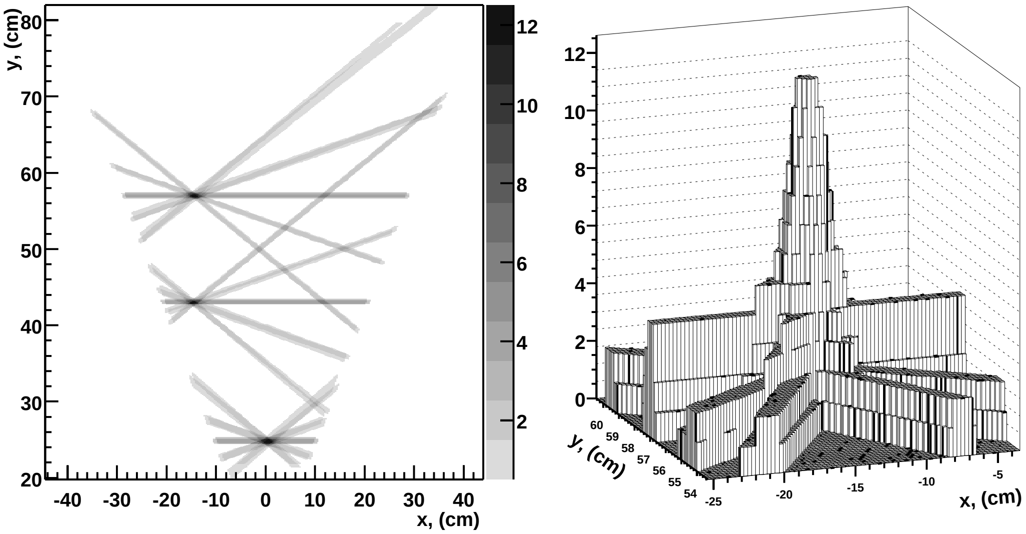

Figure 2.14: The crossing points of the projected wires builds the clusters (left). In 3D visualization projected wires build up pyramids, where the third dimension is the multiplicity of the bin on the plane in the area of projected wires summed over all layers.

The MDC cluster is defined by the set of bins, that pass the minimum occurrence in projections. The position of the cluster is calculated as weighted average from the positions of the centers of the contributing bins, where the bin occurrence is a weight. This method gives a rather low position resolution of 0.2 mm in x coordinate and 1.5 mm in y coordinate. However for low multiplicity environment of the C+C collision it is sufficient for the track reconstruction. For this method straight track approximation and exact alignment of the modules are very important. The particles with higher momenta do not change very much trajectory due to multiple scattering and therefore the position resolution for them is better. For each cluster its position is stored together with its cluster size and the number of the contributing wires to the cluster. The cluster size is number of the bins that contribute to the cluster. The number of the wires contributing to the clusters is number of the wires from all layers of the module (or 2 modules in combine mode) that contribute with their projection to the cluster. These variables turned out to play a very important role in the close pair recognition. This will be in detail described in *Chapter 4*. It is important feature of cluster finding that the same hit has different cluster size if it is counted with different level of the cluster finder. The tracks that are perpendicular to the module have the smallest area of the projected wires and therefore also the smallest cluster size. The same is valid, however, not so strong, for the number of the contributing wires. The tracks that have large angle with respect to the perpendicular one, can in the same layer cross more neighboring cells and consequently the total number of the contributing wires in the cluster is on average larger for such clusters. The properties of the clusters has been accordingly studied in several bins of azimuthal and polar angles of the particle tracks and for each level of cluster finder separately. From the position of clusters on the projection plane, the positions of the hits that correspond to this cluster in the modules 0 and 1 is recalculated. These two MDC hits correspond to one track piece, the MDC segment.

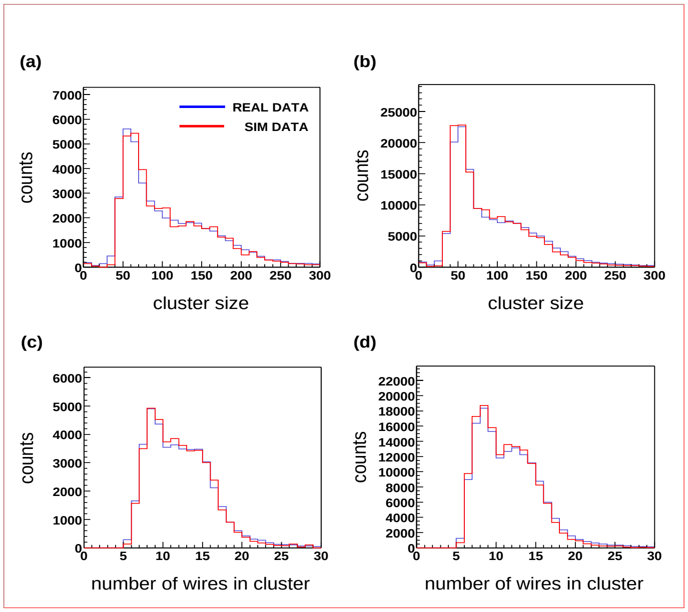

Figure 2.15: The comparison of distributions of the simulated (red) and measured (blue) cluster sizes:(a),(b) and number of contributing wire to the cluster:(c),(d) for module 1, level of cluster finding 5 and polar angles: 10-20° (a),(c) and 20-30° (b),(d).

2.4.4 The comparison of properties simulated and measured MDC clusters.

The parameters of the MDC clusters are used in analysis of the measured data for close pairs rejection, see *Chapter 4*. The selection criteria are determined by analysis of the simulated data. It is therefore decisive that these parameters are described well in simulated data. In the *Fig. 2.15* the comparison of the cluster size and number of the wires in the cluster for measured or simulated clusters is given. The compared clusters have been selected from lepton tracks. The shape of the distributions prove very good accordance between measured and simulated clusters for both parameters. The difference have been factorized by comparing of the means of the distribution for each group of the clusters (polar angle, azimuthal angle, level of cluster finding, module). In the *Fig. 2.16* and *Fig. 2.17* the comparison of the mean value of the clusters size (resp. number of contributing wires) for measured or simulated clusters is shown. The largest difference is for inclined tracks with high or low polar angles. However the difference of the mean values is smaller than 15%. The ratio of the mean values of the simulated and measured cluster parameters have been tabulated for each cluster groups and it has been taken in an account when applying selection criteria in *Chapter 4*.

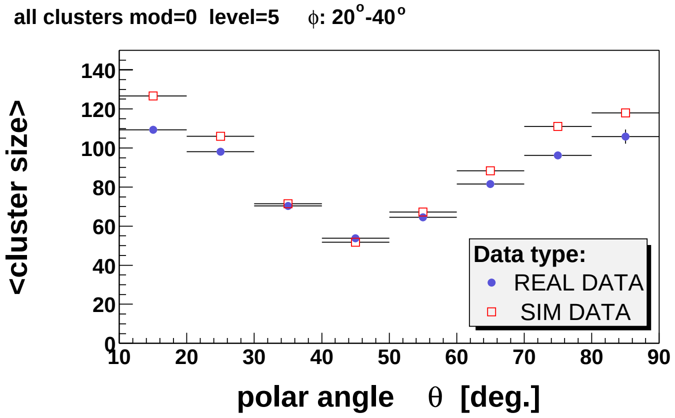

Figure 2.16: The averaged cluster size as a function of polar angle θ (profile histogram) for real (blue points) and simulated (red points) data. The distribution are plotted for all clusters in module 0 with $\phi : 20^{\circ} - 40^{\circ}$ for events with level of cluster fining $level = 5$.

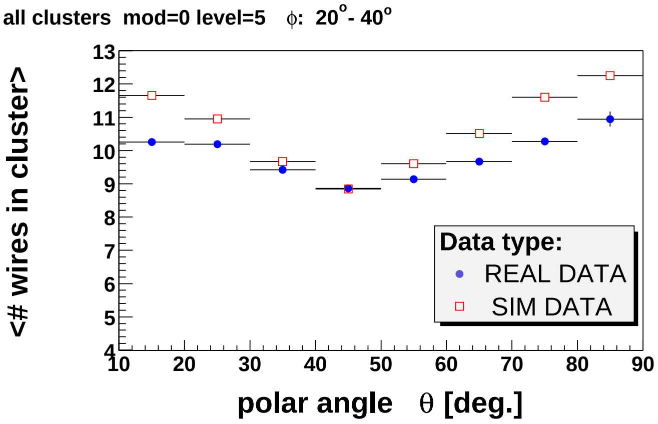

Figure 2.17: The averaged number of wires in cluster as a function of polar angle θ (profile histogram) for real (blue points) and simulated (red points) data. The distribution are plotted for all clusters in module 0 with $\phi : 20^{\circ} - 40^{\circ}$for events with level of cluster fining $level = 5$.

2.5 The HADES magnet

The momentum determination of the charged particles is in HADES based on the momentum kick of the particles in the magnetic field that is between the inner and outer MDC modules, see *Fig. 2.8*. The magnetic field in created by superconducting toroidal magnet. The magnet consists of 6 superconducting coils mounted in 80mm thick separated cases. The cases are from aluminum and superconducted material is Al stabilized Cu(Nb/Ti) conductor. An AlCu:NbTi ratio is 10:1 and Al:Cu(Nb/Ti) ratio is 3:1 in the composition. The magnet works with the maximal current 3566 A and working temperature is 4,6K.

The magnet creates an inhomogeneous magnetic field that is inside the case up to 3.7T, close to case reaches strength of 2.4 T, and in the middle of the sector about 0.8T [27]. The momentum kick in the field is for full field from 40 to 120 MeV/c.

2.6 Multiplicity and electron array

The last detector system covering the HADES spectrometer is a multiplicity and electron array (META). It consists of three detectors. The TOFINO and PreSHOWER detectors cover the acceptance from 18° $< \theta <$ 45° and the Time of Flight detector covers the acceptance of 45 $< \theta <$ 85°. The detector system is designed for an additional lepton identification and multiplicity measurement. The multiplicity of the hits in META is part of the trigger system (LVL1) and it is related to the centrality of the measured collision.

2.6.1 PreSHOWER detector

The PreSHOWER (or equivalently SHOWER) detector is designed for additional lepton identification for particles with polar angle $\theta <$ 45°. In this region most of the high momentum pions is detected and they should be separated from leptons.

The basic idea of the electron identification in the PreSHOWER detector is measurement of the electromagnetic showers produced in the lead material of convertor. Charged particles are losing their energy while passing the material. This losses are strongly dependent on the mass m of the particle. For particle with high mass is the energy loss small and vice versa. For protons and pions are these losses negligible compared to those for light electrons. Particles are loosing their energy by bremsstrahlung and e^+e^- pair production. For materials with high Z (atomic number), the bremsstrahlung is dominating the ionization for $E > E_{crit}$, where E_{crit} = 1600 m/Z. For example, for Pb it is already for energies larger than 7 MeV. The produced particles build an electromagnetic shower. The fact that electrons and positrons produce an electromagnetic shower and protons and pions do not produce a shower while passing the material of convertor, is used for lepton/hadron separation. The PreSHOWER detector, see *Fig. 2.18* consists of two lead convertors inserted between three wire chambers with a pad read-out. The shower recognition is performed by comparing the number of particles measured before and after the lead convertors. Particle hits are identified via charge produced in ionization processes in the wire chambers working in a self quenching streamer mode (SQS). The main advantage of the SQS mode is that the induced charge is nearly independent of particle specific energy loss and therefore low energy protons do not produce large signals in the post convertor chambers due to their significant energy loss in the lead material and consequently are not misidentified with electromagnetic showers. The other advantage of the SQS mode is a high amplitude of the produced signals (0.2-40 mV) . Finally, the recognition of leptons from protons and pions is based on a comparison of integrated charge on the pads before and after the lead convertors. For electrons and positrons passing the detector is this charge in the second and the third chamber significantly larger than in the first one, because of the produced showers in the lead convertors.

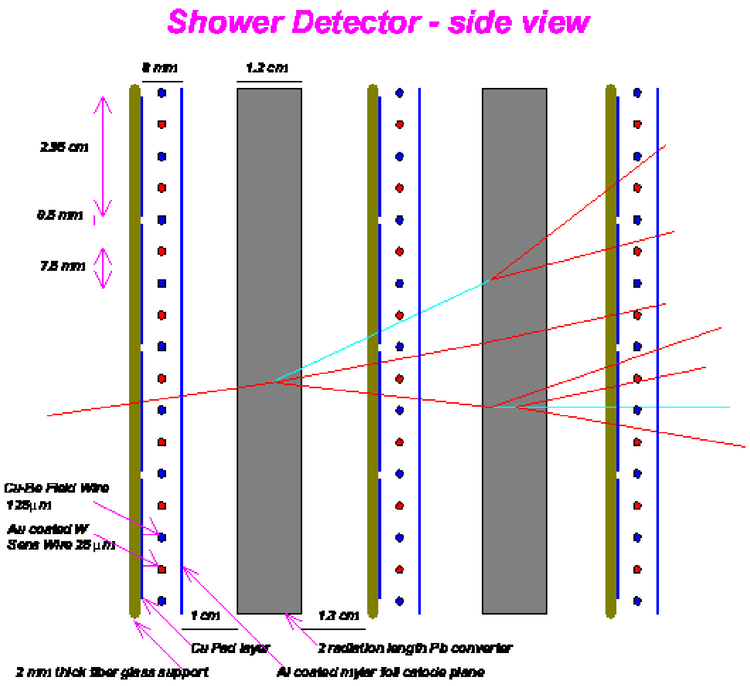

Figure 2.18: Schematic view of the PreSHOWER detector consisting of the 3 wire chambers with 2 Pb convertors between them. The lepton while passing the convertor produced a electromagnetic shower.

2.6.2 Time of flight detector

The TOF detector [28] covers the acceptance of HADES from 44° to 88°. The main purpose of this detector is a) the fast determination of charged particle multiplicity of the event in order to trigger on the centrality of the collision in the first level trigger b) the fast reconstruction of the hit position in TOF in order to allow a fast second level trigger decision and c) the measurement of the time of flight of each hitting particle in order to perform the electron/hadron discrimination.

The TOF detector, see *Fig. 2.19* is made from scintillator rods. As a particle passes through the scintillator, it excites the atoms and molecules which emit light during deexcitation within 10^8 s .This light is transported to the photomultiplier, where it is converted to photoelectrons. The weak current from the photoelectrons is amplified and read out by electronics. The advantage of the scintillator is its fast response and short recovery time.

The TOF wall is made of 6 sectors placed in hexagonal geometry - each sector constitutes from 8 cases containing 8 scintillating bars. Each bar is read out at its two ends by means of fast photo-multipliers (EMI 9133B). Within a given case, the rods have identical length, however, for different cases the length varies from 1475 mm to 2365 mm. The distance of the rods from the target is between 2075 mm and 2235 mm.As a scintillation material was chosen to be BC408 from Bircon. Each rod is wrapped in aluminized mylar sheets to optimize the reflectivity on the surface.

From the measured signal one can determine the following information: the time of flight (t_{TOF}) of particles, the hit position on the rod (x), the energy deposited in the rod by the passing particle (ΔE), and the redundant hit position ($\tilde{x}$). These values could be extracted from the following relations:

$$t_{TOF} = \frac{1}{2}\left(t_{right} + t_{left} - \frac{L}{v_{group}}\right), \tag{2.11}$$

$$x = \frac{1}{2}\left(t_{right} - t_{left}\right) v_{group}, \tag{2.12}$$

$$\Delta E = k\sqrt{A_{left}A_{right}\mathrm{e}^{L/\lambda_{at}}}, \tag{2.13}$$

$$\tilde{x} = \frac{\lambda_{at}}{2}\ln\left(\frac{A_{left}}{A_{right}}\right), \tag{2.14}$$

where t_{right}, t_{left} denote time measured on the left and the right side of the rod corresponding to time between the reaction and the readout of the signal, v_{group} is the group velocity in the rod (average velocity of light in the rod), L is the length of the rod, A_{left} and A_{right} are the light signal amplitudes on the left and right end of the rod, λ_{at} is the light attenuation length of the rod and k is a constant.

The Overall TOF resolution excluding the contribution of the START detector with related electronics is σ_{TOF} = 150 ps [28]. The detection efficiency was determined to be 0.96±0.01. From the simulation it can be concluded that this is due to a dead space of 0.8 mm between the rods. The corresponding resolution of the hit position along the bar itself is σ = 2.5 cm. The fast signal information from the TOF is used in the HADES first level trigger. The electrons and positrons move from the collision with the velocity close

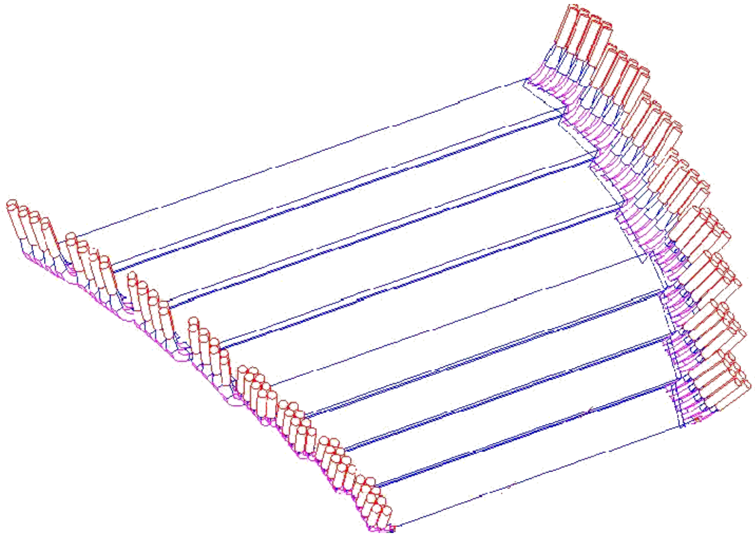

Figure 2.19: The schema of the TOF detector.

to the speed of light and they are thus the fastest particles. This is selection criterion for lepton identification.

2.6.3 TOFINO detector

The TOFINO detector, see *Fig. 2.20* is another detector for the measurement of the time of flight of particles. It covers the polar angle θ acceptance from 18° to 45°. The TOFINO detector is placed in the sector in front of the SHOWER detector with respect to the target. There are four plastic scintillator paddles covering one sector. The signal is read only from one side of the paddle. The position of the place, where the particle hits the detector, can be retrieved only using the combined information with the SHOWER detector. The time resolution of the TOFINO detector is $\sigma = 400ps$. The granularity of the TOFINO detector is low and in a case that 2 particles pass the detector in one event, time information read by detector is degraded. The substitution of the TOFINO detector with RPC (Resistive Plate Chamber) is forseen in the future to increase the granularity of the detector for measurement with heavy collision systems.

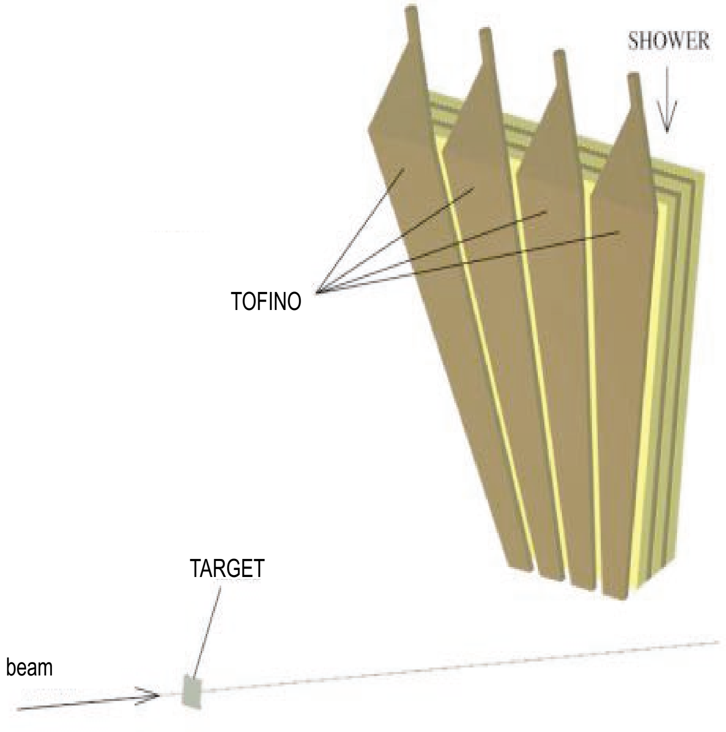

Figure 2.20: The schematics view of TOFINO detector in one sector. The detector is placed in the front of SHOWER detector.

2.6.4 HADES trigger

In experiments conducted with the HADES spectrometer, event rates up to 10^6 Hz must be handled. This requires a trigger system which is able to reduce the event rate up to the factor of 10^4 by pre-selecting interesting events with relevant signatures.

In the most challenging case of heavy ion collisions, the first level trigger (LVL1) selects 10% of the most central events via multiplicity of hits in the TOF and TOFINO detector modules. The condition on the multiplicity in the META is as follows [29]: The signal from photomultipliers of TOF and TOFINO is read by analog trigger. Each TOF photomultiplier with signal contributes to analog multiplicity with -20mV and each TOFINO photomultiplier with signal with -40mV. The discriminator threshold is put to -150mV. There is about 20% cases that there is only signal in one of the photomultipliers in TOF rod. This is due the secondary particles with deposited energy close to discriminator threshold. The dissipation of the signal in rod, can lead to the situation that signal is too small to be read in the photomultiplier on the end of the rod, that is at large distance from hit. If two of these cases happened simultaneously, the contribution is identical at it would be in a case of real hit, with signals on both photomultipliers. The analog trigger that is used can be written in form:$(M_{TOF-PM} + 2 * M_{TOFINO-PM})/2 > 3$, where M_{TOF-PM} and $M_{TOFINO-PM}$ are the multiplicities of the photomultipiers with signal from TOF or TOFINO receptively. The factor 2 in the front of the $M_{TOFINO-PM}$ is because the TOFINO signal is read only with one photomultiplier and therefore one hit gives only one signal, where on the turn the hit in TOF gives signal in two photomultipliers. The multiplicity of the signals from from photomultipliers is related to number of the hits in the META and therefore also to the multiplicity of the detected charged particles. A positive first level trigger initiates the readout of all detectors. In November 2001 beamtime the LVL trigger rates in peak of spill has been up to 5 kHz. The trigger rate has not been saturated, but it was limited by possible taping rate,while no additional LVL2 trigger has been used to reduce the data.

The main trigger component, the second level trigger (LVL2), selects events with dilepton pairs in a given invariant mass range. In the first step, the image processing units detect electron/positron signatures in the RICH, SHOWER and TOF detectors making extensive use of programmable logic. There is a hardware RICH ring reconstructor implemented, it is possible to make hardware decision in the SHOWER detector whether an electromagnetic shower was detected, and also to make selection on the time of flight of the particle in TOF. The resulting position information from this first stage is correlated between the ring of RICH and hits in the TOF and SHOWER detectors, taking into account bending in the magnetic field and thereby applying a selection on the particle momenta. Two such valid candidates with a minimum opening angle are considered to be a valid dilepton candidate with a sufficiently high invariant mass which initiates a positive second level trigger signal. The second level trigger is projected to reduce the event rate by about a factor of 100 with a latency time of about 15 events ($\gg$ 150 ms), but was not yet active in the November 2001 run.

The third level trigger (LVL3) performs a consistency check of the potential electron candidates determined in the second level trigger evaluating the hit pattern of wires from the MDC modules. The electron hit positions determined in the Second Level Trigger both for the RICH and the META detectors define regions of interest in the MDC modules. To discard events with uncorrelated hits in RICH and META, the pattern information of fired wires from the MDCs is used. The regions of interest must be determined from a simple approach which assumes a single kick-plane in the magnet and basic logical correlations must be evaluated for the corresponding wire pattern. The third level trigger is expected to gain a reduction factor of 10 in future experiments.

The communication between the different detectors is realized via a dedicated trigger bus between a central unit (CTU) for each trigger level and several detector trigger units (DTU). The bus distributes the three level trigger decisions, event identification numbers, trigger codes and detector busy/error conditions. The CTU distributes the trigger decisions, generates event identification numbers, and handles event types as well as busy and error conditions. The DTUs are responsible for the handling of the incoming HADES trigger bus signals and control various readout components via local readout system trigger busses.

Contribution to the commissioning of the HADES

The author has participated in all commissioning beamtimes from November 1998 to November 2001 within the MDC detector group. For each commissioning beamtime full scale HADES simulations have been performed for the actual set up(for details concerning November 2001 see *Section 3*). The LVL1 trigger condition and the selected target size have been designed based on the prepared simulations. The quality and consistence of the measured data have been compared with simulations already during the beamtime. The data from all commissioning and test beamtimes have been analyzed and detector performance has been determined. However only results from November 2001 beamtime are presented in the present work. This run was the first to deliver sufficient statistics for a dilepton analysis.

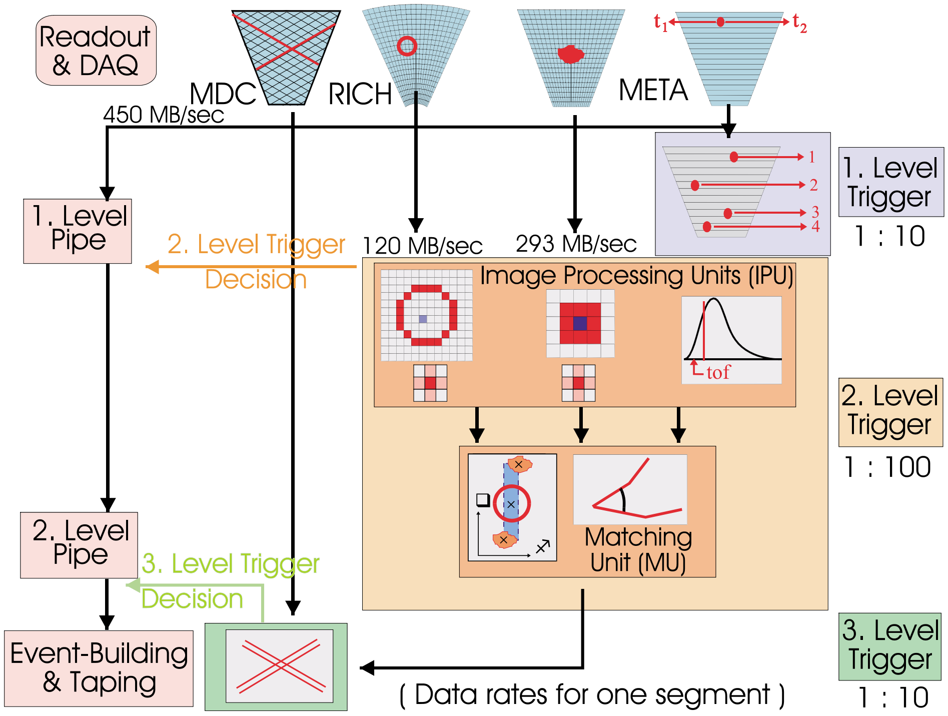

Figure 2.21: Schema of the HADES trigger system.A 3 level trigger system is designed, matching the information from all detectors.(Only LVL1 was used to aquire the data discussed in this work.)

3

Monte-Carlo simulation of C+C collisions at 2 AGeV

3.1 Introduction

Full scale simulations of C+C collisions at $2A$GeV have been performed to study the response of the HADES spectrometer and for the preparation of the proposal for the experimental runs. The simulated data allows efficient analysis preparation before the measured data are available. It also helps to understand and interpret the results obtained by analyzing measured data.

The simulated data has to be produced under conditions that are close to the real measurement and the analysis should be performed for both types of data in an identical way. The most important advantage of simulated data is however that during the simulation itself and during the analysis of simulated data the access to the complete original information about the parameters of all particles in system is possible. This allows to compare the reconstructed parameters of particles with the true, ideal one and justify the analysis steps.

For the HADES simulations a dedicated package 'HGEANT' has been developed. HGEANT is based on the GEANT [30] version 3.21. The complete detector geometry has been implemented and detector response has been simulated in digitization of the simulated information. In *Fig.3.1* a cross section of the HADES is shown as it is implemented in HGEANT together with one C+C collision. The simulated and real data are in high level analysis treated equally. The schematic simulation and analysis flow is show in *Fig.3.2*. Two type of simulations have been performed. Chronologically the first one was the simulation of the spectrometer acceptance and response to the different dilepton sources. A simplified analysis has been used for particle reconstruction and the invariant mass spectrum of 5 day beamtime has been estimated, see *Section 3.4*. For this simulation a fast event generator Pluto++ [31] has been used for each source separately. The second

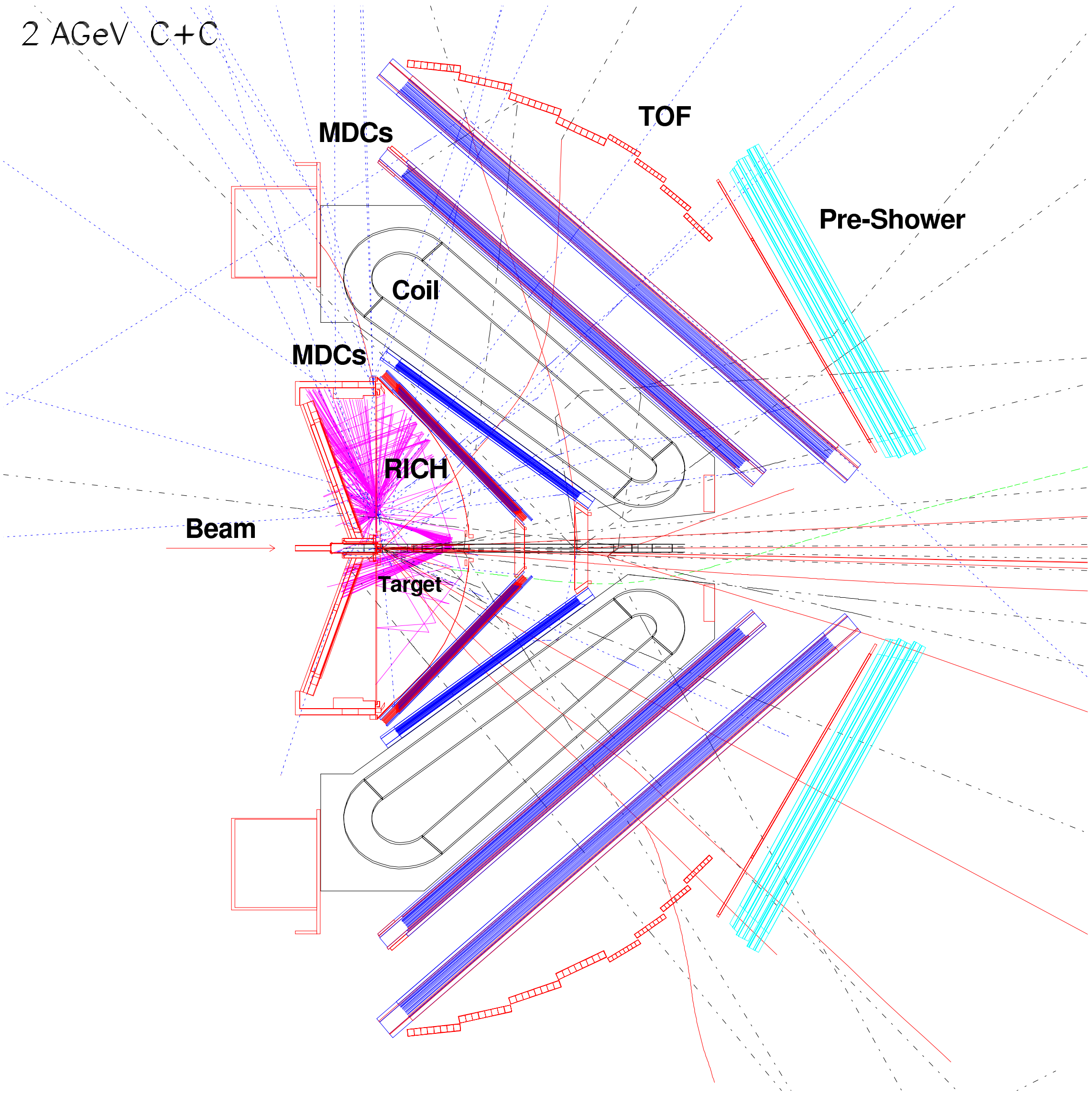

Figure 3.1: The simulation of a C+C collision at 2 AGeV in the HGEANT environment. The cross section through the HADES detector volumes is shown. Blue lines are charged particles, red lines are electrons, and green are muons.

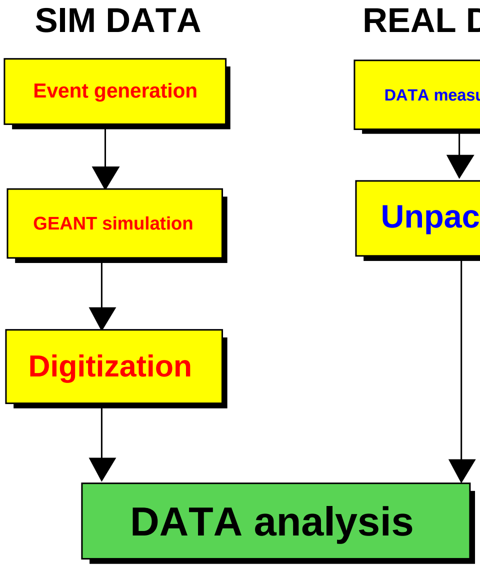

Figure 3.2: The schematic view of the treatment of measured and simulated data in analysis flow.

type of simulation has been performed with UrQMD model (version v1.2) [4] generated events. The analysis steps have been applied in the same way as for analysis of the measured data. The results from analysis of these data are used in this work for comparison with measured data.The statistics of about 20 million of C+C collisions at 2 AGeV has been simulated and analyzed for the conditions of the November 2001 beam-time. This is about 50% of the statistics measured and events selected for analysis, but it allows a quantitative comparison also for dilepton production. The main difference between the both approaches is that the first method allows fast but approximate estimation of the results, where the second method is time consuming but simulates the detector response and analysis performance close to the data with measured particle multiplicities. The dominant source of the measured $\mathrm{e^+e^-}$ pairs are π^0 decays, therefore in next Section the comparison of the UrQMD with experimental data is given.

3.2 Event generators

The main criteria for selection of the event generator are:a) particle multiplicities and distributions have to correspond to measured one, b) it should contain processes and particles of interest,c) flexibility for simulating various scenarios,d) feasibility of the generation of the large amounts of events. UrQMD model [4] is well established model that has been already used to simulate the heavy ion collisions in SIS regime, for example see [32]. It allows flexible generation of the collision at various beam energies and collision systems. The reliability of the π^0 production is discussed in next paragraph.

3.2.1 π^0 production in UrQMD

As π^0 is the most dominant source of produced $\mathrm{e}^+\mathrm{e}^-$ pairs and also the most dominant decay of π^0: π^0 to $\pi^0 \rightarrow \gamma\gamma$ with consecutive γ conversion : $\gamma \rightarrow e^+e^-$ contributes with largest part to combinatorial background, the π^0 production in UrQMD is compared to the measured multiplicities from TAPS experiment [20, 33]. The TAPS has measured also η production and therefore also these values are compared.

The UrQMD generated π^0 multiplicities were therefore compared to the measured yields for C+C collisions from the TAPS experiment [20, 33].

In *Tab. 3.1* and *Tab. 3.2* the comparison of the π^0 and η production in UrQMD for $^{12}C +^{12} C$ at 0.8, 1.0, and 2.0 AGeV energies, and $^{12}C +^{197} Au$ at 0.8 AGeV systems as they have been measured by TAPS is shown. Since the TAPS spectrometer has a limited laboratory rapidity acceptance of $\Delta y = 0.42 - 0.74$, two values are provided, one for the TAPS rapidity interval and the second one for the full rapidity range. The multiplicities summed over the full rapidity interval are estimated for TAPS based on the extrapolation from the measured values over Δy assuming an isotropic angular distribution for the produced pions [20, 33].

System	C+C					
Source	TAPS	UrQMD	TAPS	UrQMD	TAPS	UrQMD
Energy [AGeV]	0.8	0.8	1.04	1.00	2.0	2.0
Δy	0.42-0.74	0.42-0.74	0.42-0.74	0.42-0.74	0.8-1.08	0.8-1.08
$\langle M\rangle_{\pi^0}{}^{\Delta y}[10^{-2}]$	6.0 ±0.4	5.7±0.1	8.0±0.5	8.3±0.1	13.7±1.7	18.0 ±0.1
$\langle M\rangle\eta^{\Delta y}[10^{-4}]$	2.3±0.7	1.0±0.3	7.2 ±1.4	3.8±0.6	85±15	49.7±2.2
y	all	all	all	all	all	all
$\langle M\rangle_{\pi^0}{}^{all}[10^{-2}]$	22.2 ±1.8	32.8±0.1	33.5±2.5	50.0±0.2	82.6 ±8.4	124.0 ±0.3
$\langle M\rangle\eta^{all}[10^{-4}]$	6.9±2.5	2.5±0.5	17 ±5	10±1	294±46	240 ±4

Table 3.1: Comparison of mean multiplicities for π^0 and η measured by TAPS and given by UrQMD for **C+C** collisions. The rapidity interval Δy covered by TAPS in the laboratory frame is given in the third column. The mean multiplicities extrapolated by TAPS to the full y interval are shown in the second part of the table. In the TAPS extrapolation of the multiplicity an isotropic angular distribution has been assumed.

At the low beam energy, the TAPS and UrQMD generated π^0 multiplicities in the TAPS interval of rapidity are identical within error bars and their difference is increasing with the energy up to 25%[1] at 2 AGeV for C+C. Comparing both systems, C+C and C+Au, this behavior is found to not depend on the number of nucleons in the collision.

---

[1] Very recently the version UrQMD v1.3 has been investigated [34]. The generation of the events with the Wood-Saxon potential model of the nuclei and removing the spectators from them, leads to mean π^0 multiplicity in C+C accepted in HADES after simulating trigger about 30% smaller than in the UrQMD v1.2.

System	**C+Au**	
Source	TAPS	UrQMD
Energy [AGeV]	0.8	0.8
Δy	0.42-0.74	0.42-0.74
$\langle M \rangle_{\pi^0}{}^{\Delta y}$ [10^{-2}]	10.2 ±1.0	10.2 ±1.0
$\langle M \rangle \eta\ ^{\Delta y}$ [10^{-4}]	-	-
y	all	all
$\langle M \rangle_{\pi^0}{}^{all}$ [10^{-2}]	40.9 ±3.8	54.5 ±0.2
$\langle M \rangle \eta^{all}$ [10^{-4}]	-	-

Table 3.2: As in *Tab. 3.1*, for **C+Au** system.

The η meson multiplicities have the opposite behavior: with increasing beam energy the difference between the TAPS measured and UrQMD generated multiplicities decreases. But the absolute value of the difference is about 60% at 2 AGeV for C+C. For the π^0 multiplicity the UrQMD value overestimates the measured one while for the η multiplicity it is underestimated.

The extrapolated values of the π^0 multiplicities in the full rapidity range differ more than those in the TAPS acceptance rapidity interval. This is due to the assumption of an isotropic angular distribution for produced pions in TAPS. The UrQMD generator produces π^0 with an angular distribution that differ from the isotropic source. This can be seen from the angular distribution of π^0 in UrQMD in the center of mass system (C.M.) as shown in *Fig. 3.3* for π^0 produced in C+C collisions at 1.0 AGeV. The angular distribution in the phase space can be characterized by the polar angle. The azimuthal symmetry of the system allows to integrate over the azimuthal angle ϕ. This integration gives factor 2π. The differential of the solid angle reads $d\Omega = 2\pi \sin\theta d\theta$. Therefore, $dN/d\Omega = 1/(2\pi\sin\theta) \cdot dN/d\theta$. If the π^0 would be produced isotropically, as the TAPS extrapolation assumes, then the $dN/d\Omega$ spectrum would be flat. This is not the case for the UrQMD produced events. The anisotropy can be quantified by fitting the spectrum with the function $F = a + b\cos^2\theta$. The ratio of the fit parameters a, b for the UrQMD produced π^0 in C+C at 1.0 AGeV in *Fig. 3.3* is b/a = 0.82. This ratio for the isotropic distribution would be equal to 0.

It can be concluded that the UrQMD source has a strong anisotropic angular distribution that results in an enhancement at the forward and backward angles and possible explains the difference in the comparison of the UrQMD generated and TAPS extrapolated values of the π^0 multiplicities over the full rapidity range.

For the sake of completeness, the rapidity distribution of π^0 generated by the UrQMD are compared with the rapidity distribution of π^0 emitted from a thermal source with T = 56 MeV in *Fig. 3.4*. The rapidity distribution of the thermal source is given by [35]

$$\frac{dn_{th}}{dy} = \frac{V}{(2\pi)^2} T^3 \left(\frac{m^2}{T^2} + \frac{m}{T}\frac{2}{\cosh y} + \frac{2}{\cosh^2 y} \right) \mathrm{e}^{-\frac{m}{T}\cosh y}, \tag{3.1}$$

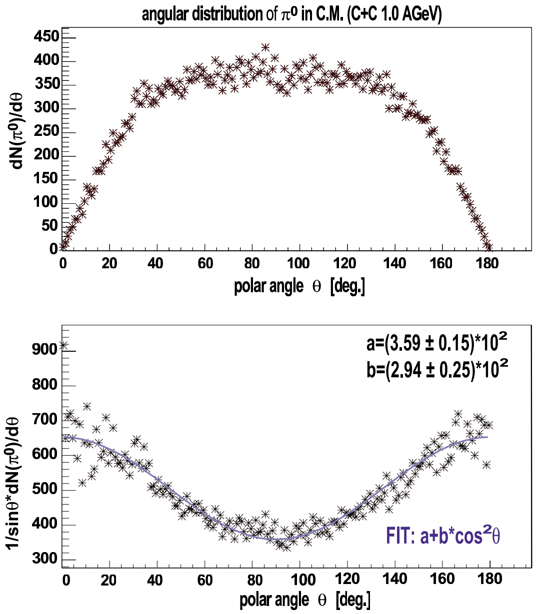

Figure 3.3: The angular distribution of the π^0 produced by UrQMD in the center of mass system. The distribution is fitted with the function $a+b\cos^2\theta$ and the value b/a = 0.82 characterizes the anisotropy of the source.

where V is the volume, T is the temperature of the source, and m is the mass of the particle of interest.

The rapidity in both cases differs at the higher and lower edge. This implies again the angular distribution of the π^0 source differs from an isotropic one. This representation has an advantage that it is Lorenz invariant.

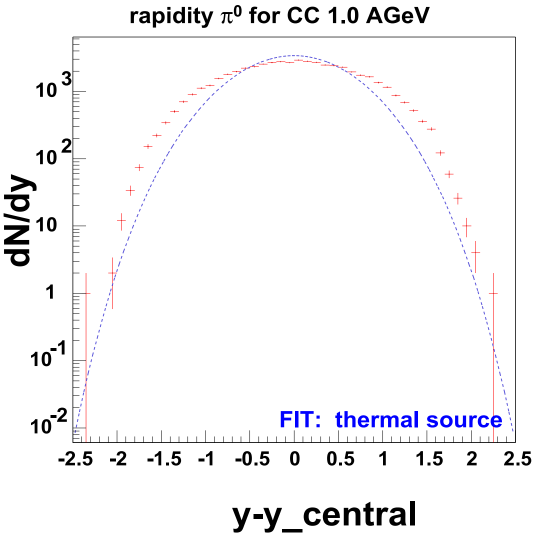

Figure 3.4: The rapidity distribution of the π^0 produced by UrQMD for C+C at 1 AGeV. The distribution is compared to an isotropic thermal source distribution with T = 56 MeV using Eq. (3.1). The deviations for low and high rapidity come from the anisotropy of the UrQMD distribution.

The slope parameter of the transverse mass distribution $m_T = \sqrt{m_{\pi^0}^2 + p_T^2}$ of π^0 in C+C collisions at 1.0 AGeV in UrQMD has also been studied (see *Fig. 3.5*). The inverse-slope parameter T for UrQMD is extracted from fitting the transverse mass spectrum with

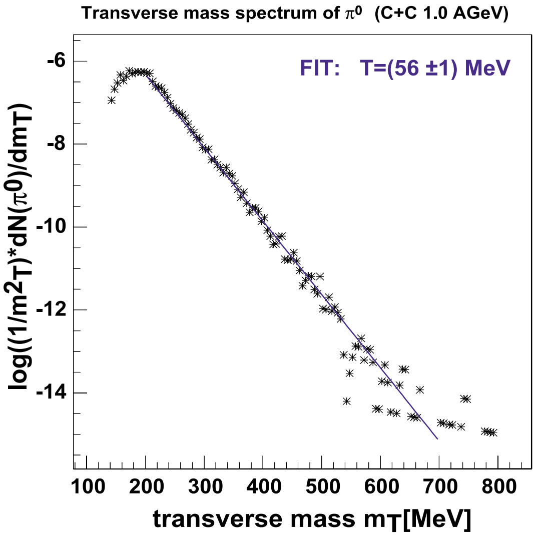

Figure 3.5: Transverse momentum distribution of π^0 produced by UrQMD for C+C at 1 AGeV. The spectrum was fitted with a Boltzmann function resulting in an inverse slope parameter of (56±1) MeV.

Source	System	Energy [AGeV]	Δy	particle	T [MeV]	$< p_T >$ [MeV/c]
TAPS meas.	C+C	1.0	0.42 -0.74	π^0	54±3	187±5
UrQMD	C+C	1.0	0.42 -0.74	π^0	56±1	198 ±6

Table 3.3: Comparison of slope parameters for π^0 transverse momentum distributions measured by TAPS and generated by UrQMD. The slope parameter T is deduced from Boltzmann fit. The averaged transverse momenta $< p_T >$ are for π^0 emitted in the given rapidity interval Δy .

a Boltzmann function

$$\frac{d\sigma}{dm_T} \approx m_T^2 \cdot e^{\frac{-m_T}{T}} \tag{3.2}$$

in the same way as it has been done for pions produced at mid-rapidity in TAPS [33]. In *Tab. 3.3* the inverse slope parameter and the mean transverse momentum are compared. The inverse slope parameter T = (56±1) MeV for UrQMD is consistent with the TAPS fitted value of T = (54±3) MeV [33]. The mean p_T is within 5% consistent with the value given by TAPS as well.

In *Tab. 3.4* the π^0 multiplicities from UrQMD for C+C central collision with impact parameter b=0.5fm are compared to multiplicities from BUU model. The multiplicities from BUU model are for beam energy of 0.8 A GeV about 50% larger, however for beam energy of 2 A GeV is BUU value about 20% smaller. Both models give different multiplicities of the π^0.

The average π^0 multiplicity of the UrQMD events for C+C at 2AGeV is about 20% larger as value measured by TAPS. The η multiplicity is for UrQMD in this case 40% smaller. This difference should be taken in an account in discussion of the results from simulated and measured data.

System	C+C					
Source	BUU	UrQMD	BUU	UrQMD	BUU	UrQMD
Energy [AGeV]	0.8	0.8	1.0	1.0	2.0	2.0
Δy	0.42-0.74	0.42-0.74	0.42-0.74	0.42-0.74	0.8-1.08	0.8-1.08
$\langle M\rangle_{\pi^0}{}^{\Delta y}[10^{-2}]$	22.1	13.6	26.8	18.4	38.2	44.5
y	all	all	all	all	all	all
$\langle M\rangle_{\pi^0}{}^{all}[10^{-2}]$	101.6	69.4	133.9	104.6	219.1	287.2

Table 3.4: The comparison of mean multiplicities for π^0 given by UrQMD and BUU for C+C collisions with impact parameter b= 0.5 fm. The multiplicities are compared in full y interval and in the rapidity interval Δy covered by TAPS in the laboratory frame.

3.2.2 The centrality of the simulated events

With UrQMD simulated events have been before the analysis also filtered with HADES trigger condition. Trigger condition changes the centrality of the produced events in similar way as it is for measured data. The original impact parameter distribution is influenced. The events with smaller impact parameter are called more central, because the nuclei centers are during the collision close to each other. The impact parameter distribution of UrQMD generated events reflects the hard sphere model of the nucleon density profile that was used. The impact parameter of the collisions was sampled from 0 to $b_{max} = R_p + R_t - d$, where R_p, R_t are the projectile and target radii and d is a fixed parameter at 1 fm. For C+C collisions it gives b_{max} = 4.4 fm. The minimum bias impact parameter distribution follows $dN/db \approx 2\pi b$ and therefore most of the collisions are produced with a large impact parameter, see *Fig. 3.6* (blue line). The mean impact parameter for C+C minimum bias events produced in UrQMD is $\langle b_{C+C}\rangle$ = 2.9 fm.

During the November 2001 beam-time the first level trigger (LVL1 trigger) has been used to trigger on events. The LVL1 trigger selects events that fulfill the multiplicity condition: $(M_{TOFPM} + 2 * M_{TOFINOPM})/2 > 3$, where M_{TOFPM} and $M_{TOFINOPM}$ is the multiplicity of the photomultipliers in TOF, and TOFINO respectively, in a given event (for details see *Section 2.6.4*). The HADES acceptance in polar angle is limited to $18° < \theta < 85°$. Most of the spectators and nuclear fragments have smaller angles and they are not detected. If the collision is more central, then more particles fly into the HADES acceptance. Therefore, the multiplicity condition in the LVL1 trigger increases the average centrality of the events that pass the condition.

The LVL1 trigger condition has also been simulated. The trigger condition $M_{TOF} + M_{TOFINO} > 3$, where M_{TOF} and M_{TOFINO} are the hit multiplicities in TOF and TOFINO respectively. The corresponding hit finders have been performed in advance and only the events which passed the condition have been selected for further analysis. The trigger condition applied to simulated data is not identical to the condition for measured data, but the difference is estimated to be less than 5% [29]. The impact parameter distribution of the events which passed the LVL1 trigger condition in the simulation is shown in *Fig. 3.6* (red line). The mean impact parameter for triggered events is $\langle b_{C+C}^{LVL1} \rangle = 2.7$ fm. The LVL1 trigger condition $M_{TOF} + M_{TOFINO} > 3$ decreases the average impact parameter by 7%. A fraction of 66% of collisions passed the trigger. The mean π° multiplicity in the events after LVL1 trigger increases to $\langle M_{\pi^{\circ}}^{LVL1} \rangle = 1.45$, which is 17% more than the multiplicity from the UrQMD source before the trigger. For η, the mean multiplicity increases by 22%.

There are no fragments produced in UrQMD and carbon nuclei are propagated as 12 unbound nucleons. The spectators of the collision can interact with the target and the target tube and the secondaries influence the trigger decision because they contribute to the $M_{TOF} + M_{TOFINO}$ multiplicity. In a real collision fewer secondaries are produced. This effect decreases the centrality of the triggered simulated events. The trigger decision in the measured data is in turn influenced by the presence of noise. This decreases the centrality of the measured data.

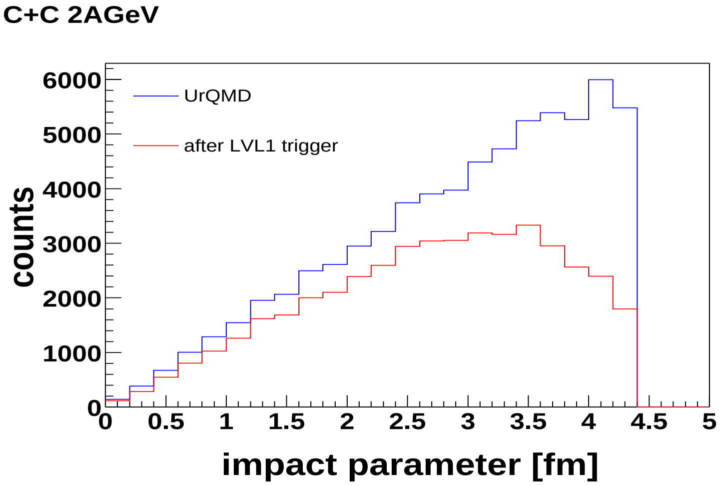

Figure 3.6: The impact parameter distribution of all events from UrQMD (blue) and those events that pass the LVL1 trigger (red).

3.3 Monte-Carlo simulations with HGEANT

The HADES simulation framework HGEANT is based on the CERN simulation package GEANT 3.21 [30], adopted to the HADES analysis environment with ROOT [36]. GEANT is a system designed to model detectors and simulate the passage of particles through them. It allows to describe an experimental setup as a structure of geometrical volumes filled with media defined by so-called tracking medium parameters. These parameters include a reference to the properties of the material filling the volume. GEANT processes events generated by event generators as input.

The particles in an event are propagated through the materials of the detector setup. This propagation takes into account geometrical volume boundaries, physical effects according to the nature of the particles themselves and their interaction with the matter and the magnetic field. The trajectories of the propagated particles and the response of the detectors are recorded and written out. The package also allows to visualize the detectors and the particle trajectories. An example of a C+C collision at 2 AGeV is shown in *Fig. 3.1* at beginning of this chapter.

The simulation of particles traversing an experimental setup has to take into account the variety of the interactions of those particles with the material of the detector. GEANT is able to simulate the dominant electromagnetic processes which occur in the energy range from 10 keV to 10 TeV . For hadronic interactions the model does not extend below a few tens of MeV. In *Tab. 3.5* the processes which are currently implemented in GEANT are listed.

Originally, GEANT has been written in FORTRAN language, and it produced output files, in the form of PAW HBOOK format. Since the HADES software development is based on the C++ object-oriented language and the ROOT environment, it was necessary to develop an interface to be able to write GEANT output in ROOT-file format.

The HADES geometry data and media for the standard setup may be read in by HGEANT, either directly from an Oracle database or from file. To run simulations with HGEANT one has to set up the input file including a list of the paths to the current geometry files, media, field map, event files, and the name of the output root file. It is also possible to switch off any given physical process or the magnetic field.

For further analysis the output from HGEANT simulations is “digitized”, namely it is rendered into the form of raw data for each detector module, corresponding to the type of signal that would have been obtained in a real experiment. The main principles of the digitization for each particular detector in HADES are given in the next section.

Processes implemented in GEANT	
Processes involving the photon	e^+e^-pair conversion
	Compton effect Photoelectric effect Photo-fission of heavy elements Rayleigh effect
Processes involving e^+/e^-	Multiple scattering
	Ionization and δ-ray production Bremsstrahlung Annihilation of positrons Generation of Cherenkov light Synchrotron radiation
Processes involving μ^+/μ^-	Decay in flight
	Multiple scattering Ionization and δ-rays production Ionization for heavy ions Direct e^+e^-pair production Nuclear interaction Generation of Cherenkov light
Processes involving hadrons	Decay in flight
	Multiple scattering Ionization and δ-rays production Hadronic interactions Generation of Cherenkov light

Table 3.5: Processes currently implemented in GEANT.

3.3.1 Digitization

In this section digitalization as it is currently implemented in the HYDRA analysis environment is discussed. The details can be found for RICH in [23, 37], for MDC in [24], and for PreSHOWER in [38].

A GEANT simulation yields a complete description of the particle track in the detector, including interactions with detector materials. Digitization is the process of transforming this ideal information into a signal which is measured in an experiment. For this, the physical processes which lead to the signals read in each of the HADES detectors must be modeled.

The RICH signals are read out from the pads of the photon detector. Therefore, the RICH digitizer describes the process influencing charge on the pads due to the gain amplification of the photo electron. Cherenkov photons hit the CsI coating on the pad, where they may be absorbed with a simultaneous release of an electron. This electron then travels to the anode and initiates an avalanche.Each electron initializes an avalanche on the anode wire of the MWPC. The probability $P(Q)$ that an avalanche forms a charge Q is given by the Polya function which reduces to good approximation to $P(Q) = \exp(-Q/Q_{mean})$, where Q_{mean}= $1.2 \cdot 10^5$ e. The digitizer calculates the static charge induced on the pads close to the wire. Only the pads with a pulse above a threshold are stored for the analysis.

There is also another process possible that may lead to a signal on the anode wire. It is when a charged particle passes the gas of the photon detector and produces electrons along the path which lead to an avalanche on the wires. From GEANT simulations it is known what charged particle energy was deposited in the photo-detector volume and also the length of the track segment in the photo-detector. From the mean energy for electron-ion pair creation, which for CH_4 is 28 eV, it is possible to calculate the number of electrons created due to the photon passage. It is assumed that electrons are produced equidistantly over the whole track segment.

The MDC digitizer calculates from exact particle track position in an MDC layer the wire cell which has fired due to passage of this particle. The minimal distance to the sense wire is calculated from impact angle of the track. From GARFIELD simulations the drift velocity distribution in cell is known and the drift time to wire for the particle track defined by inclination angle and minimal distance is tabulated. From the apparent track length and position, the arrival time of electron cloud is derived. This distribution is folded with the response of the preamplifier and resulting signal is discriminated with realistic threshold. Since the TOF modules are scintilators, each particle that passes through produces photons that are reflected on the walls of the module until they are absorbed by a photocathode at the left or right end of the module. Experimental information consists of the time of flight of the particle at either side, and collected charge on each photocathode. The position of the crossing point of the particle trajectory and the module and the time of flight of the particle to this point are known from simulation. The photon propagation in the scintillator material is described by the group velocity v_g. Total time of the flight read on each side of the module is expressed as

$$time = Tof + \left(\frac{L}{2} + X_{module}\right)/v_g, \tag{3.3}$$

where Tof is the time of flight of the particle until it hits the module, L is the length of the TOF module, and X_{module} is the distance of the center of the module to the point where the particle crossed the module.

The time resolution σ_{time} depends on the number of photons deposited on the cathode:

$$\sigma_{time} = \sigma_o \exp\left(\left(\frac{L}{2} + X_{module}\right)/l_{att}\right), \tag{3.4}$$

where σ_0 is a constant, l_{att} is the attenuation length of the material.

The $time$ is sampled from a Gaussian distribution around the calculated value with variance σ_{time}. The second measured variable is the charge collected on the photocathode on either side. This charge is calculated from the energy loss in passing the module, photon yield in the material, and the quantum efficiency, and it also takes into account losses of photons due to absorption in the medium. In case of double hits the charge on the photocathode is the sum of the charges induced by both particles.As the measured time on left or right side of rod is considered always to be the shortest one from times corresponding to the each particle.

The PreSHOWER digitization is based on the fact that each charge particle passing the chamber results in an avalanche. The charge on the sense wires due to this avalanche, and the induced charge on the cathode pads, are calculated.

From the full particle track information from GEANT, it is possible to determine the sense wire in PreSHOWER closest to the track. This wire is then considered to be the one that fired. The charge accumulated on the sense wire Q_{wire} is calculated from an empirical formula

$$Q_{wire} = 4.18 \cdot \exp(-1.72 \cdot \beta), \tag{3.5}$$

where β is the velocity of the particle in units of speed of light.

In SQS mode, each particle going through a chamber liberates an avalanche of almost the same charge, weakly depending on β. The charge Q_{wire}induced on the wire is broadened according to a Gaussian distribution (FWHM = 60 %) to reflect the real detector resolution. The distribution of the induced charge on the pads is calculated numerically. A pattern matrix is created consisting of 1mm x 1mm square cells. The pattern matrix covers a 5x5 pad area. This pattern matrix contains the charge image on a plane 4 mm above the sense wires.

3.4 The simulation of the e^+e^- cocktail for C+C collisions at 1.0 and 2.0 AGeV

One of the first goals of the HADES experimental program is to revisit the measurement of the continuum region of the dilepton invariant mass spectrum from C+C collisions measured previously by the DLS experiment at the Bevalac, as it was mentioned in *Chapter 1*. In the year 2001, the HADES collaboration presented a proposal for a dilepton measurement in C+C and $\pi + p$ reactions [39], which was accepted by GSI. The details of the simulations for this proposal are presented below.

For our simulations, two beam energies have been chosen: E_{lab} = 1 AGeV measured also by the DLS experiment, and the maximum SIS energy of E_{lab} = 2 AGeV. The beam energy E_{lab} = 1 AGeV is below the threshold for η, ρ, and ω production, but E_{lab} = 2 AGeV allows sufficient production of η, ρ, ω, and eventually also of ϕ mesons.

The aim of the simulations was to estimate the total yield of dileptons which can be reconstructed from the data taken during a beam-time period of several days. Also the acceptance and resolution of the HADES setup with 3 MDC modules in each sector has been studied. The simulation allows to determine the yield from different dilepton sources separately. In *Chapter 1* it has been pointed out that the branching ratios for dilepton decays are small. Therefore, an enormous amount of events has to be simulated in order to obtain an invariant mass spectrum with a significant statistics which would correspond to the number of the measured events in several days. For example to obtain 1000 produced $\mathrm{e}^+\mathrm{e}^-$ pairs from the ω direct decay one needs 700 million of C+C semi-central events at 2.0 AGeV. For the energy of 1.0 AGeV one would even need a factor 10^3 more events. Such simulations would be an impossible task because of the limited resources of CPU time and disc space available. Therefore, instead of the simulation of full events with realistic particle multiplicities, each dilepton source has been simulated separately with high statistics with use of Pluto++ event generator. The final spectra were then constructed by adding the spectra from the simulated sources weighted with the expected parent particle yields. However, in the data analysis of events with realistic multiplicities there is not only one true pair in an event reconstructed, but also tracks from other sources. The random combinations of the leptons from different sources build a combinatorial background. The combinatorial background can be reconstructed by several methods. In *Chapter 5*, the method based on the like-sign pairs, that has been used for the analysis of the measured data in this work, is presented. In this simulation each source has been produced and analyzed separately and therefore for the estimate of total yield of the pairs, the combinatorial background should be estimated additionally. The main source of the combinatorial background are the π^0 induced decays. Therefore, the combinatorial background has been estimated from sample of 300 000 events with realistic π^0 multiplicities.

In Pluto++ the mesons can be produced with momentum distributions corresponding to a thermally equilibrated source. The energy spectra of particles with mass m emitted isotropically from a thermal source are characterized by the Boltzmann temperature T_B and follow

$$\frac{dN}{dE} = p \cdot E \cdot e^{-E/T_B}. \tag{3.6}$$

For the transverse mass (m_T) spectra of particles emitted at mid-rapidity Eq. (3.6) simplifies to [40]

$$\frac{1}{m_T^2}\frac{dN}{m_T} \approx e^{-m_T/T_B}, \tag{3.7}$$

where $m_T = \sqrt{(m^2 + p_T^2)}$. The generated mesons are decayed into $\mathrm{e^+e^-}$ pairs via Dalitz or two-body decays. Final events contain one $\mathrm{e^+e^-}$ pair per event from the simulated meson. Events with decays of π^0, η, ω, ϕ, and Δ have been produced. For each of the processes a sample of 50000 $\mathrm{e^+e^-}$ pairs has been simulated. The Boltzmann temperature T_B of the thermal source in Pluto++ has been chosen to be T_B(1 AGeV) = 55 MeV for the beam energy of 1 AGeV and T_B(2 AGeV) = 89 MeV for the beam energy of 2 AGeV [41], respectively.

The produced pairs have been propagated in HGEANT through the HADES geometry. The particles in HGEANT have been emitted from the center of the carbon target. The simulated data has been analyzed up to the HIT reconstruction and in each detector within the HYDRA analysis package. The status of the analysis in May 2001 has not allowed to performed a high level analysis used in the rest of this work. Thus a simplified analysis, a so called *PseudoTracking*, has been used. A particle has been considered as reconstructed by the *PseudoTracking* if the corresponding track number has been found in all hits in the following combination of detectors: RICH + MDC + TOF or RICH + MDC + TOFINO + SHOWER. Such defined method of reconstruction contains the geometrical acceptance and the reconstruction efficiency up to the HIT level. An $\mathrm{e^+e^-}$ pair has been reconstructed if both leptons that belong to the pair have also been reconstructed by the *PseudoTracking*. In analysis also an opening angle cut of $15°$ between the rings in pair has been applied.

The propagated particle in HGEANT carries the full information including the momentum of the particle. In the real data analysis, the momentum of the particle is reconstructed from the change of the trajectory in the magnetic field. It is possible to reconstruct the momentum of the particle within the precision of the applied momentum reconstruction method. Indeed, the finite resolution of the track position before and after the magnetic field reduces the precision of the momentum reconstruction. The best results could be achieved with the full HADES setup, where two modules of the MDC detectors before and after the magnetic field determine the precise position. The simulation has been done for a setup with three modules of the MDC, two modules before and one module after the magnetic field. With this setup the momentum resolution is $\Delta\, p/p[\%] \;=\; 1.0 + 3.6 \cdot\; p$ [GeV/c]. This gives for $\rho - \omega$ region resolution of 3-4%. The expected momentum resolution was simulated by smearing the ideal HGEANT momentum of the particle.

For each of the simulated processes an invariant-mass spectrum of the reconstructed pairs has been produced. In the cocktail simulation the following processes have been considered: π^0 Dalitz , η Dalitz , Δ Dalitz , ω direct and ω Dalitz decays, ρ direct decay, ϕ direct decay, and pn-bremsstrahlung. The pair production from the pn-bremsstrahlung was implemented to Pluto++ in such a way that the generated spectrum corresponds to the pn-bremsstrahlung of $\mathrm{e}^+\mathrm{e}^-$ pairs simulated within the UrQMD model. The dilepton sources used in this simulation are listed in *Tab. 3.6*.The branching ratios of dilepton channels has been listed in *Tab. 1.2* in *Chapter 1*.

	Beam energy			
Particle	1 AGeV	1.5 AGeV	1.75 AGeV	2.0 AGeV
π^0	$6.8{\cdot}10^{-2}$	1.24	1.49	1.71
η	$1.3{\cdot}10^{-3}$	$1.9{\cdot}10^{-2}$	$3.0{\cdot}10^{-2}$	$4.3{\cdot}10^{-2}$
Δ	1.02	1.86	2.24	2.56
ω	$4.8{\cdot}10^{-5}$	$1.4{\cdot}10^{-3}$	$2.9{\cdot}10^{-3}$	$4.8{\cdot}10^{-3}$
ρ	$4.8{\cdot}10^{-5}$	$1.4{\cdot}10^{-3}$	$2.9{\cdot}10^{-3}$	$4.8{\cdot}10^{-3}$
ϕ	$1.6{\cdot}10^{-6}$	$9.9{\cdot}10^{-5}$	$2.5{\cdot}10^{-4}$	$4.8{\cdot}10^{-4}$
pn-bremss.	$2.4{\cdot}10^{-4}$	$3.0{\cdot}10^{-4}$	$3.3{\cdot}10^{-4}$	$3.6{\cdot}10^{-4}$

Table 3.6: The averaged multiplicities for 40% central C+C collisions at 4 different beam energies and for all dilepton sources used in the cocktail simulations. The multiplicity of particles in central collisions is 2x larger compared to the minimum bias events.

Events with realistic π^0 multiplicities from the UrQMD model have been simulated and analyzed to estimate the combinatorial background. The estimate has been done for two limiting cases: *i)* after the rejection of all pairs with opening angles smaller than 15° recognized as two rings in the RICH only; *ii)* after the rejection of close lepton tracks with opening angles smaller than 15° (assuming ideal two-track resolution). The π^0 Dalitz pairs have average opening angle about $13\circ$ and the pairs from two body decays of vector mesons about $100\circ$. Therefore with 15° opening angle cut the most of π^0 Dalitz pairs is suppressed with respect to the pairs from two body decays from vector mesons.

In the first method the close pair that is found as one ring is not rejected. In the second method, the full track information from HGEANT is used to reject all close pairs even those which are found in the RICH as one ring. The realistic analysis that combines the information from the MDC hits described in *Chapter 4* rejects more than 90% of the close pairs and is therefore close to an ideal line. The combinatorial background has been constructed with the event mixing method.

As it was mentioned above, each analyzed event contained one $\mathrm{e}^+\mathrm{e}^-$ pair. The spectrum of all sources is sum of the reconstructed spectra from each source scaled with the product of the multiplicity of the source particle in event and the branching ratio to decay in $\mathrm{e}^+\mathrm{e}^-$ channel. The geometrical acceptance and part of the track reconstruction up to the HIT level is included in the analysis as it is described in the previous paragraph. Only the estimation of the reconstruction efficiency that comes from the higher level analysis including the hit matching and particle identification should be estimated. The total track reconstruction efficiency of $\mathrm{e}^+\mathrm{e}^-$ pair was estimated to be about 70%.

The multiplicities of all mesons produced per event have not yet been measured experimentally for SIS energies from 1 AGeV to 2 AGeV. This is actually one of the tasks of the HADES program. Some multiplicities had to be estimated. The cross sections of π^0 and η production at SIS energies were systematically measured by the TAPS collaboration for C+C, Ar+Ca, Ca+Ca, Ni+Ni, Kr+Zr, and Au+Au collisions [20, 33]. The measured cross sections were fitted as a function of the beam energy [20] and the collision system size [42]. *Fig. 3.7* shows the beam energy dependence. From this the average multiplicity of a given particle per event can be determined knowing its cross section and using

$$\sigma_{\pi^0,\eta} = \sigma_{tot} \cdot M_{\pi^0,\eta}, \tag{3.8}$$

where $\sigma_{\pi^0,\eta}$ is the measured cross section, σ_{tot} is the total cross section, and $M_{\pi^0,\eta}$ is the multiplicity of the measured meson per reaction. The total reaction cross section can be determined in a simple way as

$$\sigma_{tot}[fm^2] = \pi(R_t + R_p)^2 = (1.14)^2\pi(A_t^{1/3} + A_p^{1/3})^2 \tag{3.9}$$

where R_p^2, R_t^2 are the radii of the projectile and the target atoms, and A_p, A_t are the nucleon numbers of the projectile and the target atoms.

There have been several observations [33, 43–45] of the m_T-scaling of π^0 and η intensities at SIS energies down to 0.8 AGeV for heavy collision systems. This fact seems to be a general feature of heavy ion collisions in the SIS energy regime (see *Fig. 3.8*). The m_T-scaling predicts that the production of mesons is only a function of the transverse mass. This is expected to be valid also for vector mesons and can be taken as an assumption to estimate the vector meson cross section. Then the ratio of the integrated m_T-spectra for various particles is equal to the ratio of the cross sections. Each m_T-spectrum for different particles starts at different value due to the different rest mass of the particles. This is schematically shown in *Fig. 3.9*. From the known cross sections of π^0 and η and applying m_T-scaling we have estimated the expected cross sections for ω, ρ, and ϕ mesons. The values for ω and ρ were set to be equal. The multiplicity of Δ production is related to the π production in the ratio of 3/2. The multiplicity of pn-bremsstrahlung pairs was taken from the UrQMD simulations. *Tab. 3.6* summarizes the estimated averaged multiplicities of the sources used for C+C system at 1 AGeV, 1.5 AGeV, 1.75 AGeV, and 2.0 AGeV.

For the proposal the following event rate has been estimated. With the carbon beam intensity of $2 \cdot 10^6$ events/s and 1% interaction target, a first level trigger rate of $1 \cdot 10^4$ events/s is expected. The first level trigger condition $M_{TOF} + M_{TOFINO} \geq 2$, and $M_{TOF} + M_{TOFINO} \geq 6$ were evaluated. The latter reduces the rate by a factor of 2.5 in comparison to the first condition. The second level trigger brings an additional reduction of the taping and DAQ rate and the conservative factor of 10 leads to the final rate of

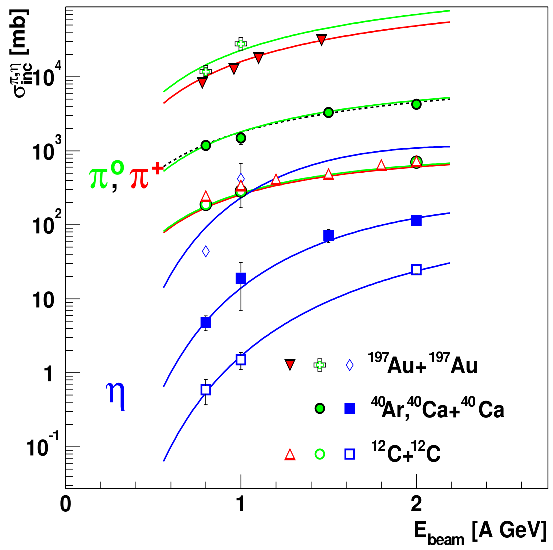

Figure 3.7: The inclusive cross section of the π° and η measured by TAPS as a function of the incident beam energy E_{lab}.

1.10^3 events/s. With the duty factor of 50% $2.16 \cdot 10^9$ LVL1 collisions can be measured in 5 days of beam-time. The expected yield for the $\mathrm{e^+e^-}$ pairs for 5 days of beam-time for C+C at 1 AGeV is shown in *Fig. 3.10* and for C+C at 2 AGeV in *Fig. 3.11*, respectively. Depending on the first level trigger condition for 1 AGeV the total yield of $\approx$ 25100-50300 $\mathrm{e^+e^-}$ pairs and $\approx$ 350-700 $\mathrm{e^+e^-}$ pairs in the region of region 200-600 $\mathrm{MeV/c^2}$ is expected. For C+C at 2 AGeV the total yield is a factor of 3.6 higher and in the region of 200-600 $\mathrm{MeV/c^2}$ the yield of $\approx$ 2100-4200 is expected. *Tab. 3.7* shows the yield of $\mathrm{e^+e^-}$ pairs from each dilepton source separately for one minimum bias collisions and one day of the beam-time for both beam energies. The *Tab. 3.8* shows the expected $\mathrm{e^+e^-}$ yield for five days beam-time for both energies and the first level trigger conditions.

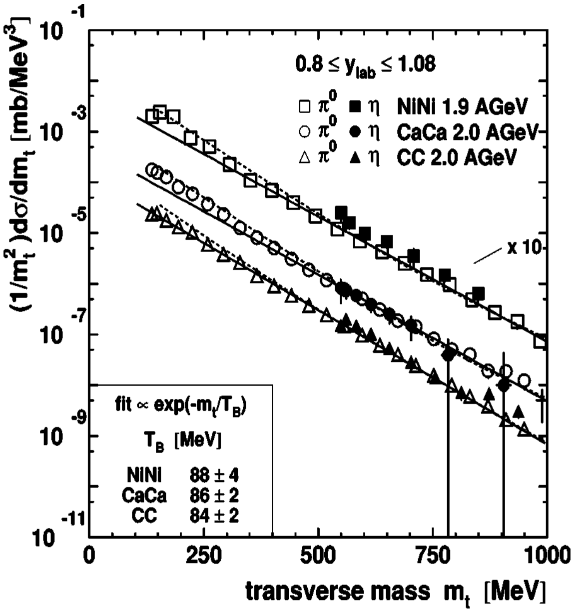

Figure 3.8: The impact-parameter inclusive transverse mass spectra of π^0 and η as observed in the systems C+C, Ca+Ca at 2 AGeV beam energy and in Ni+Ni at 1.9 AGeV measured by the TAPS collaboration. The solid line represents Boltzmann fits. The figure is taken from [46].

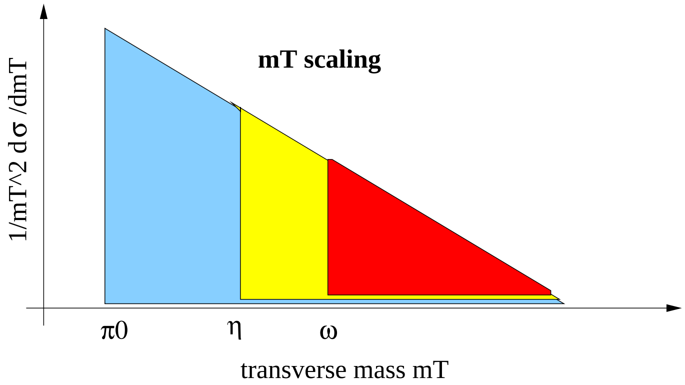

Figure 3.9: The schematic explanation of the m_T-scaling. The m_T spectra according to the hypothesis lie on the same line. This allows to estimate the cross section of other mesons, based on the line that it is measured for some of them.

	E_{beam} = 1 AGeV T_B = 55 MeV		E_{beam} = 2 AGeV T_B = 89 MeV	
Decay channel	$\langle M_{\mathrm{e}^+\mathrm{e}^-} \rangle$ [per collision]	$\mathrm{e}^+\mathrm{e}^-$ yield [per day]	$\langle M_{\mathrm{e}^+\mathrm{e}^-} \rangle$ [per collision]	$\mathrm{e}^+\mathrm{e}^-$ yield [per day]
π^0-Dalitz	$1.1 \cdot 10^{-5}$	$4.6 \cdot 10^{3}$	$3.7 \cdot 10^{-5}$	$1.6 \cdot 10^{4}$
η-Dalitz	$6.7 \cdot 10^{-8}$	$2.9 \cdot 10^{1}$	$2.2 \cdot 10^{-6}$	$9.7 \cdot 10^{2}$
Δ-Dalitz	$4.2 \cdot 10^{-7}$	$1.8 \cdot 10^{2}$	$7.6 \cdot 10^{-7}$	$3.3 \cdot 10^{2}$
ω-Dalitz	$4.6 \cdot 10^{-10}$	$2.0 \cdot 10^{-1}$	$4.4 \cdot 10^{-8}$	$1.9 \cdot 10^{1}$
ρ	$4.5 \cdot 10^{-10}$	$2.0 \cdot 10^{-1}$	$2.1 \cdot 10^{-8}$	9
ω	$2.3 \cdot 10^{-10}$	$1.0 \cdot 10^{-1}$	$2.0 \cdot 10^{-8}$	8
ϕ	$< 4.0 \cdot 10^{-11}$	0	$1.0 \cdot 10^{-8}$	4
pn-bremss.	$2.0 \cdot 10^{-7}$	$8.4 \cdot 10^{1}$	$4.0 \cdot 10^{-7}$	$1.7 \cdot 10^{2}$
comb. back.		$9.0 - 220.0 \cdot 10^{1}$		$2.3 - 57.0 \cdot 10^{2}$

Table 3.7: The $\mathrm{e}^+\mathrm{e}^-$ yields simulated for C+C collisions at 1.0 and 2.0 AGeV in the acceptance of the HADES spectrometer. The values are given for one minimum bias collision and for one day of beam time with a beam intensity of $2 \cdot 10^6$/s. The combinatorial background corresponds to the two limiting values given in *Fig. 3.10* and *Fig. 3.11*, respectively.

LVL1 Trigger	$\mathrm{e}^+\mathrm{e}^-$ invariant mass [MeV/c^2]	E_{beam} = 1 AGeV Yield in 5 days	E_{beam} = 2 AGeV Yield in 5 days
$M_{ch.p.} \geqq 2$	0-1200	25000	89000
$M_{ch.p.} \geqq 2$	200-600	350	2100
$M_{ch.p.} \geqq 2$	600-900	2	93
$M_{ch.p.} \geqq 6$	0-1200	50000	178000
$M_{ch.p.} \geqq 6$	200-600	700	4200
$M_{ch.p.} \geqq 6$	600-900	4	186

Table 3.8: The $\mathrm{e}^+\mathrm{e}^-$ yields simulated for C+C collisions at 1.0 and 2.0 AGeV in the HADES spectrometer acceptance and for 5 days of the beam-time. The values are given for collisions with LVL1 trigger condition $M_{ch.p.} \geqq 2$ and for semi-central collisions with $M_{ch.p.} \geqq 6$ condition and LVL1 trigger rate of 10^4/s. The yield of combinatorial background is not included. For an estimate see *Fig. 3.10* and *Fig. 3.11*.

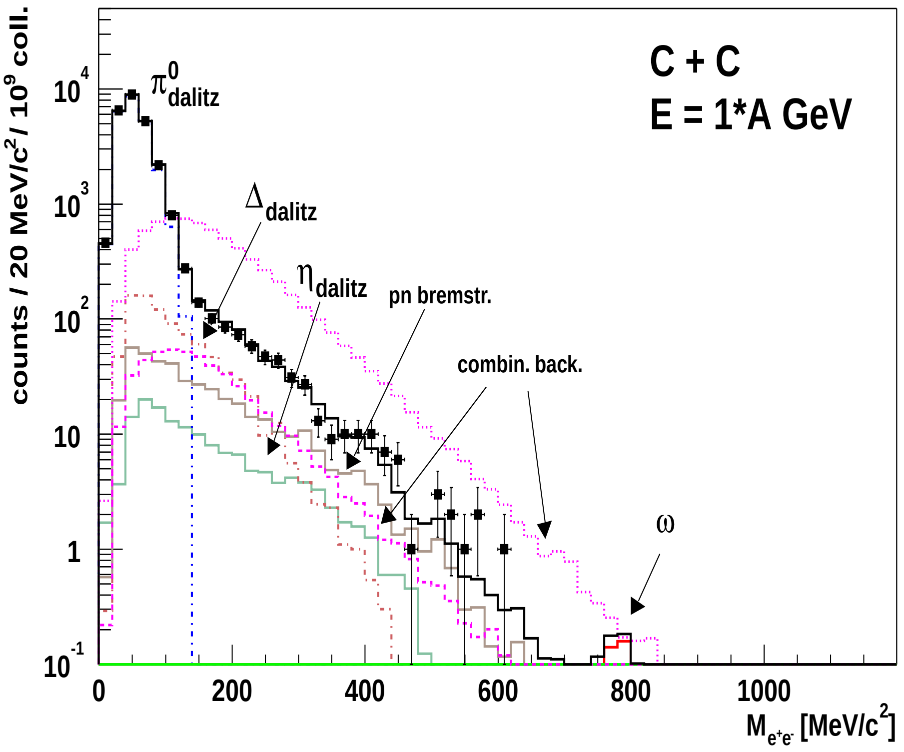

Figure 3.10: The simulated invariant e$^+$e$^-$ mass spectrum for C+C collisions at 1 AGeV beam energy. The spectrum corresponds to 210^9 semi-central collisions (40% of total cross section) for the HADES setup with 3 MDCs modules in the sector. The error bars reflect only statistical errors. Systematic errors are estimated to be about 30%. The combinatorial background is calculated for two limiting scenarios of the close pairs rejection, see text for details. The total yield of e$^+$e$^-$ pairs is obtained using the lower curve is expected to be $\simeq$ 50000 and is plotted as a solid line.

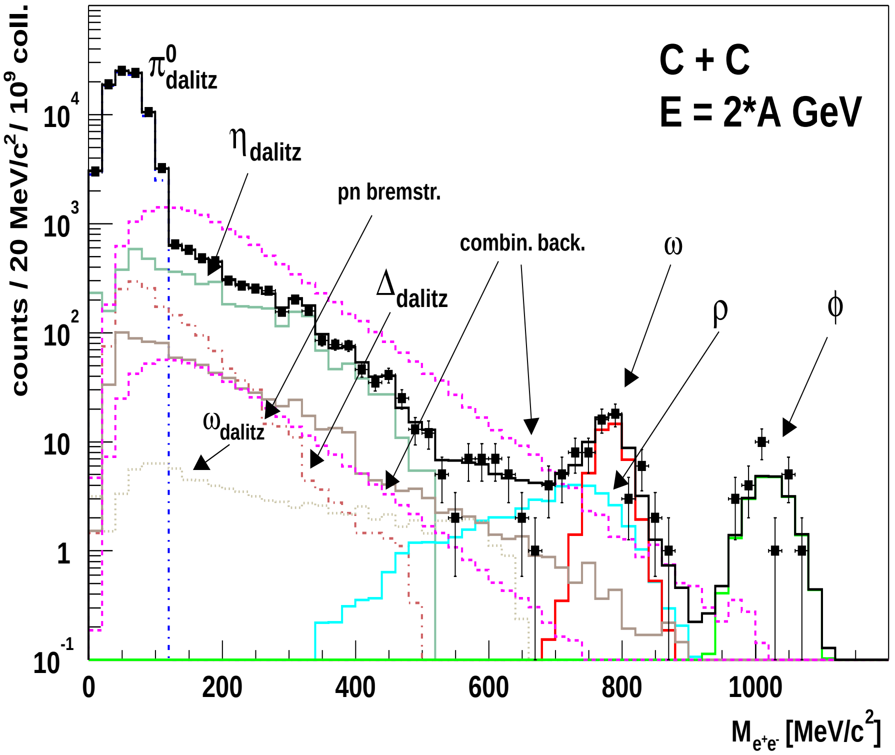

Figure 3.11: The simulated invariant e^+e^- mass spectrum for C+C collisions at 2 AGeV of beam energy. The spectrum corresponds to 2x10^9 semi-central collisions (40% of total cross section) for the HADES setup with 3 MDCs modules in the sector. The total yield of e^+e^- pairs is expected to be $\simeq$ 180000. For the errors and the combinatorial background explanation see *Fig. 3.10.*

4

Close pairs rejection in MDC

4.1 Introduction

The particle tracking algorithm combines the hits reconstructed in the detectors. The detectors have a limited granularity and if two tracks lie in space too close to each other there are not resolved as two separated hits. For the C+C collisions at 2 AGeV the multiplicity of the particles is small and it can happen with negligible probability for uncorrelated tracks. However the correlated leptons in $\mathrm{e}^{+}\mathrm{e}^{-}$ pairs from particle decays can have close tracks to each other. This is valid especially for leptons γ conversion pairs. Unresolved and unrecognized close tracks that are identified as one lepton track should be rejected from analysis before combining them with other tracks in the event, because all such combinations are fake pairs, these pairs do not correspond to decay of one particle. The method of rejection of the close tracks, so called close pairs is discussed in this chapter.

4.2 The γ conversion pairs.

The most frequently produced meson in C+C collision at 2 AGeV are pions, see *Tab.3.6*. Neutral mesons decay mostly to γ via $\pi^0 \rightarrow \gamma + \gamma$ (BR=98.8%). When photon passes through matter, it can in the vicinity of the another particle convert to an $\mathrm{e}^{+}\mathrm{e}^{-}$ pair: $\gamma \rightarrow e^{+} + e^{-}$. The participation of the another particle is necessary due to conversation of the total momentum. The produced pairs are called conversion pairs. The probability of the production of the conversion pair depends on the material and length of the trajectory of the γ in the material. The radiation length is the material parameter that characterizes conversion. It is defined as 7/9 of mean free path for pair production by photon ($E_\gamma \rightarrow \infty$). The radiation length of carbon (material used for target) is 18.8 cm [6].

Most of the momentum of photon is carried by the produced pair and because of the small lepton mass the opening angle of the created conversion pair is small. The average opening angle of conversion pairs created up to a distance of 30 cm from the target and flying into the HADES acceptance is $\alpha_{\mathrm{e}^+\mathrm{e}^-} = 2.4°$ (see *Fig. 4.1*). The magnetic field of HADES puts a cut on the momentum of accepted particles. Only particles with a momentum larger than approximately 50 $\mathrm{MeV/c^2}$ pass the field. The momentum condition on the leptons in the pair affects also their mean opening angle. For the pairs with at least one lepton with larger momentum than 100 $\mathrm{MeV/c^2}$ the averaged opening angle is $\alpha_{\mathrm{e}^+\mathrm{e}^-} = 1.6°$ and for pairs with both particles over 100 $\mathrm{MeV/c^2}$ the average opening angle is $\alpha_{\mathrm{e}^+\mathrm{e}^-} = 0.5°$. All conversion leptons that are produced between target and RICH mirror can be reconstructed in the analysis if they have large enough momentum to overcome the magnetic field.

Only 10% of the conversion pairs have large enough momenta to pass the magnetic field. In the analysis of the simulated data 65% of all leptons come from conversion pairs (see *Fig. 6.11*).Most of them come as expected from the carbon target and the RICH radiator gas C_4F_{10} (*Fig. 4.3*).

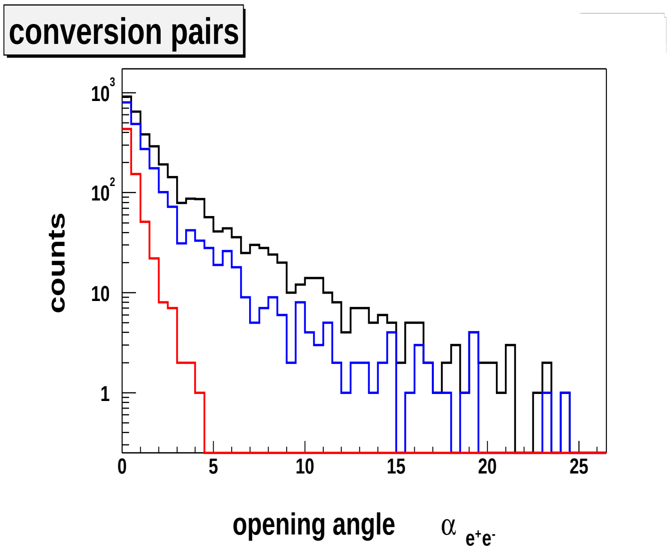

Figure 4.1: The opening angle distribution of conversion pairs produced within 30 cm from the target. All pairs in HADES acceptance (black line), those with $p > 100$ $\mathrm{MeV/c^2}$ (blue line) for at least one lepton in pair and those with $p > 100$ $\mathrm{MeV/c^2}$ for both leptons (red line) are shown. The corresponding values of average opening angles are: $\alpha_{\mathrm{e}^+\mathrm{e}^-} = 2.4°$, $\alpha_{\mathrm{e}^+\mathrm{e}^-} = 1.6°$ and $\alpha_{\mathrm{e}^+\mathrm{e}^-} = 0.5°$, respectively.

Due to the small opening angle of the conversion pairs it is possible that the close tracks of the electron and positron are resolved neither in the RICH nor in the inner MDC detector as separated tracks. If one of the leptons does not have sufficient momentum to pass the magnetic field and is bent out of the acceptance then this pair is considered as a single lepton track, because the double track piece before the field is matched with the META hit from the lepton that passed the field. Possible scenarios are schematically shown in *Fig. 4.2*. The combinations of these conversion tracks with other lepton tracks are fake pairs. These fake pairs result in a large combinatorial background to the correlated pairs if they are not rejected during the analysis.

A method of double-track rejection has been developed using the hit properties in the MDC detector and is described in the next section.

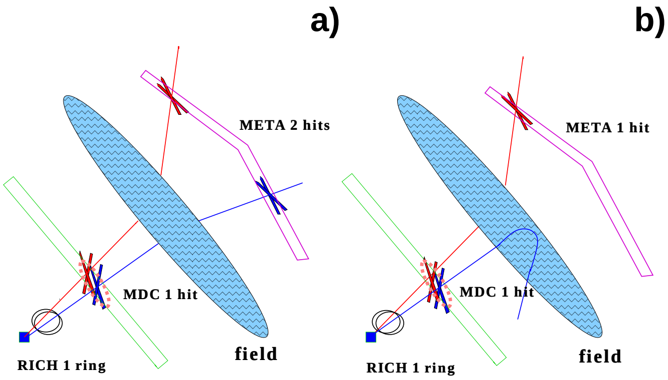

Figure 4.2: Schematic view of different close pair geometries (a) both leptons are reconstructed as full track (b) one lepton is lost in the magnetic field.

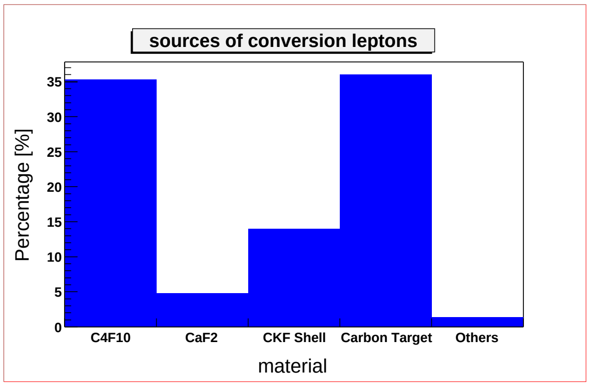

Figure 4.3: The conversion sources of leptons produced within 30 cm from target and that pass a RICH mirror and both inner MDC modules.

4.3 The properties of the conversion pairs in the MDC

In data analysis in this work the cluster finding method for reconstruction of the hits in MDC has been used, for details see *Section 2.4*. Two tracks can be reconstructed as one cluster (it means also as one hit) in a MDC module if they are too close to each other. The minimal opening angle that a pair would be reconstructed as two separated clusters is about $\sigma_\alpha = 1.5°$.

In a simulation it is however possible to identify which MDC hit corresponds to a single lepton track and which corresponds to the passing of a close e^+e^- pair,a double hit. For each cluster up to 5 different track numbers of particles that give signals on sense wires that contribute to the cluster is stored. For each such particle also the corresponding number of fired wires are stored. If in this particle list of MDC cluster corresponding to the hit, e^+e^- pair from the same decay is found then hit is considered to be a double MDC hit. In principle it is possible that also for two close, but separated clusters, the wires of one lepton contribute to the neighboring cluster. This false contribution to double clusters can be suppressed by a condition on the minimum amount of wires contributing to the cluster from both lepton partners to consider it as double. For selection of the doubles, a minimum wire multiplicity from each track of 3 has been requested. The clusters that contain only wires from one particle are called singles. There is a group of clusters that are neither singles nor doubles. These are clusters where to wires from one lepton track also some random wires from another track contribute and second track is not partner in pair. These clusters are called here mixed clusters.

65% of all reconstructed conversion leptons make a double hit in module 0 or module 1. Only 10% of the leptons from conversion make a single hit in both modules of MDC. Also pairs from other sources with small opening angle can be found as double hit in MDC. But if the average opening angle of the pairs from the process is large, than these pairs are a small part of the total amount. For π^0 Dalitz leptons about 20% make a double hit in one of the MDC modules.

The classification of leptons after all lepton cuts (see *Tab. 6.1*) by type of the cluster in both modules is listed in *Tab. 4.1*. The most frequent combination for electrons is with 33% the situation that in both modules of MDC there is double hit. In more than 50% at least in one module is a double hit.

In the sample of simulated data single and double clusters have been selected for lepton candidates (after *cut 0* of analysis in *Tab. 6.1*). It has been observed that values of the cluster size and number of contributing wires to the cluster is systematically larger in the case of double clusters compare to single clusters. These two parameters of the tracks turn out to be good candidates for a double track rejection algorithm. The distribution of the cluster size is shown in *Fig. 4.1* (picture (a) and (b)) for single (blue line) and double (red line) clusters. The distribution is plotted for clusters for tracks with $\theta \in (20° - 30°)$ (a) and $\theta \in (50° - 60°)$ (b) in module 0 and events where level of cluster finder was set to 5. *Fig. 4.1* (c) and (d) shows the distribution of the number of contributing wires to the cluster for single (blue line) and double (red line) shown for the same tracks. The number

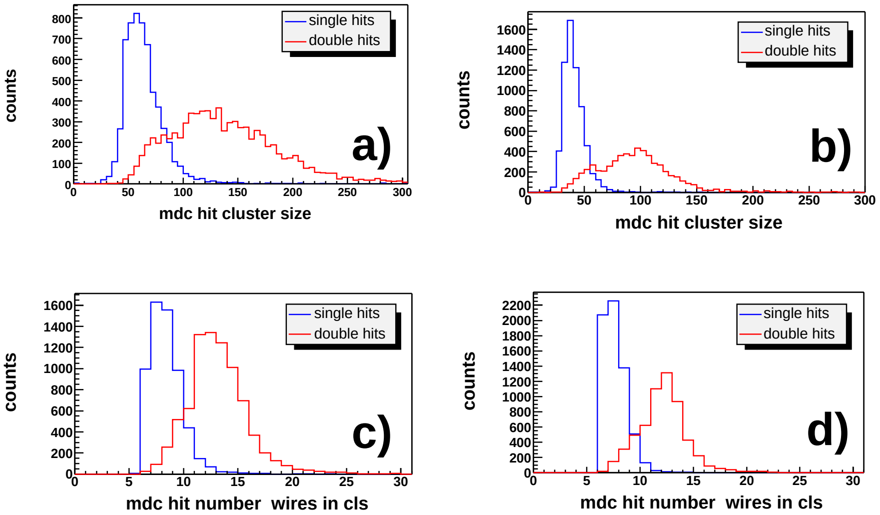

Figure 4.4: Simulated MDC single hits (blue) and double hits (red). (a) cluster size for hits $\theta \in (20 - 30)$. (b) cluster size for hits $\theta \in (50 - 60)$. (c) number of wires in cluster for hits $\theta \in (20 - 30)$ (d) number of wires in cluster for hits $\theta \in (50 - 60)$. The hits are selected in module 0 and events with level of cluster finding 5.

of the wires in the cluster shows similar systematic difference as the cluster size.

The cluster size and number of wires in cluster change as function of the polar and azimuthal angles of the track (see *Fig. 2.16* and *Fig. 2.17* in *Section 2.4*). In *Section 2.4* it has been explained that for various multiplicities of hits in a module of MDC, so called different level of cluster finder are used. The systematic comparison of the single and double clusters has been done for groups of clusters with similar angles and the same level of cluster finding. The phase space has been divided into 8 bins in polar angle $\theta \in (10^\circ - 20^\circ)$,$(20^\circ - 30^\circ)$,$(30^\circ - 40^\circ)$, $(40^\circ - 50^\circ)$,$(50^\circ - 60^\circ)$,$(60^\circ - 70^\circ)$,$(70^\circ - 80^\circ)$,$(80^\circ - 90^\circ)$, into 3 bins azimuthal angle $\phi \in (0^\circ - 10^\circ) + (50^\circ - 60^\circ)$,$(10^\circ - 20^\circ) + (40^\circ - 50^\circ)$,$(20^\circ - 40^\circ)$ and into each level of cluster finder ($level = 4, 5, 6$), finally each module of MDC ($m = 0, 1$) have been treated separately.

4.4 The construction of the probability to be single hit in MDC.

In our sample of all simulated data single and double clusters have been found. The distributions of cluster size and number of contributing wires in cluster have been constructed for clusters belonging to the same group of θ, ϕ and $level$ and MDC module m. From created histograms of the type shown in *Fig.4.4* the probability density functions Pdf^s, Pdf^d to be a single or a double cluster have been constructed as function of the cluster size or number of wires in cluster:

$$Pdf_i^s(v,p) = \frac{N_i^s(v,p)}{\sum_i N_i^s(v,p)} \tag{4.1}$$

$$Pdf_i^d(v,p) = \frac{N_i^d}{\sum_i N_i^d(v,p)} \tag{4.2}$$

where N_i^s and N_i^d is the multiplicity of the singles or doubles for the i-th bin of the histogram for $v =$ cluster size or number of contributing $wires$ in cluster and for value of parameters p defined by module $m = 0, 1$ of the MDC, angles θ, ϕ of the tracks.

The integrals of the Pdf functions defined by expressions 4.1 and 4.2 are normalized by definition to 1. Each bin contains the value that gives the part of clusters with cluster size (or number of wires in cluster) in this bin from all clusters of this type. The values of Pdf are non zero only for regions where the original distributions of parameter have non zero value. Outside of this region the value is 0. For example, for the cluster size distribution of singles in *Fig.4.4* (a) is the corresponding probability density function Pdf^s defined as non zero for cluster sizes from 20 to 150. For clusters with cluster size outside of this interval, another method is applied to decide whether the cluster is single or double, as it will explained at the end of this section.

For a particular lepton the information from each of two inner MDC modules is available. The cluster size and number of wires in the cluster in each of the modules is known. This information can be combined to decide whether the track is a single or a double.

The Bayes theorem to calculate probability that track is single has been used. For the track with MDC hit cluster size cls and number of wires in cluster nw the probability to be single is:

$$Ps(cls,nw,p) = \frac{N_p^s \cdot Pdf^s(cls,p) \cdot Pdf^s(nw,p)}{\sum_{t=s,d} N_p^t \cdot Pdf^t(cls,p) \cdot Pdf^t(nw,p)} \tag{4.3}$$

where $N^s(p), N^d(p)$ are the yields of singles and doubles for tracks with values of bin p defined θ, ϕ angles and level of cluster finding.

In *Fig. 4.5* an example of distribution of the probability that the cluster is a single $Ps(cls, nw, p)$ is shown for clusters with combinations of values of cluster size $cls \in (0-150)$ and number of wires in the cluster $nw \in (4-15)$ for $module = 0$ and clusters with angles $\theta \in (20^\circ - 30^\circ)$, $\phi \in (0^\circ - 10^\circ) + (50^\circ - 60^\circ)$ analyzed with $level = 5$ of cluster finder. The probability that a cluster is a single is close to one for clusters with combination of a small cluster size and a small number of wires in the cluster. For cluster with cluster size larger than 110 and number of wires in cluster larger than 11 is probability to be single is close to zero. This is in agreement to expectation from *Fig. 4.4,* (a),(c) where such clusters are predominantly double clusters. Two dashed lines with

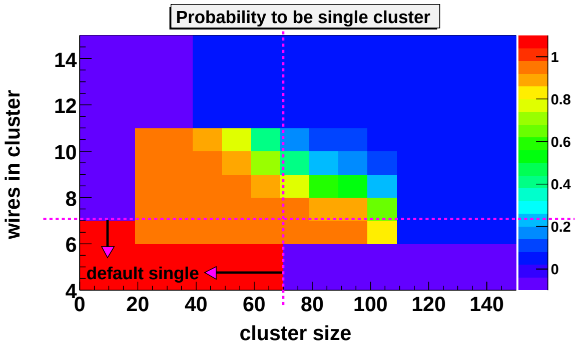

Figure 4.5: Example of the probability distribution to be a single cluster for clusters in $module = 0$ with $\theta \in (20° - 30°)$; $\phi \in (0° - 10°) + (50° - 60°)$, analyzed with $level = 5$ of cluster finder. The pink line indicates the region where in a case that Pdf function is not defined by default the cluster is identified as a single. Outside of this region the cluster would be a double.

arrows in *Fig. 4.5* circumscribe the region ($cls \leqq 70 \cap nw \leqq 7$) in which the cluster is by default single in a case that the Pdf function is not defined for values of cluster size and number of wires in the cluster. These default conditions have been determined from distributions of type shown in *Fig. 4.4* for each module and level of cluster finder in such way that almost no double clusters can be found with the parameters in this region.

4.5 Performance of the close pairs rejection method in MDC.

The method described in the previous section allows to calculate the probability that MDC hit for track of interest is single or double in each module. With this probability a decision about the track can be made. After investigation of various possibilities the following rule has been applied to the analysis of our data. An electron track is single if at least in one of the modules of MDC it has hit with given minimum probability to be single: it means $Ps_0 > P_{min}$ or $Ps_1 > P_{min}$. For each value P_{min} different amount of double clusters is rejected and single clusters is accepted. In general, if the value P_{min} is low, then the rejection of double clusters is also low because some of them fulfill the condition, but the acceptance of singles is very high, because only very few do not fulfill the condition. In opposite case of high value P_{min}, rejection power is high, as only few pass the condition, however larger amount of single clusters do not fulfill the condition and the single acceptance is smaller.

As it results from the probability distribution in *Fig. 4.5* the clusters that fulfill $Ps_0 > P_{min}$ condition have smaller cluster size and smaller number of contributing wires in cluster as those that do not fulfill the condition. In *Fig. 4.6* the distribution of cluster size

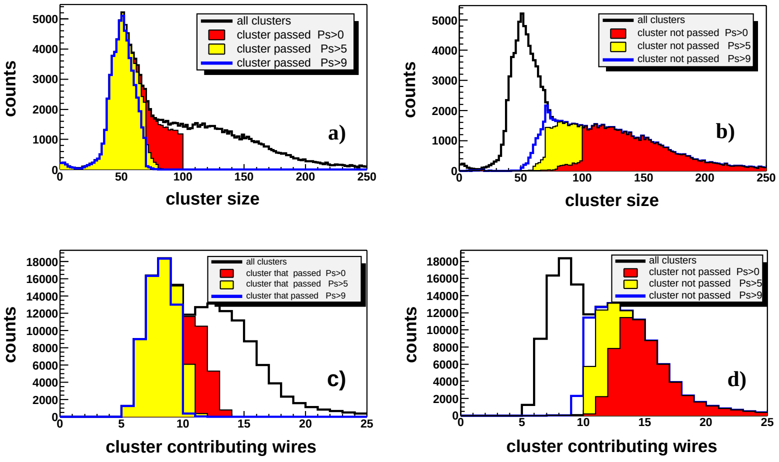

Figure 4.6: The cluster parameter distributions for clusters that fulfill (left) or do not fulfill (right) the minimum probability to be single with $P_{min} > 0$ (red area), $P_{min} > 0.5$ (yellow area) and $P_{min} > 0.9$ (blue line). The clusters are selected from lepton tracks in measured data in $module = 1$ with polar angles $\theta \in (20^{\circ} - 30^{\circ})$ analyzed with level of cluster finder $level = 5$.

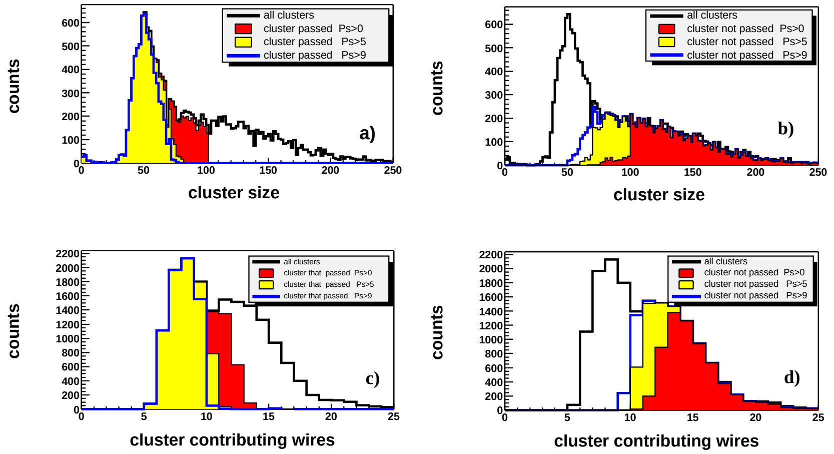

Figure 4.7: The cluster parameter distributions for clusters that fulfill (left) or do not fulfill (right) the minimum probability to be single with $P_{min} > 0$ (red area),$P_{min} > 0.5$ (yellow area) and $P_{min} > 0.9$ (blue line). The clusters are selected from lepton tracks in simulated data in $module = 1$ with polar angles $\theta \in (20^{\circ} - 30^{\circ})$ analyzed with level of cluster finder $level = 5$.

(upper 2 pictures) and the distribution of number of wires in cluster (lower two pictures) is shown for clusters that fulfill (always left picture) and for those that do not fulfill (always right picture) the condition $Ps_1 > P_{min}$ for the 3 different values P_{min}:$P_{min} = 0.0$ (red area),$P_{min} = 0.5$ (yellow area) and $P_{min} = 0.9$ (blue line). The pictures on left side show the accepted clusters and pictures on right side the rejected clusters. The clusters are selected from lepton tracks in measured data in $module = 1$ with polar angles $\theta \in (20^\circ - 30^\circ)$ analyzed with level of cluster finder $level = 5$. With larger value of P_{min} more clusters with higher values of both cluster parameters are rejected. The resulting distribution of the cluster parameters after $Ps_1 > 0.9$ (blue line, left picture) contains predominantly single clusters (compared to the distribution of single and double clusters in *Fig. 4.4*). For the sake of comparison, the corresponding picture for simulated data in *Fig. 4.7* is presented. The clusters for simulated and measured data show a similar behavior.

For each minimum probability to be single P_{min} applied to analysis using both modules, the double cluster rejection factor R_d can be defined as ratio between the part of double clusters that do not pass the condition and number of all double clusters in the sample. In a similar way also the single cluster acceptance factor A_s can be defined as ratio of the single clusters that pass the condition and number of all single clusters in the sample. In the ideal case both factors would be close to one. Another important parameter that characterizes the performance of the method, is the ratio of the single clusters to double clusters after applying the selection criterion. This ratio $S/B = \frac{N^s_{P>P_{min}}}{N^d_{P>P_{min}}}$ is called signal to background ratio.

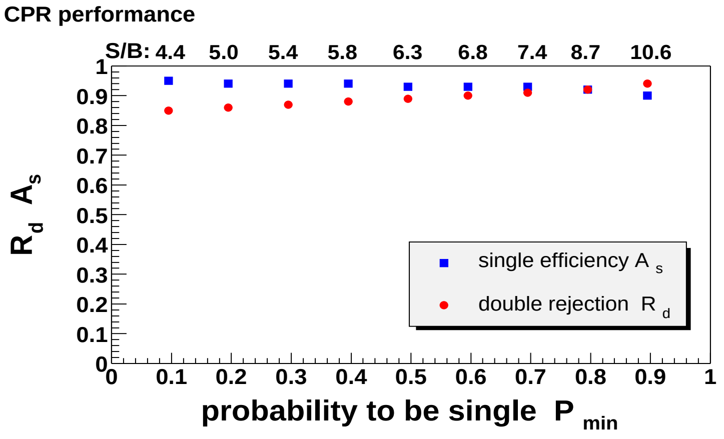

Figure 4.8: The performance of the CPR method to reject the double clusters. The double cluster rejection factor R_d (part of rejected double clusters) and single cluster acceptance factor A_s (part of accepted single clusters) is shown as a function of minimum probability to be single P_{min}. S/B is the corresponding ratio of single and double clusters after selection. The information from both modules has been used with condition $Ps_0 > P_{min}$ or $Ps_1 > P_{min}$ for single cluster decision.

In *Fig. 4.8* the values of R_d,A_s and S/B are shown for P_{min} from 0 to 1.0 with a step of 0.1. The points have been constructed by analyzing the sample of clusters from lepton tracks (after all lepton cuts, see *Tab. 6.1* in module 0 from simulated data for November 2001.In the analysis of the simulated and measured data the minimal probability $P_{min} = 0.9$ has been required. According to *Fig. 4.8* for this condition $R_d = 0.94$, so 94% of double clusters are rejected and $A_s = 0.90$, so 90% single clusters are accepted.

The classifications of the leptons from simulated data by type of the cluster in both modules is listed in *Tab. 4.1* also for leptons after the $Ps_0 > 0.9$ or $Ps_1 > 0.9$ condition. The most frequent combination after double clusters rejection for electrons is with 30.8% the situation that in both modules of MDC is single hit. The most frequent combination before the double hit rejection, double-double, has been suppressed from 33.4% to 6.5%. The overall performance of the double track (tracks with at least one double hit) rejection can be expressed with similar factors as for single-double cluster rejection in the previous paragraph. The overall double track rejection factor $R_{d.t.}$ (note different index) is the ratio of the number of tracks with double hit in MDC that are rejected after rejection condition to the number of such tracks before the rejection. The overall single track acceptance factor $A_{s.t.}$ is the ratio of the number of the tracks without double hit in MDC to the number of such tracks before the rejection. The group of the tracks that should not be rejected after cuts consists from s-s (single hit in $module\ 0$ - single hit in $module\ 1$), s-m, m-s and m-m tracks. It means that also mixed clusters, that are lepton clusters with some random contamination of uncorrelated track, have to be accepted. The overall signal to background ratio $(S/B)_t$ is ratio of number of accepted tracks without double hits and number with double hit after the rejection.

$$R_{d.t.} = \frac{N^{d-d}_{P\leq P_{min}} + N^{d-m}_{P\leq P_{min}} + N^{m-d}_{P\leq P_{min}} + N^{s-d}_{P\leq P_{min}} + N^{d-s}_{P\leq P_{min}}}{N^{d-d} + N^{d-m} + N^{m-d} + N^{s-d} + N^{d-s}} \tag{4.4}$$

$$A_{s.t.} = \frac{N^{s-s}_{P>P_{min}} + N^{s-m}_{P>P_{min}} + N^{m-s}_{P>P_{min}} + N^{m-m}_{P>P_{min}}}{N^{s-s} + N^{s-m} + N^{m-s} + N^{m-m}} \tag{4.5}$$

$$(S/B)_{t.} = \frac{N^{s-s}_{P>P_{min}} + N^{s-m}_{P>P_{min}} + N^{m-s}_{P>P_{min}} + N^{m-m}_{P>P_{min}}}{N^{d-d}_{P>P_{min}} + N^{d-m}_{P>P_{min}} + N^{m-d}_{P>P_{min}} + N^{s-d}_{P>P_{min}} + N^{d-s}_{P>P_{min}}} \tag{4.6}$$

,where $N^{t_0-t_1}_{P>P_{min}}$ is always the number of tracks with cluster of type $t_0 = s, d, m$ in $module\ 0$ of MDC and cluster of type $t_1 = s, d, m$ in $module\ 1$ of MDC with probability to be single $P > P_{min}$ for at least one of the clusters, $N^{t_0-t_1}$ is the number of all tracks of type $t_0 - t_1$ in the sample. The condition $P \leq P_{min}$ means the logical NOT of $P > P_{min}$.

The overall performance of the double tracks rejection determined with lepton tracks from simulated data, see *Tab. 4.1*, is $R_{d.t.} = 0.70$, $A_{s.t.} = 0.94$ and $(S/B)_t = 3.1$. It means that in the sample of the lepton tracks from simulated data during rejection 70% of the double tracks has been rejected, keeping 94% of single tracks in the sample. The ratio between single and double tracks in the final sample is 3.1 (compare to 0.97 before the rejection). In *Fig. 2.15* in *Section 2.4* the comparison of the cluster parameter distribution for measured and simulated data is shown. The distributions show very good agreement. Therefore it is reasonable to expect that the rejection mechanism works identically on measured and simulated data.

The method can be extended by using the additional information from RICH ring that belongs to the lepton track. It is expected that double rings would have different properties compare to single tracks. Another possible extension of the method is to study the shapes of the MDC clusters. These can bring additional improvement of the double rejection. The dedicated two tracks fitting of the MDC clusters will also bring a better two track resolution of the MDC and therefore also less tracks make a double hit.

	electrons		positrons	
mdc clusters	part of all [%]	part of all after CPR [%]	part of all [%]	part of all after CPR [%]
s-s	18.5	30.8	17.7	28.3
s-d	0.6	0.9	0.4	0.6
s-m	3.4	5.7	3.4	5.5
d-s	0.9	1.6	1.2	1.9
d-d	33.4	6.5	30.9	6.0
d-m	8.2	10.7	9.5	12.0
m-s	8.0	13.3	8.6	13.7
m-d	9.6	4.6	8.8	4.0
m-m	17.4	26.0	19.4	28.1

Table 4.1: Type of clusters for lepton candidates in simulated data. The type s-s means that in both MDC modules there were contributions from single lepton tracks to the cluster. The type d-d means that there were contribution from e^+e^- pair. The type m-m means that there were contribution from lepton track and some admixture from some other random track. The other types are combinations from these situations. The column 2 and 4 show the contribution of the specific type to all clusters for electrons and positrons.The columns 3 and 5 show the contribution of the specific type of the cluster after CPR cut with probability to be single larger 0.9 at least in one MDC was applied.

5

Combinatorial background

5.1 Definition of signal and combinatorial background

In final step of e^+e^- analysis a sample of electron and positron tracks from the data sample is identified . In one measured event we can find after analysis more that 2 lepton tracks. By combining unlike-sign e^+e^- lepton tracks in each event total $\mathrm{e}^+\mathrm{e}^-$ spectrum $N^{tot}_{e^+e^-}$ is constructed. In collision and following interactions leptons from several different sources can be produced and reconstructed. An important task is to reconstruct correlated e^+e^- signal $S^{corr}_{e^+e^-}$ that corresponds to pairs from physical decays. However there is no possibility to find out to which process particular lepton belongs. Therefore, dedicated statistical procedure has to be applied to subtract from all constructed pairs $N^{tot}_{e^+e^-}$ those that are consisting from uncorrelated e^+e^- pairs $N^{uncorr}_{e^+e^-}$. The total unlike-sign pairs spectrum $N^{tot}_{e^+e^-}$ consists of correlated pairs which are the real physical signal $S^{corr}_{e^+e^-}$ originated from the same decay, and of the uncorrelated unlike-sign pairs which are combinatorial background, made by pairing leptons from different decays:

$$S^{corr}_{e^+e^-} = N^{all}_{e^+e^-} - N^{uncorr}_{e^+e^-} \tag{5.1}$$

For construction of combinatorial background two methods can be used. Either so-called same event like-sign technique or different events mixing technique. An example of the comparison of the both methods in dilepton analysis can be found in [47]. In the analysis of the data in this work same event like-sign pairs method has been used to reconstruct the combinatorial background.

5.2 Same-event like sign pairs combinatorial background

The production of the correlated like-sign pairs $\mathrm{e}^-\mathrm{e}^-$, $\mathrm{e}^+\mathrm{e}^+$ requires higher order processes. The strongest of them is the $\pi^0 \rightarrow e^+e^+e^-e^-$ decay, that is suppressed by factor ≈ 380 [6] relative to the π^0 Dalitz and therefore is negligible for this analysis.

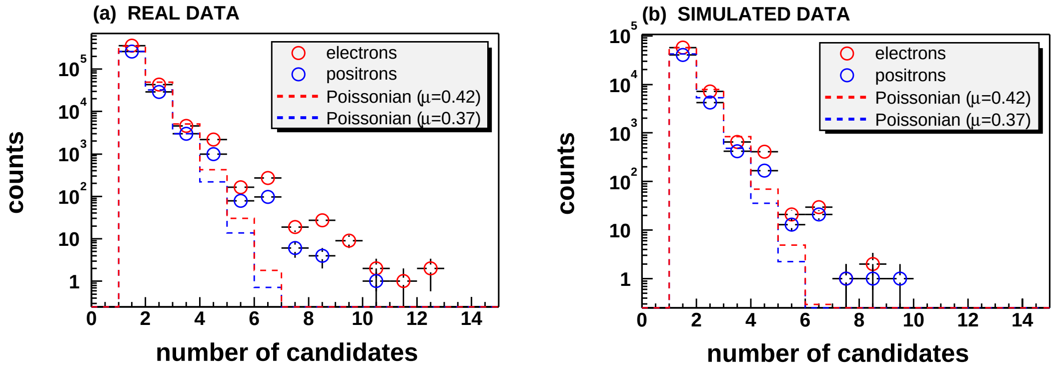

Figure 5.1: The multiplicities of electrons (red points) and positrons (blue points) per event in sample of measured (a) or simulated (b) events. The events with zero multiplicity has been filtered during the analysis. For a sake of comparison also the Poisson distributions with mean $\mu = 0.42$ (red line) and $\mu = 0.37$ is shown. The values of mean μ has been chosen such that average multiplicity of Poisson distribution corresponds to average multiplicity of electrons (resp. positrons) in sample.

The combinatorial background of $\mathrm{e}^+\mathrm{e}^-$ pairs can be calculated as

$$N^{uncorr}_{e^+e^-} = 2\sqrt{N_{e^+e^+}N_{e^-e^-}} \tag{5.2}$$

In next the derivation of the formula Eq.5.2 is presented following the steps in [47,48]. The multiplicity of the produced particle species in heavy ion collision is described by Poisson probability distribution P(N) for independent production. This is valid also for multiplicity of produced electrons N_{e^-} and positrons N_{e^+} in event. The multiplicity of the electrons and positrons in event for measured or simulated data is shown in *Fig. 5.1*. For sake of comparison also Poisson distribution is given. The mean of the Poisson distribution has been selected such that the mean of the Poisson distribution for multiplicities larger or equal one and mean of the corresponding electron (resp. positron) distribution is equal. Only events with multiplicity of electrons (resp. positrons) larger zero has been plotted in *Fig. 5.1*. The multiplicity of the produced leptons can be in 3 multiplicity bins described by Poisson distribution. For multiplicities equal or larger 4 the measured or simulated multiplicities differ from Poisson distribution. This difference is larger in measured data than simulated. This could be accounted to contamination of the fake lepton candidates in the sample.

If average multiplicity of leptons (in next e^+ or e^-) in event is $\overline{N}_l$ then probability $P(k)$ produce in one event k leptons is given:

$$P(k) = \frac{\overline{N}_l^k}{k!}\exp\left(-\overline{N}_l\right) . \tag{5.3}$$

Because of the limited geometrical acceptance and lepton reconstruction efficiency not all produced leptons are also observed. The probability ϵ_l to observe produced lepton is $\varepsilon_l = \varepsilon_l^{acc.}\varepsilon_l^{rec.}$. Probability to observe an electron ε_{e^-} and a positron ε_{e^+} can be different, because the presence of the magnetic field between inner and outer drift chambers. The probability to observe in event $n_l = k$ leptons from N_l produced is binomially distributed:

$$B(k) = \frac{N_l!}{k!\,(N_l-k)!}(\varepsilon_l)^k\,(1-\varepsilon_l)^{N_l-k}\ . \tag{5.4}$$

Making use of Eq. 5.4 one obtains the average number of reconstructed electron and positron tracks:

$$\begin{aligned} \overline{n_{e^+}} &= \varepsilon_{e^+}N_{e^+}\ ,\ \overline{(n_{e^+})^2} = \varepsilon_{e^+}(1-\varepsilon_{e^+})N_{e^+} + \varepsilon_{e^+}^2 N_{e^+}^2\ , \\ \overline{n_{e^-}} &= \varepsilon_{e^-}N_{e^-}\ ,\ \overline{(n_{e^-})^2} = \varepsilon_{e^-}(1-\varepsilon_{e^-})N_{e^-} + \varepsilon_{e^-}^2 N_{e^-}^2\ . \end{aligned} \tag{5.5}$$

The mean number of all $\mathrm{e^+e^-}$, $\mathrm{e^-e^-}$ and $\mathrm{e^+e^+}$ pairs in event with N_{e^-} electrons and N_{e^+} positrons is given by:

$$\begin{aligned} \overline{n_{e^+e^+}} &= \kappa_{e^+e^+}\sum_{k=0}^{N_{e^+}}\frac{k(k-1)}{2}\,B(k) = \frac{1}{2}\kappa_{e^+e^+}\varepsilon_{e^+}^2 N_{e^+}(N_{e^+}-1)\ , \\ \overline{n_{e^-e^-}} &= \kappa_{e^-e^-}\sum_{k=0}^{N_{e^-}}\frac{k(k-1)}{2}\,B(k) = \frac{1}{2}\kappa_{e^-e^-}\varepsilon_{e^-}^2 N_{e^-}(N_{e^-}-1)\ , \\ \overline{n_{e^+e^-}} &= \kappa_{e^+e^-}\sum_{k=0}^{N_{e^+}}\sum_{l=0}^{N_{e^-}} k\,B(k)\,l\,B(l) = \kappa_{e^+e^-}\varepsilon_{e^+}\varepsilon_{e^-}N_{e^+}N_{e^-}\ . \end{aligned} \tag{5.6}$$

The factor κ is the two-track efficiency of the pair. This must not be necessary equal for like-sign and unlike-sing pairs, because the charge asymmetry of magnetic field. Making use of Eq.5.6 the averaged number of the pairs in the event sample is:

$$\begin{aligned}
\langle n_{e^+e^+}\rangle &= \sum_{N_{e^+}=0}^{\infty} \overline{n_{e^+e^+}}\, P(N_{e^+}) \qquad (5.7)\\
&= \frac{1}{2}\kappa_{e^+e^+}\varepsilon^2_{e^+} \sum_{N_{e^+}=0}^{\infty} N_{e^+}(N_{e^+}-1)\, P(N_{e^+})\\
&= \frac{1}{2}\,\kappa_{e^+e^+}\,\varepsilon^2_{e^+}\left(\overline{N_{e^+}}\right)^2 ,\\
\langle n_{e^-e^-}\rangle &= \sum_{N_{e^-}=0}^{\infty} \overline{n_{e^-e^-}}\, P(N_{e^-}) = \frac{1}{2}\,\kappa_{e^-e^-}\,\varepsilon^2_{e^-}\left(\overline{N_{e^-}}\right)^2 ,\\
\langle n_{e^+e^-}\rangle &= \sum_{N_{e^+}=0}^{\infty}\sum_{N_{e^-}=0}^{\infty} \overline{n_{e^+e^-}}\, P(N_{e^+})\, P(N_{e^-}) = \kappa_{e^+e^-}\,\varepsilon_{e^+}\,\varepsilon_{e^-}\overline{N_{e^+}}\,\overline{N_{e^-}}\ .
\end{aligned}$$

In Eq.5.7 $\langle n_{e^+e^-}\rangle$ is unlike sign combinatorial background $N^{uncorr}_{e^+e^-} = \langle n_{e^+e^-}\rangle$ and it can be approximated as geometric mean of $\langle n_{e^+e^+}\rangle$ and $\langle n_{e^+e^+}\rangle$:

$$\begin{aligned}
\underbrace{\langle n_{e^+e^-}\rangle}_{\text{unlike-sign bg}} &\equiv \underbrace{2\sqrt{\langle n_{e^+e^+}\rangle\,\langle n_{e^-e^-}\rangle}}_{\text{like-sign bg}} ,\\
\kappa_{e^+e^-}\,\varepsilon_{e^+}\,\varepsilon_{e^-}\overline{N_{e^+}}\,\overline{N_{e^-}} &\equiv \sqrt{\kappa_{e^+e^+}\kappa_{e^-e^-}}\,\varepsilon_{e^+}\,\varepsilon_{e^-}\,\overline{N_{e^+}}\,\overline{N_{e^-}}\ . \qquad (5.8)
\end{aligned}$$

The equality Eq.5.8 is fulfilled if the two-track efficiency κ is the same for $\mathrm{e^+e^-}$, $\mathrm{e^-e^-}$ and $\mathrm{e^+e^+}$ pairs. The investigation of the pair detection efficiencies in HADES spectrometer [37] shows that there is only slightly higher recognition efficiency for unlike-sign pairs than for like-sign pairs.

5.3 The combinatorial background for C+C at 2AGeV.

The combinatorial background in the analysis of the data in these work has been reconstructed with like sign pairs method Eq.5.2. The details of the analysis up to reconstructed lepton pairs are given in *Chapter 6*. The reconstructed like-sign $\mathrm{e^-e^-}$ and $\mathrm{e^+e^+}$ spectra are shown in *Fig. 5.2*. For each bin of the spectra using Eq.5.2 the combinatorial background of unlike-sign pairs $N^{uncorr}_{e^+e^-}$ has been calculated. The combinatorial background from analysis of measured data after each step of the analysis is shown in *Fig. 5.3*. The opening angle like-sign pairs spectra show the correlation up to $\alpha_{op.} = 8^\circ$. This is presumably an artifact of the matching of the MDC and META hits in kickplane method. It can happen that MDC hit from one track in open $\mathrm{e^+e^-}$ pair is also matched with another META hit giving the wrong charge and then such track with another track in pair build correlated like-sign pair. The large opening angle cut $\alpha_{op.} = 8^\circ$ ($cut9$) has been applied to remove these pairs. After such cut, the shape of the combinatorial background follow expected behavior that it drops down for invariant masses less than 100 $\mathrm{MeV/c^2}$ (red line).

The analysis of the simulated data allows to compare the reconstructed combinatorial background with invariant mass spectrum of the uncorrelated pairs (using the full information about the particle in simulated data). According the *Fig. 5.4* the reconstructed combinatorial background for simulated data after all dilepton cuts, rather good describes the true combinatorial background. The ratio between the both spectra in *Fig. 5.5* is in most of the bins around 1. It means that true combinatorial background is correctly described by reconstructed one. For the pairs after all dilepton cuts (red circles), the largest difference is for the first two bins, where the reconstructed spectrum underestimates the true one by 40% and in bin 490-600 $\mathrm{MeV/c^2}$, where the true spectrum in overestimated by factor 2. In the other part of the spectrum, the reconstructed spectrum underestimate the real spectrum, but with less than 20%. The precise description of the spectrum is essential in part of the spectrum where the signal to background ratio is small. This is the part of the spectrum over π° mass. In a case of the weak signal even small error on background determination leads to large errors of the signal determination. In *Fig. 5.6*, the ratio of the difference of true and reconstructed background and reconstructed signal is shown after each cut of the dilepton analysis. The negative values of difference indicate the underestimation of the true combinatorial signal. For the spectrum after all cuts (red circles) it can be observed that there is about $5 - 10\%$ error on the reconstructed signal for the pairs with invariant mass up to 100 $\mathrm{MeV/c^2}$ where the most of the intensity of the π^0 Dalitz pairs is. In the region of the spectrum 160-490 $\mathrm{MeV/c^2}$ the error of the background determination is $40 - 80\%$ of the reconstructed yield of the $\mathrm{e^+e^-}$ signal. The reconstructed signal in this region of the $\mathrm{e^+e^-}$ invariant mass spectrum is by factor 2 overestimated as it will be discussed in *Chapter 6*. There has been no pairs produced in simulation with invariant masses larger than 500 $\mathrm{MeV/c^2}$ and all reconstructed pairs are due errors of the background determination and therefore will not be discussed.

The like sign pairs method as it has been used for reconstruction of the combinatorial background brings the limited precision, that is reasonable for reconstruction of the signal from π^0 Dalitz decay. The precise reconstruction of the signal from the other sources needs improvement of the reconstruction with smoothing procedure for example or using the event mixing method that reduce significantly errors due small statistics of the like sign pairs with high invariant masses.

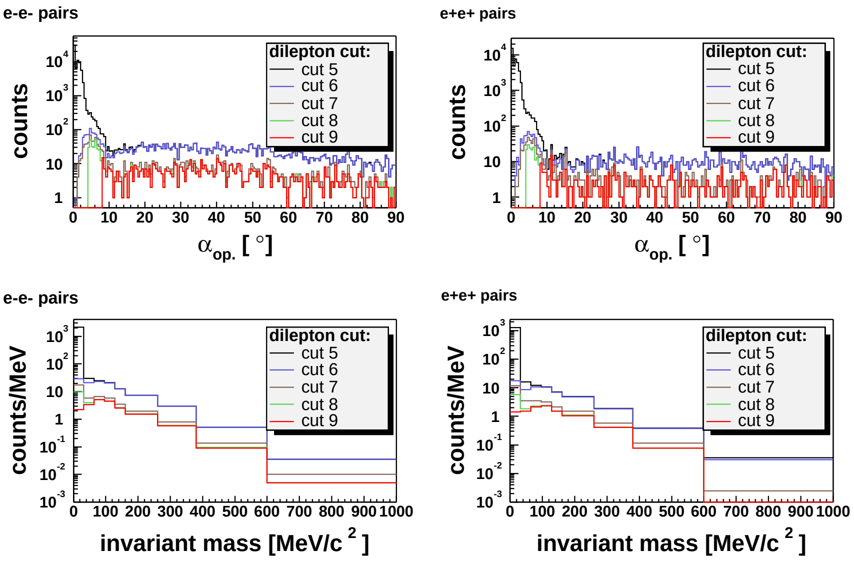

Figure 5.2: The invariant mass and opening angle spectra of the like-sign pairs from the analysis of measured data of C+C at 2 AGeV for all dilepton cuts.

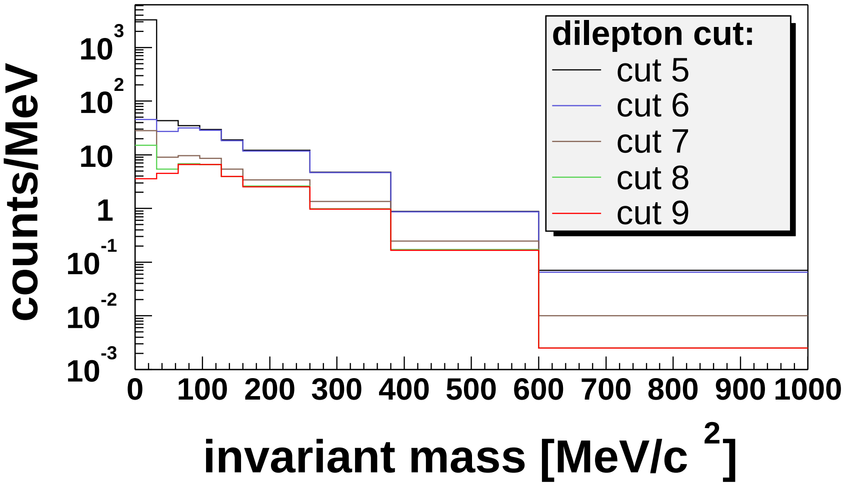

Figure 5.3: The combinatorial background spectrum reconstructed with like-sign pairs method for the measured data of C+C at 2 AGeV after each dilepton cut separately.

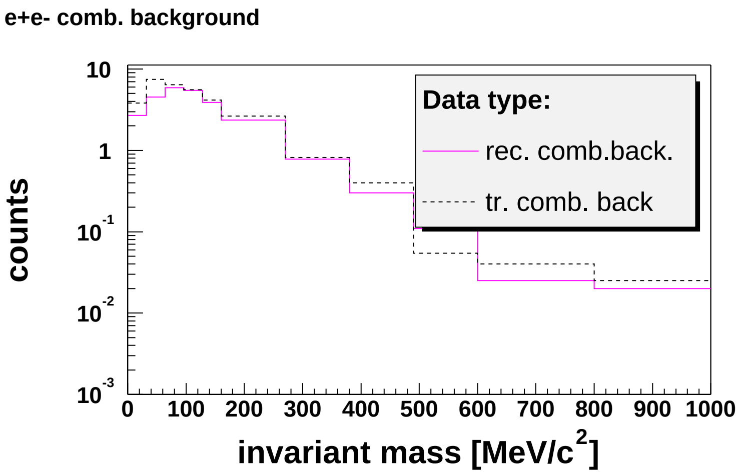

Figure 5.4: The comparison of the combinatorial background reconstructed with like-sign pairs method for the simulated data of C+C at 2 AGeV after all cuts and spectrum of true background. True background has been constructed for simulated data combining the leptons that are not pair from the same physical decay.

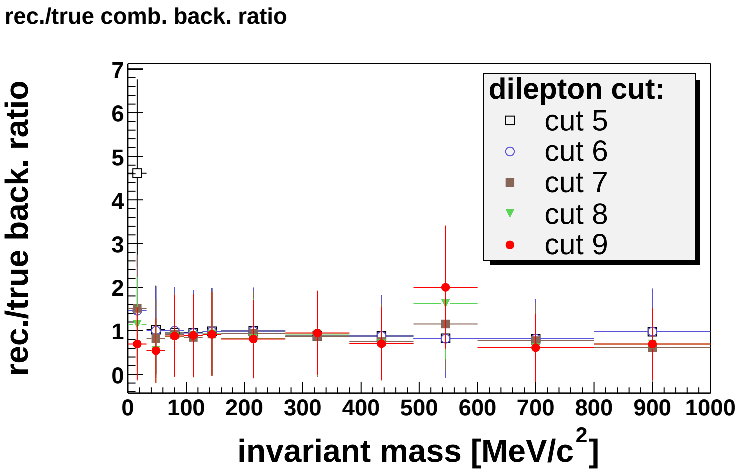

Figure 5.5: The ratio of the combinatorial background reconstructed with like-sign pairs method for the simulated data of C+C at 2 AGeV after all cuts and spectrum of true background, see *Fig. 5.4*. True background has been constructed for simulated data combining the leptons that are not pair from the same physical decay.

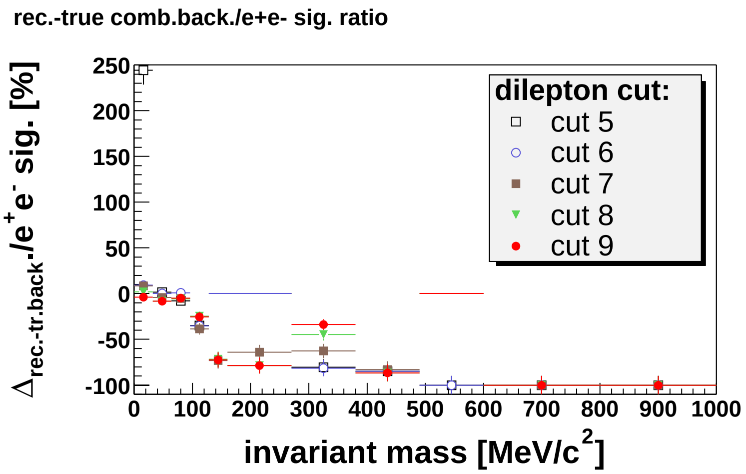

Figure 5.6: The ratio of the difference between true and reconstructed combinatorial background and the value of reconstructed e^+e^- signal. The combinatorial background is reconstructed with like-sign pairs method for the simulated data of C+C at 2 AGeV after all cuts, see *Fig. 5.4*. True background has been constructed for simulated data combining the leptons that are not pair from the same physical decay.

6

Dilepton analysis of C+C at 2 AGeV

6.1 Characteristics of the data set

In November 2001, there was a set of about 94 million first level triggered events taken on tape during the commissioning beam-time. The HADES experimental setup covered all six sectors equipped with inner MDC modules and sectors 0, 3, 4, and 5 covered with a MDC module 3. In the sector 0 there was also a module 4 installed. Since the performance of the outer drift chambers and the module 0 in the sector 0 was not stable during all beam-time, they have not been taken into account in the analysis and for the momentum reconstruction hits from the META detectors have been used. The measured system was C+C with beam energies of 1.0 and 2.0 AGeV. Part of the data has been taken with zero magnetic field ('no field data'), another part of the data has been taken with 11% of maximal strength of the magnetic field ('low-field data') and the largest part has been measured with 72% of maximal strength of the magnetic field with current I = 2497 A ('high-field data'). There has been a 5 mm thick carbon target used. The set of no field data has been used for an alignment of the chambers and detectors [49]. This thesis focuses on the analysis of the high-field data.

After quality assessment 45 million of events from days 338, 339, 340, 341, and 342 were chosen for the analysis. During these days, the data acquisition was rather stable and data was taken with similar conditions for all detectors. *Fig. 6.1* shows the lepton content of the data files as a function of time. Especially days 339–342 show very constant behavior. The lower multiplicity in part of the day 338 is due the fact that part of the data have been taken with 2 missing sectors of TOF detector. During the experiment the first level trigger condition was used. The collision should lead to a hit in the start detector and net multiplicity of photomutipliers with signal from TOF and TOFINO should be $(M_{TOF-PM} + 2 * M_{TOFINO-PM})/2 > 3$, for details, see *Section 2.6.4*. The Veto detector was not operational during the beam-time and therefore we restricted the analysis to events where the multiplicity of the START detector strips was one, to obtain the correct start time of the collision. The results presented in this work were

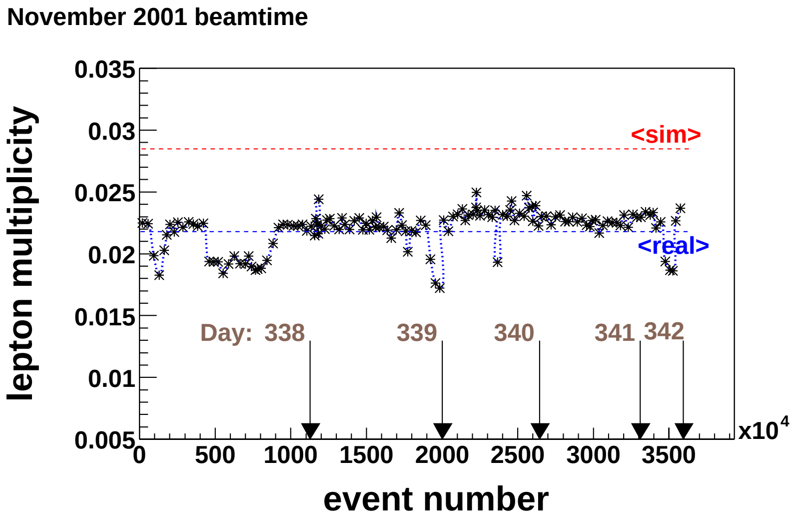

Figure 6.1: The averaged lepton multiplicity during the beam-time in November 2001 as a function of the event number. For each data file one point in the graph is plotted. The blue line shows the average multiplicity for whole beam-time and the red line shows the average multiplicity from the analysis of simulated data, respectively. The numbers 338-342 enumerate various days of the beam-time. The leptons were selected applying all lepton cuts.

obtained from analyzing a sample of 35 325 966 events with multiplicity of the charged particles larger than zero measured during November 2001 beam-time for the C+C system at 2 AGeV with 72% of the maximal strength of the magnetic field.

6.2 The analysis framework

For the analysis of the HADES data a dedicated analysis framework HYDRA has been developed by the HADES collaboration [50]. This framework is written in C++ language and uses the histograming package ROOT [36] as an integral part. The data are after unpacking stored in HCategories (for each detector separately). An example of HCategory is HMdcCal1 category that contains for each fired wire in the MDC detector time1 and time2, a number of the wire, a module to which the wire belongs, and a sector in which is this module. Each further analysis step is performed in the form of HReconstructor. This is a class that reads lower level category, performs an analysis step, and writes the output to the higher level of the analysis. In any moment it is possible to have access to the parameters, database through HRtDatabase, stored in Oracle, ROOT file or ASCII file. For parameters a powerful version management has been developed. An example of a HReconstructor is the MDC cluster finder HMdcClusFind. The analysis can start from *.hld file directly written by data acquisition or from ROOT file that already contains the

HCategories with data that are analyzed up to some step of the analysis. In general, after each step of the analysis only information relevant for physics analysis is stored reducing thus the volume of the data. For example after the HIT reconstruction in all detectors, the previous data categories are not stored anymore in the output, because the reduced information in the HIT category is sufficient for further analysis. The data presented have been analyzed with the version 6.12 of the HYDRA package.

6.3 The analysis steps

In *Tab. 6.1* all performed analysis steps are schematically listed. They can be divided into four logical parts. The first part a so-called **PreAnalysis** contains the selection of the good events (all detectors work under similar and stable conditions), unpacking and calibrating events, hit finding, alignment of the detectors, and momentum reconstruction. The data that are pre-analyzed with these steps are written out in a reduced form to DST (Data Summary Tape) root files. These DST files are used as a reference for further development of the analysis. After each significant improvement of the calibration, alignment or hit finding, a new *generation* of DST was produced. For results presented here the last *generation 6* of DST was used.

The second part of the analysis is the **Lepton Analysis**. Here a set of cuts (the selections of the particles fulfilling some conditions) is performed to reconstruct all tracks that correspond to the passing of leptons through the detectors. In the first step, *cut 0* the centers of the reconstructed rings in RICH with the MDC-META track pieces from Kick-Plane momentum reconstruction algorithm [50] are matched. The difference of the polar angle θ and the azimuthal angle ϕ of the rings and track pieces is used for matching as it is described in *Section 6.5.1*. The next step is *cut 1*, the selection of the tracks with the rings which fulfill four quality criteria, to reject the fake tracks that are constructed from fake rings randomly correlated with some MDC-META track piece. The selection criteria for the rings are described in *Section 6.5.2*. The step *cut 2* (see *Section 6.5.3*) operates on the tracks that contain in the META a hit in the PreSHOWER detector. Here a lepton PreSHOWER condition is applied. This condition selects the hits for which the corresponding sum of charge in 2 and 3 module of the PreSHOWER detector are larger by a factor of F than the sum charge in the module 1. This condition is momentum dependent and can separate lepton hits in the PreSHOWER detector from hadron hits. After this a selection on the velocity of the particles is applied in *cut 3* (see *Section 6.5.4*). The electron candidates should have in each momentum group of the particles the shortest time of flight from the target to the TOF or TOFINO detectors and therefore the highest velocity approaching the value of one. To suppress the contamination of the electron candidates that are build from the fake MDC-META track pieces we have applied an additional selection in *cut 4* (see *Section 6.5.5*) of the tracks with best values of the matching variable *Pull* .

The third part of the analysis is the **DiLepton Analysis**. In this part we construct from the leptons dilepton pairs by combining all leptons in a given event in *cut 5*. These $\mathrm{e}^+\mathrm{e}^-$ pairs contain either correct combination of the leptons corresponding to a true decay to $\mathrm{e}^+\mathrm{e}^-$ or it is a random combination of lepton candidates. The final aim is to identify those pairs that correspond to π^0 Dalitz and η Dalitz decays. To reach this, the pairs are cleaned in *cut 6* by removing such pairs that could not correspond to the true lepton pairs and are only artifact from a fake combination of HITS during the track reconstruction. These are the pairs that are built from leptons that have a common HIT in one of the detectors. Then all the pairs that contain a lepton that is probably constructed from a double hit in MDC are rejected. The criteria how to select the double hits from single ones were in details described in *Chapter 4*. This procedure rejects the combinations of true lepton with double track from γ-conversion pair. The rejection is performed in *cut 7* and the resulting tracks are dominated by true lepton pairs and random combinations of true lepton tracks. The pairs that come from γ-conversion and are reconstructed as two separated leptons have in average still a smaller opening angle than those from π^0 Dalitz and η Dalitz decays. Therefore, we can suppress them in a *cut 8* by applying an opening angle cut 4° and 8° in *cut 9*. We tabulate both opening angle cuts separately since later one also removes the correlated background visible for example in like sign pairs opening angle distribution which is an artifact of the fakes in the matching of the MDC and META hits due to a small granularity of the META detectors. As it was mentioned above, due to the absence of the outer MDC, the META hits are used for tracking and momentum determination instead.

In the last part of the analysis called **PostAnalysis**, using the like-sign pairs method the combinatorial background is constructed. This background can be subtracted from reconstructed unlike-sign dilepton pairs. The spectra obtained after this subtraction correspond to the yield of the $\mathrm{e}^+\mathrm{e}^-$ pairs mainly from particle decays. In the next Sections the cuts listed here are described in details.

6.4 The momentum reconstruction

The reconstruction of the momenta of the particles in this analysis have been done with ’kickplane plane’ method [50]. The particle momentum is obtained from the its deflection in magnetic field. For this the points in the front and behind magnetic field is needed. The MDC segments in inner modules in the front of the magnetic field and META hits behind magnetic field have been used. The effect of the deflection in the magnetic field is modeled by the 2D plane, that is constructed with help of the simulated data. The granularity of the META detectors is critical parameter of the precision of the deflection angle determination. In a case of TOF is the granularity in y-direction (perpendicular to beam axis in up-down direction) given by sizes of the scintillator rods: 2-3cm, in a case of PreSHOWER detector it is size of the pads that range from 3 to 4.5cm. It should be note here, that these detectors are not designed for precise position determination and they are use for this purpose only because of the missing outer drift chambers in this commission

The Analysis steps		
PreAnalysis - DST prod.	step 0	Unpacking/(Digitization for simulated data)
	step 1	Calibration
	step 2	Hit finding in all detectors
	step 3	The momentum reconstruction
Lepton Analysis	cut 0	The angular matching of the ring centers and kicktrack track pieces with $\Delta\theta = 1.7°\Delta\phi = 1.8°$
	cut 1	Selection of the tracks with minimum bias rings
	cut 2	Lepton condition in PreSHOWER detector
	cut 3	Momentum dependent 3 σ selection on velocity of the particles to get the fastest particles
	cut 4	Momentum dependent 3 σ selection on pull variable to get the tracks with best MDC-META matching
DiLepton Analysis	cut 5	Pairing all e^+ with e^- in event
	cut 6	The rejection of the pairs containing the tracks with common hits
	cut 7	Rejection of the pairs containing the tracks with $P_{sing.} < 0.9$ in both modules of MDC.
	cut 8	Rejection of the pairs with $\alpha_{open.} < 4°$. Also all pairs are rejected that contain leptons from such rejected close $\mathrm{e}^-\mathrm{e}^-$ pairs.
	cut 9	Rejection of the pairs with $\alpha_{open.} < 8°$. Also all pairs are rejected that contain leptons from such rejected close $\mathrm{e}^-\mathrm{e}^-$ pairs.
PostAnalysis	step 0	Construction of the combinatorial background using like sign pairs method
	step 1	Spectra generation

Table 6.1: The steps and cuts used in this work to analyze measured and simulated data. Both data are treated equivalently only step 0 of the PreAnalysis is different leading in both cases to the same format.

beamtime.

The momentum resolution of the used method is momentum dependent. The high momentum particle is in magnetic field deflected with smaller angle as lower momentum particle. Therefore the precision of the position determination behind the magnetic field is relatively more impact on momentum reconstruction of high momentum particles. The momentum resolution of the particles with the momentum 150 $\mathrm{MeV/c^2}$ is about 2$\%$, with 500 $\mathrm{MeV/c^2}$ is about 8$\%$ and with 1000 $\mathrm{MeV/c^2}$ it is about 15$\%$.

The matching of the hits in META and inner MDC should be done before the momen-

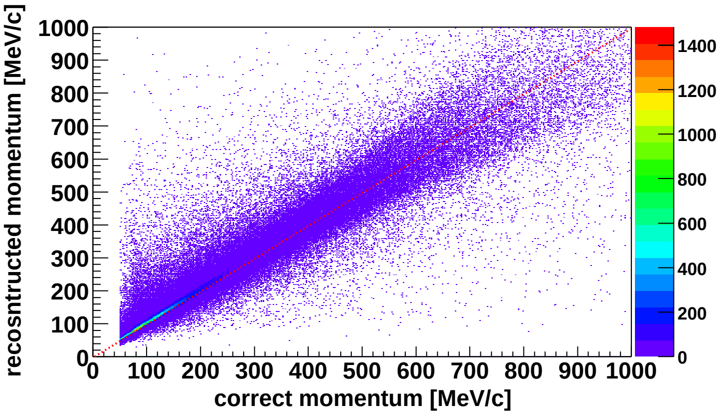

Figure 6.2: The reconstructed momentum of the leptons from simulated data versus the correct momentum from GEANT. The 'kickplane' method of momentum reconstruction has been used. As a position of the track in the front of the magnetic field inner MDC segment and behind magnetic field META hits have been used. Red line connects the points where reconstructed and correct momentum is equal.

tum for this track can be calculated. The matched MDC-META track pieces are called in this work also 'kicktracks', while they are found during this part of analysis. The particle track is uniquely defined by five parameters. There is four parameters defining the inner MDC segment and two parameters defining the META hit, it means we have one parameter too many. The x coordinate of the META hit can be chosen for matching. From the five parameters of the track (p, ρ, z, θ, ϕ) the x coordinate of the intersection of META x_c is calculated. One defines the variable $Pull$ as

$$Pull = \frac{x_c - x_m}{\sigma_{x_c - x_m}}, \tag{6.1}$$

where x_m is the x coordinate of the measured META hit. However, because of the low granularity of META detectors it is possible that one MDC segment is combined with several META hits. The amount of the such fake combinations will be reduced with presence of the outer MDC.

In *Fig. 6.2* the reconstructed momentum versus correct momentum for the reconstructed leptons from simulated data is shown. The momentum reconstruction is better for particles with small momenta.

6.5 The lepton analysis steps

6.5.1 The track matching

The first step of the analysis is to identify the hits in the detectors that can build the lepton tracks. The lepton track candidate is built from a ring in the RICH detector and then a segment in the inner MDC and the META hit after the magnetic field. If the outer drift chambers would be used in the analysis then also a segment from the outer MDC would contribute. The matching between the inner MDC segments and the META hits is done already by the kick plane algorithm for momentum determination in the DST production. Therefore, these kicktrack pieces are necessary to match with RICH rings. For matching the polar angle θ and the azimuthal angle ϕ of the MDC segments in the kicktrack and of the center of the ring is used. The matching condition was determined with a sample of 300 000 events where the difference of both angles for the rings and kicktracks has been plotted. *Fig. 6.3* and *Fig. 6.4* show these residuals distributions of θ and ϕ angles between all found rings and all reconstructed kicktracks. The residuals are fitted with a Gaussian function and quadratic background. The Gaussian width σ of the fit of the θ angle residuals was $\sigma_\theta = 0.85°$ and of the ϕ angle was $\sigma_\theta = 0.90°$. The background of the peak was investigated in simulation and it was found out that there is a probability that for the lepton track the real ring is reconstructed and also some fake rings about $5°$ away from the real one. These fake rings constitute together with random true ring-kicktrack combinations the background. The matching condition of rings and kicktrack pieces has been chosen to be 2σ for each angle. Correlations with fake rings are small in this window. The RICH ring and the MDC-META kicktrack belong to the one lepton track candidate if $|\Delta(\theta_{ring} - \theta_{kicktrack})| < 1.7°$ and $|\Delta(\phi_{ring} - \phi_{kicktrack})| < 1.8° \sin(\theta)$. The analysis of the simulated data shows that after this selection 76% of the lepton candidates correspond to the true lepton tracks (cf. *Tab. 6.7*)

6.5.2 The ring quality criterion

The reconstructed minimum bias RICH rings contain not only rings with ring centers corresponding to leptons tracks passing the radiator but also the fake rings which are product of the ring finder algorithm that combines not related fired pads to the fake ring or from the part of the related pads build a fake ring. The ring reconstruction algorithm provides several characteristics for each ring. Usually the fake ring have a lower quality than the real ones. A dedicated study of the RICH rings has been performed [37] and following criteria have been determined to separate the fake ring from a real one. For completeness the used criteria are listed: the ring is accepted if averaged integrated charge on pad in the ring is larger than 4, the quality parameter from the pattern matrix algorithm is larger than 200, the number of the pads that build the ring is larger than 5, and the ring centroid is smaller than 2.8. The ring centroid is defined as the distance between the calculated ring center and the center of mass of the ring. With these conditions 19% of all

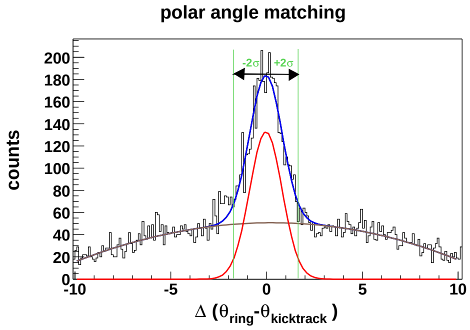

Figure 6.3: The definition of the matching of the ring centers and kicktrack MDC-META track pieces in polar angle.The residuals from 300 000 measured events have been fitted with a Gaussian function after the background subtraction. In analysis the matching of $2\sigma = 1.7^\circ$ was used (see green lines).

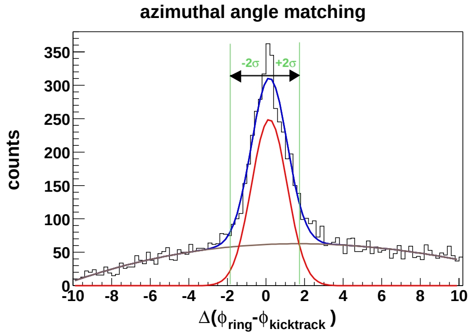

Figure 6.4: The definition of the matching of the ring centers and kicktrack MDC-META track pieces in azimuthal angle. The residuals from 300 000 measured events have been fitted with a Gaussian function after the background subtraction. In analysis the matching of $2\sigma = 1.8^\circ$ was used (see green lines).

tracks but only 2.5% with the true lepton rings are rejected. The analysis of the simulated data shows that after this selection 80% of the lepton candidates correspond to the true lepton tracks (*Tab. 6.7*).

6.5.3 The lepton PreSHOWER condition

The PreSHOWER detector allows an additional lepton identification. If an electron passes the 3 modules of the detector it produces an electromagnetic shower in the converter between the PreSHOWER plane and the two PostSHOWER planes. The PreSHOWER hit finder looks at local maximum of the charge distribution over all fired pads on the PreSHOWER pad plane. Then the charge of the surrounding 8 pads is added to the charge of the pad with the local maximum to get $Q_{PreShower}$. To each local maximum in the PreSHOWER module correspond 9 pads in both PostSHOWER modules. The integrated charge over those pads gives $Q_{PostShower1}$ and $Q_{PostShower2}$. If the ratios $F2(p) = Q_{PostShower1}/Q_{PreShower}$ and $F1(p) = Q_{PostShower2}/Q_{PreShower}$ are larger than a determined threshold then the hit corresponds to an electron. The response of the PreSHOWER detector to hadron and lepton candidates with different momenta has been investigated and momentum dependent threshold $F(p)$ has been determined [38]. *Fig. 6.5* shows the threshold functions $F2(p)$ (red line) and $F1(p)$ together with an example of the constant F = 1.9. The track candidate that does not fulfill the condition is rejected from further analysis. Indeed, for the leptons with low momenta there is a contamination from hadrons that fulfill also the PreSHOWER condition [38]. This contamination is shown on the left part of *Fig. 6.6*. For low energies the fake tracks are dominantly pions and for momenta above 500 MeV/c protons (see the right panel of Fig. 6.6). The analysis of the simulated data shows that after this selection 85% of the lepton candidates correspond to the true lepton tracks (*Tab. 6.7*).

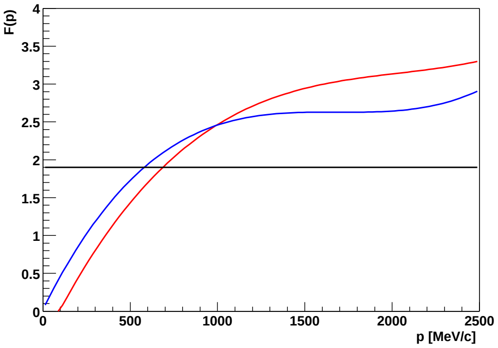

Figure 6.5: The PreSHOWER condition factor $F(p)$ as a function of momentum in PreSHOWER module 1 (blue line) and module 2 (red line). The particles for them the ratios between the charges for hits in the PreSHOWER modules 1,2 and module 0 are larger than value $F(p)$ are leptons.

6.5.4 The selection of the fastest particles

The rest mass of the electron is much smaller than the rest mass of the pion and proton. Therefore, the velocity of electrons is much higher than the velocity of hadrons with the same momentum. In HADES, there are two detectors, TOF and TOFINO, that measure the time of the flight *tof* of particle between the target and hit in the detector. From the

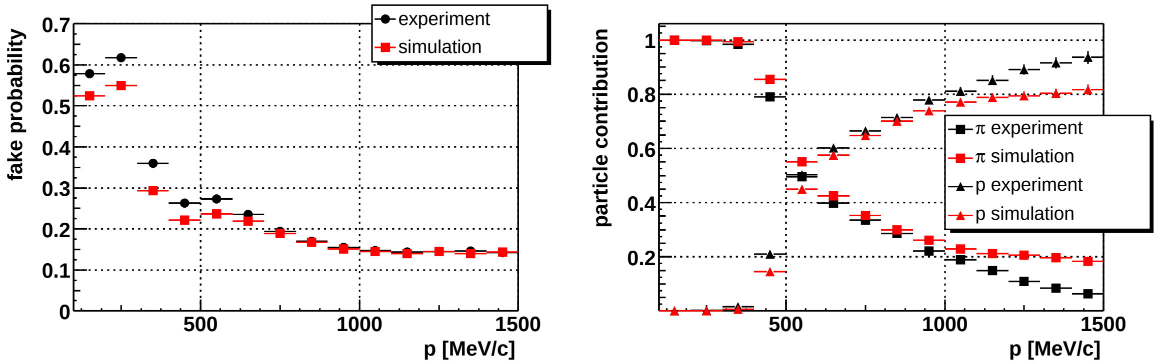

Figure 6.6: The contribution of the lepton fakes that fulfill PreSHOWER lepton condition as a function of the momentum of the particle.

position of the HIT we can calculate the distance to the target and with the knowledge of the *tof* we can calculate the velocity of the particle.

In *Fig.* 6.7 and *Fig.* 6.8 the distributions of the velocities of the lepton candidates that passed the **Lepton Analysis** cuts 0–2 are plotted. These distributions are shown for the particles in momentum groups, with a momentum step of 100 MeV/c between the groups. In each group we fit the velocity with a Gaussian function and in *Tab.* 6.2 we tabulate the mean values and the Gaussian widths σ of the fits. The value of the velocity is within 1 σ equal to the speed of light c, because the sample is already now dominated by leptons. The Gaussian width σ of the velocity distribution is smaller for higher momenta, because the velocity resolution of the high momenta particles is better. The granularity of the TOFINO detector, consisting only of four paddles per sector, is smaller than the granularity of the PreSHOWER detector. Even for light C+C collision system it is possible that more than one particle passes the TOFINO paddle in one event. Then the *tof* measured by the TOFINO detector is not correct and in general shorter than the true one. For such hits this leads to velocities larger than *c*. In simulations we have found out that 40% of leptons in the PreSHOWER detector are found out in such events. Therefore, the velocity condition used for the selection of lepton candidates in the PreSHOWER/TOFINO system was: $tof > tof_{mean} - 3\sigma$. The lepton velocity condition for tracks that contain a hit in the TOF detector was for each momentum range of particle: $tof_{mean} + 3\sigma > tof > tof_{mean} - 3\sigma$. The analysis of the simulated data shows that after this selection 91% of the lepton candidates correspond to the true lepton tracks (*Tab. 6.7*).

6.5.5 The selection of the tracks with the best MDC-META matching

In the kickplane method momentum determination the inner MDC-META track pieces are built by matching the corresponding hits [50], see also *Section 6.4* . The variable

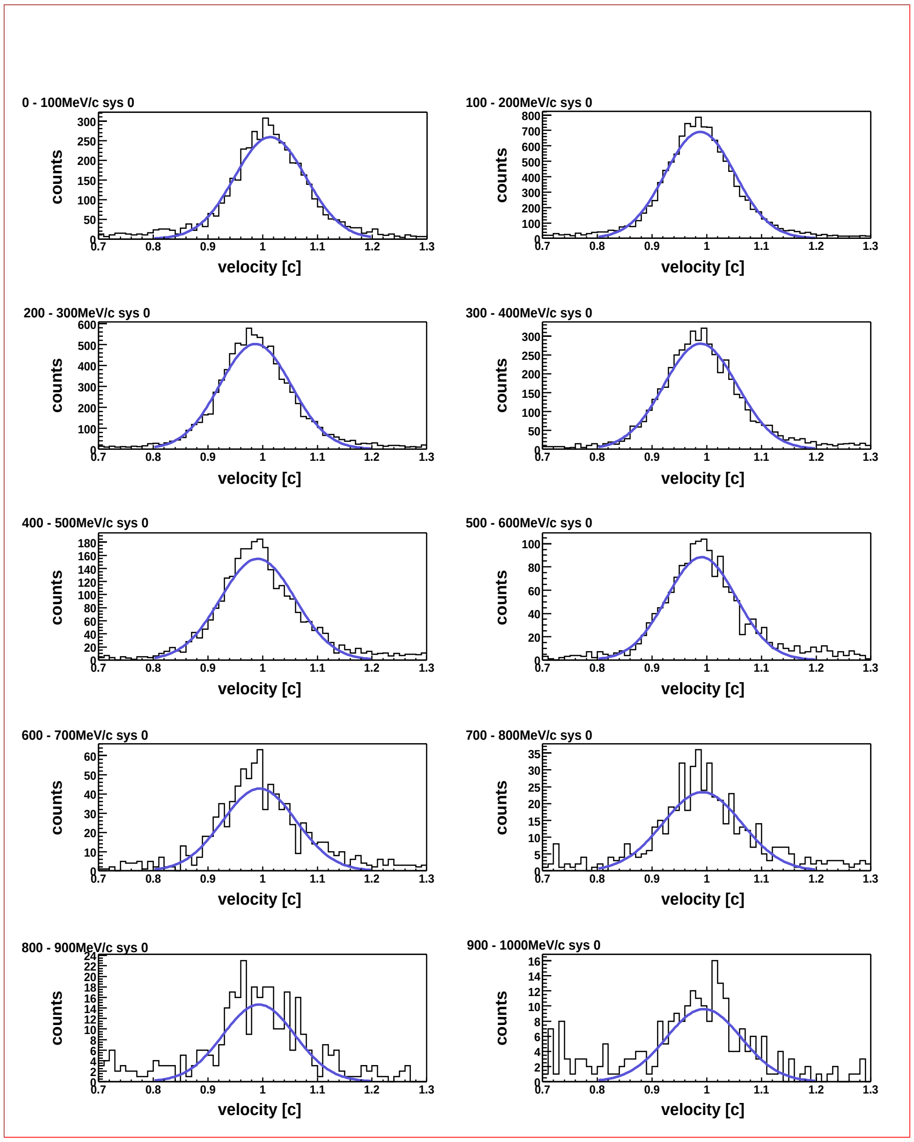

Figure 6.7: The fit of the velocity of the lepton candidates with a hit in the PreSHOWER detector.

characterizes the matching is Pull variable, defined by Eq. 6.1.

For the lepton candidates that passed the lepton selections *cut 0-3* the distributions of the Pull variable for momentum bins 100 MeV/c and for the TOF and PreSHOWER/TOFINO subsystems are plotted in *Fig.* 6.9 and *Fig.* 6.10. We fit the distributions to obtain the mean value and σ to be able to define selection conditions. The values of the fit are tabulated in *Tab. 6.4* for the measured data and in *Tab. 6.5* for the simulated data, respectively. For the momentum bins with small lepton statistics we did not fit the distribution and took the

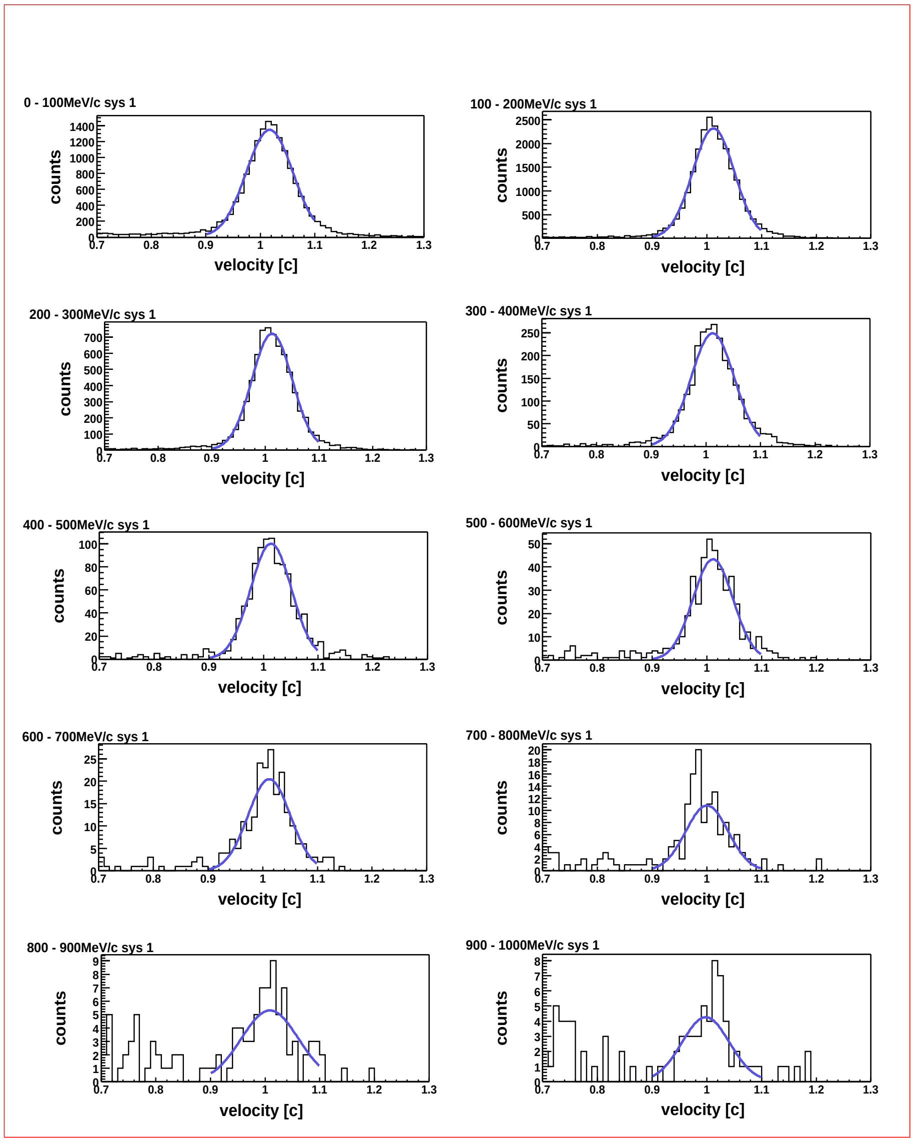

Figure 6.8: The fit of the velocity of the lepton candidates with a hit in the TOF detector.

values from the last momentum bin with enough statistics instead. The mean of the distribution lies as expected close to zero and σ varies for example for tracks with a TOF META hit from 2 to 1.4. For particles with higher momenta the deflection angle in the magnetic field is smaller than for those with small momenta and therefore also the matching is for them more precise and Pull variable have smaller values.

As an additional condition for lepton selection 3-σ cut was used. The tracks that have a $Pull$ value within 3-σ from mean of momentum bin were accepted. This selection

momentum [MeV/c]	TOF		TOFINO	
	mean velocity	$\sigma_{velocity}$	mean velocity	$\sigma_{velocity}$
0-100	1.0165	0.0424	1.0148	0.0646
100-200	1.0121	0.0380	0.9881	0.0633
200-300	1.0123	0.0379	0.9875	0.0656
300-400	1.0123	0.0396	0.9894	0.0658
400-500	1.0143	0.0359	0.9900	0.0678
500-600	1.0134	0.0382	0.9910	0.0623
600-700	1.0134	0.0395	0.9950	0.0672
700-800	0.9970	0.0333	0.9923	0.0742
800-900	1.0070	0.0388	0.9872	0.0764
900-1000	1.0060	0.0290	0.9942	0.0783

Table 6.2: The analysis of the real data. The parameters of the Gaussian fit of the velocity of the lepton candidates after cut2 for various lepton momentum groups. The fits are performed separately for the reconstructed leptons in TOF and PreSHOWER/TOFINO.

momentum [MeV/c]	TOF		TOFINO	
	mean velocity	$\sigma_{velocity}$	mean velocity	$\sigma_{velocity}$
0-100	1.0211	0.0248	1.0461	0.0778
100-200	1.0142	0.0233	1.0306	0.0710
200-300	1.0126	0.0234	1.0295	0.0706
300-400	1.0115	0.0240	1.0306	0.0722
400-500	1.0106	0.0244	1.0310	0.0637
500-600	1.0105	0.0253	1.0295	0.0688
600-700	1.0104	0.0213	1.0294	0.0699
700-800	1.0090	0.0215	1.0220	0.0697
800-900	1.0092	0.0218	1.0305	0.0674
900-1000	1.0074	0.0238	1.0290	0.0682

Table 6.3: Analysis of the simulated data. The parameters of the Gaussian fit of the velocity of the lepton candidates after cut2 for various lepton momentum groups. The fits are performed separately for the reconstructed leptons in TOF and PreSHOWER/TOFINO.

was used to suppress the fake lepton tracks coming from the kickplane method matching. Since it has no sense to put the $Pull$ cut smaller than the corresponding resolution of the x-positions determination from the TOF and PreSHOWER detectors, we have used 3-σ cut. This cut does not bring a very significant improvement of the purity of lepton sample in total but improves a bit the high momentum part which is visible as a difference of the red and yellow lines in *Fig. A.5*.

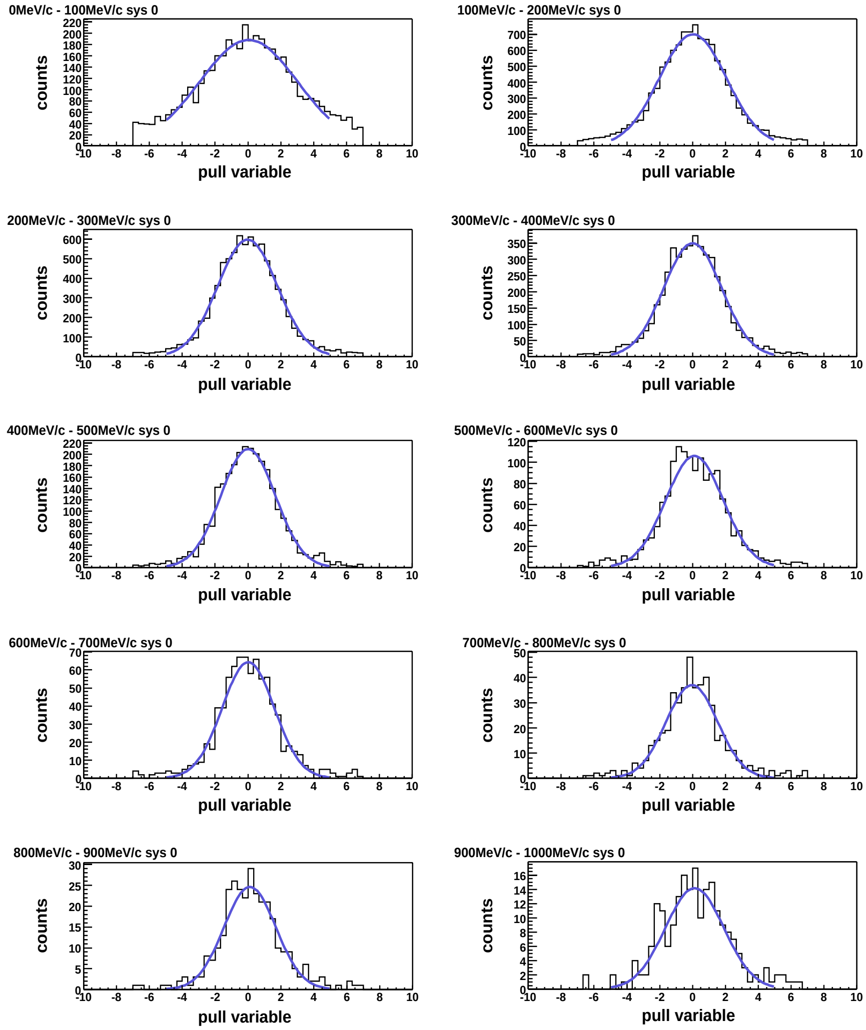

Figure 6.9: The fit of the $Pull$ variable of the lepton candidates with hit in the PreSHOWER detector.

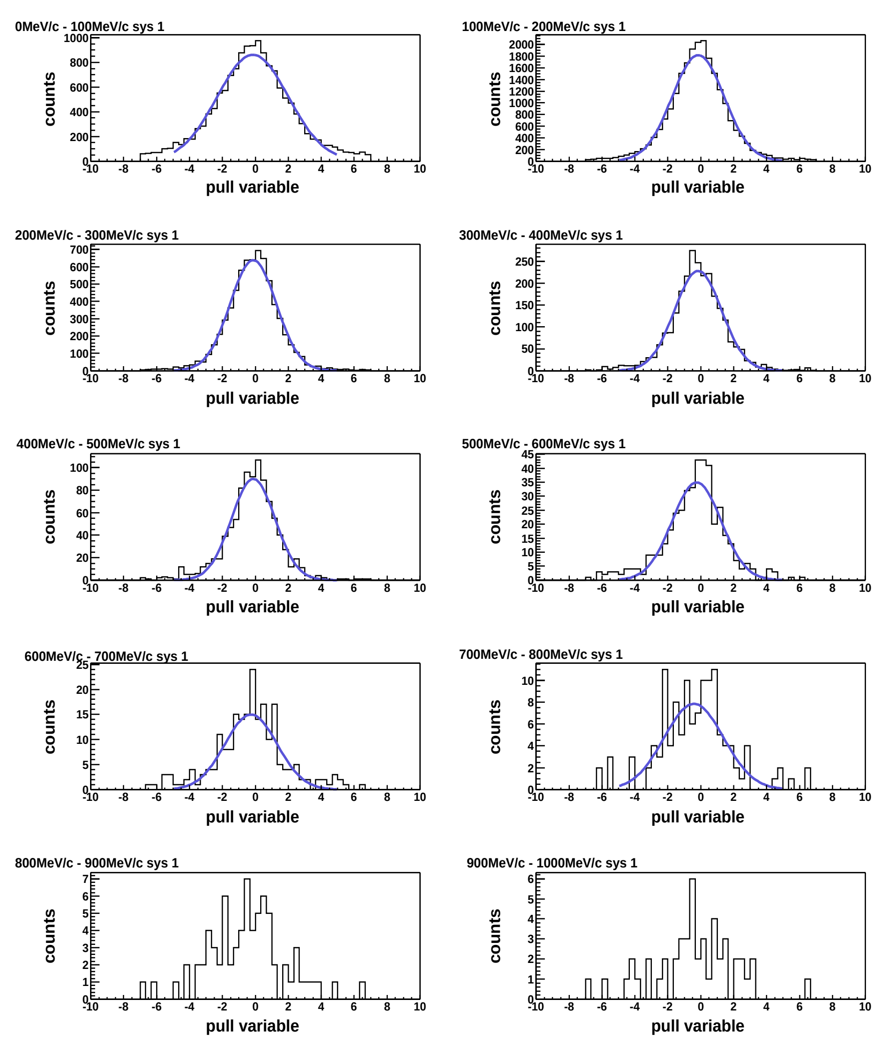

Figure 6.10: The fit of the $Pull$ variable of the lepton candidates with hit in the TOF detector.

momentum [MeV/c]	TOF		TOFINO	
	pull	σ_{pull}	pull	σ_{pull}
0-100	-0.16	2.15	0.10	2.97
100-200	-0.15	1.59	0.02	2.05
200-300	-0.12	1.41	-0.02	1.80
300-400	0.21	1.45	-0.01	1.77
400-500	-0.17	1.39	0.01	1.69
500-600	-0.23	1.49	0.09	1.77
600-700	-0.10	1.71	-0.02	1.58
700-800	0.00	1.71	0.05	1.60
800-900	0.00	1.71	-0.01	1.61
900-1000	0.00	1.71	-0.01	1.61

Table 6.4: The analysis of the real data. The parameters of the Gaussian fit of the $Pull$ variable of the lepton candidates after cut3 for the various lepton momentum groups. The fits are performed separately for the reconstructed leptons in TOF and PreSHOWER/TOFINO.

momentum [MeV/c]	TOF		TOFINO	
	pull	σ_{pull}	pull	σ_{pull}
0-100	0.01	2.45	0.03	2.75
100-200	-0.04	2.00	0.04	1.83
200-300	-0.02	1.82	-0.28	1.64
300-400	0.04	1.79	-0.01	1.53
400-500	-0.02	1.56	0.09	1.59
500-600	-0.03	1.31	0.08	1.40
600-700	0.17	1.38	0.08	1.45
700-800	0.17	1.38	0.05	1.60
800-900	0.17	1.38	-0.20	1.65
900-1000	0.17	1.38	-0.20	1.65

Table 6.5: The analysis of the simulated data. The parameters of the Gaussian fit of the $Pull$ variable of the lepton candidates after cut3 for the various lepton momentum groups. The fits are performed separately for the reconstructed leptons in TOF and PreSHOWER/TOFINO.

6.6 Single lepton spectra

As it was mentioned in *Section 6.1*, there were about 35 millions of events with a multiplicity of at least one charged particle selected for analysis. The events with at least one charge particle have been selected such, that the multiplicity of the kicktrack (MDC-META track pieces) is for these events larger than 0.

The all analysis steps described in *Section 6.3* have been applied to obtain the electrons and positrons from the data sample. The multiplicities of the lepton candidates that fulfill each step of the lepton analysis are tabulated in *Tab. 6.6* for measured data. There were 450674 electrons and 319956 positrons found. This is in average 2.18x10^{-2} leptons per one event with at least one charged particle. *Fig. 6.1* at the beginning of this chapter shows the average multiplicity of leptons in the measured data. Each point in the graph corresponds to one data file. The lepton content in the data has not been constant during the beam-time. On day 338 there were approximately 20% fewer leptons per event than is the average value, due missing sector 2 and 5 of the TOF for part of the measurement. The rest of the data shows a constant behavior.

Each applied lepton cut reduces the number of lepton candidates in the sample, because of the suppression of the contribution of tracks that are not real leptons, but fake candidates. The fake candidates are either random combinations of the rings with the hadron track pieces in MDC-META or with the track pieces MDC-META that do not correspond to any true particles (fakes from matching in the kickplane method). The hadron fakes could be suppressed by stronger lepton conditions but the fakes from the matching in the kickplane method are in principle not possible to be removed in the case that a META hit corresponds to another electron candidate. This problem will not be present in the analysis of data where at least one outer chamber is present. The position resolution of the outer drift chambers is much better than that of the META detectors.

The analysis of the simulated data (16 973 392 events), summarized in *Tab. 6.7*, shows that the purity of the lepton candidates increases from originally 76% after *cut 0* to 91% after applying all lepton selection criteria *cut 0-4*. The purity of the electrons candidates is 93% and is higher than the purity of the positron candidates which is 89%. There are two reasons for the lower purity of the positrons. The first one is that for positrons there is an additional contribution to the background from protons which is not present for electrons. The second reason is a different geometrical acceptance of leptons. The larger part of the positrons is detected in PreSHOWER/TOFINO while reconstructed electrons are mostly detected in the TOF system. Therefore electrons must fulfill more precise velocity condition. However, already after the track matching in *cut 0* the purity of the electron candidates is by 13% better than for positrons, because of the first mentioned reason. The PreSHOWER lepton condition in *cut 2*, that works dominantly for positrons due to their geometrical acceptance, reduces this difference.

The sources of reconstructed leptons from analysis of the simulated data are shown in *Fig. 6.11*. Most of the reconstructed leptons come from γ conversion , namely 65%. The second most probable source is π^0 Dalitz decay with a contribution of 21%. The

cut level	$\sharp$ leptons	[%]	$\sharp$ e^-	[%]	$\sharp$ e^+	[%]
cut 0	1300603	100	636419	100	664184	100
cut 1	1102827	85	574705	90	528122	80
cut 2	945765	73	516610	81	429155	65
cut 3	783233	60	459083	72	324150	49
cut 4	770630	59	450674	71	319956	48

Table 6.6: Analysis of the real data (November 2001), C+C at AGeV sample 35 325 966 evt with Mult.char.part > 0. The lepton multiplicities and reduction after each analysis step.

cut level	$\sharp$ lep	purity [%]	[%]	$\sharp$ e^-	purity [%]	[%]	$\sharp$ e^+	purity [%]	[%]
cut 0	741132	76	100	387245	82	100	353887	69	100
cut 1	671774	80	91	360896	84	93	310878	75	88
cut 2	558185	85	75	314700	87	81	243485	82	69
cut 3	488652	91	67	290610	93	76	198042	89	57
cut 4	483299	91	66	287464	93	75	195835	89	56

Table 6.7: The analysis of the simulated C+C events at 2 AGeV sample 16 973 392 evt with Mult.char.part > 0. The lepton multiplicities, purity and reduction after each analysis step.

contribution of the tracks that in simulation do not corresponds to common lepton track in all detectors- fake tracks is for electrons 7% and for positrons 11%.

On *Fig. 6.12* the momentum of the electron and positron candidates after *cut0* is plotted as a function of velocity of the particle. The distribution has maximum for low momenta and velocity about one. This corresponds to the observation that most of the candidates are leptons. Also the expected lines of pions and protons are shown. The proton contamination of the positrons is visible. It is easy to understand that velocity cut in *cut3* will remove the dominant part of it. In distributions for leptons in the TOFINO detector, an occurrence of the candidates with the velocity larger than one. This is related to the hits where there is more than one particle TOFINO hit and time of flight time was wrongly determined, systematically lower. This leads then to velocities larger than one for such tracks. These hits have not been removed from analysis but velocity cut for leptons in TOFINO has been open for velocities larger than 1 (in c units).

All distribution presented in these chapter are shown in *Appendix A* separately for TOF and TOFINO subsystem and also for each step of the lepton analysis.

In *Fig. 6.13* and *Fig. 6.14* the polar and azimuthal distribution of the leptons from the analysis of the measured (blue) and the simulated (red) data is shown. The mean values of the polar angle are larger in the simulation than in the real data (see *Tab. 6.9*), but the shape of the two distributions is similar. The mean polar angle θ = $51.8°$ of the reconstructed positron candidates is larger than that of $39.3°$ of electron candidates in the measured data. This is because of the opposite polarity of the particles. The HADES magnetic field has during an experiment such polarity that electrons have been bent out of the beam axis while positrons have been bent towards the beam axis. Most influenced

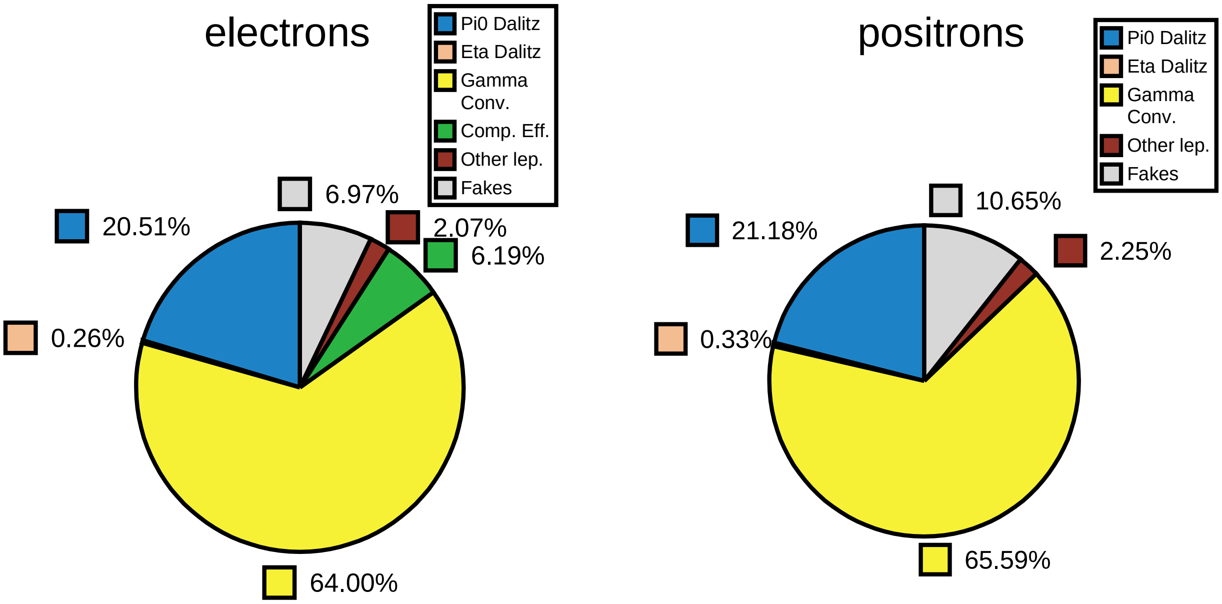

Figure 6.11: The sources of reconstructed leptons in simulated data.

by the magnetic field are particles with low momenta since they have the largest bending angles. Electrons with large polar angle θ before the magnetic field and low momenta are bent out of the acceptance in the field and do not hit TOF. This is possible to see on the momentum dependence of θ for leptons in *Fig. A.8*, where the electrons with momenta lower than 100 MeV/c and $\theta \in (70° - 85°)$ are not detected in TOF because they went out of the acceptance. The part of the electrons with $\theta \in (10° - 40°)$ and low momenta went to the TOF detector despite the fact that without a field they would fly to TOFINO. For a comparison, positrons with the same θ and momentum are bound out of the acceptance towards the beam axis. The positrons with $\theta \in (50° - 65°)$ and low momentum are due to the deflection flying to TOFINO instead to TOF. These effects lead to the fact that electrons are found with smaller polar angles than positrons.

The azimuthal angle ϕ distribution in *Fig. 6.14* shows the differences of the lepton yield in various sectors of HADES. The sector 0 that covers $\phi \in (60° - 120°)$ was equipped only with one inner MDC chamber and therefore position resolution of the tracks was also lower and the matching with the rings is not so good. The rest of the sectors should be identical. This is observed for simulated data (red line) but for the real data in sectors 1-4 covering $\phi \in (120° - 360°)$ the multiplicity is lower than expected. The difference between the measured and simulated data is larger for particles with hit in TOF than TOFINO, see *Fig. A.2*. This indicates the lower efficiency of TOF detector in measured than simulated data. In sector 2 ($\phi \in (60° - 120°)$) also one TOFINO paddle had lower efficiency, but otherwise measured data are well described by simulation.

The momentum spectra of the measured and the simulated data are displayed in *Fig. 6.15*. The simulated data overestimate the measured data, but the shape and slope of the spectra above the momentum of 100 $\mathrm{MeV/c^2}$ is similar. In *Fig. A.5* in *Appendix A* momentum spectra are shown after each lepton cut for measured data. The contamination from high momentum hadrons is significantly reduced after all cuts are applied, especially for the positrons that are contaminated by protons.

Another possible presentation of the data is with help of the rapidity and the transverse momenta variables. For the particle with four momentum $(E, p_x c, p_y c, p_z c)$ is the transverse momentum $p_T = \sqrt{p_x^2 + p_y^2}$ and rapidity $y = \frac{1}{2}\ln(\frac{E+p_z c}{E-p_z c})$ The mean rapidity for the reconstructed electrons is 1.11 while for positrons it is 0.77 (see *Tab. 6.9*). This difference is caused also by the difference of the acceptance of the leptons with different polarity for low momenta (see *Fig. 6.18*, *Fig. 6.19*, and *Fig. 6.20*).

The measured and simulated rapidity spectra in *Fig. 6.17* differ mainly for rapidities smaller than 1. This is the region of acceptance cover mostly by TOF detector.

The comparison of the transverse momentum spectra of simulated and measured data in *Fig. 6.16* shows an agreement of the shape. The simulated data overestimate the measured value for transverse momenta up to 700 $\mathrm{MeV/c^2}$.

The shapes of the spectra of simulated and measured data agree but the yields of the simulated data are larger. In *Tab. 6.8* the yields of the positrons and electrons are tabulated for measured and simulated data in TOF and TOFINO separately. The multiplicity of the leptons in the simulated data with the UrQMD event generator is 2.85.10^{-2} leptons per one event with at least one charged particle. This value is by 31% larger than that for the measured data. The difference is larger for the leptons detected in the TOF detector that is 38% than for the leptons detected in the TOFINO detector, 21%. These differences in the yield are discussed at the end of *Section 6.7* .

Summary

Single lepton tracks have been identified in measured and simulated data. The rapidity of reconstructed leptons spans from 0 to 2 units of rapidity. The purity of the lepton sample in simulations is after applying the lepton selection criteria about 90$\%$. The spectra of measured and simulated leptons agree well in shape, especially for the momentum spectrum. However the yields of the measured data are smaller than the yields of the simulated data by about 30$\%$. The difference varies for different sectors and systems. Appart from a possible overall deficiency of the UrQMD transport model, this indicates that the experimental lepton efficiency varies from sector to sector, and needs to be investigated further. Other possible reasons of the differences in the yield are discussed together with yields of dileptons at the end of *Section 6.7* .

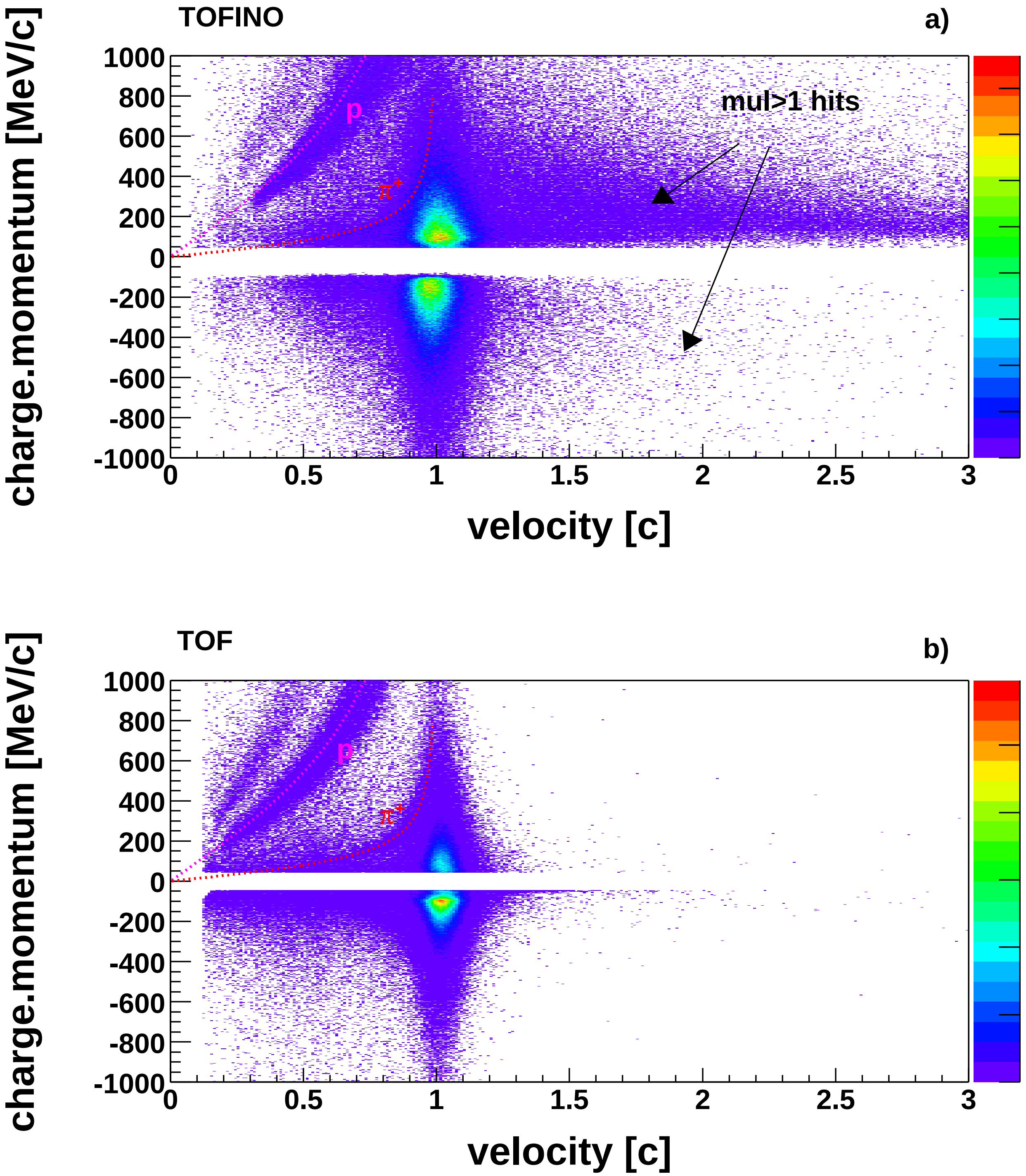

Figure 6.12: The momentum*charge versus velocity distribution of the lepton candidates after $cut0$ (tracks matched with RICH rings) of analysis for the measured data. For the positive charge particles the expected lines for protons and pions are also plotted. The hits above the proton line are probably deuterons. The leptons candidates are separated to those that have hit in TOFINO (a) and TOF (b). The hits with velocity larger than 1 are in TOFINO case are the multiple hits in TOFINO, for details see text.

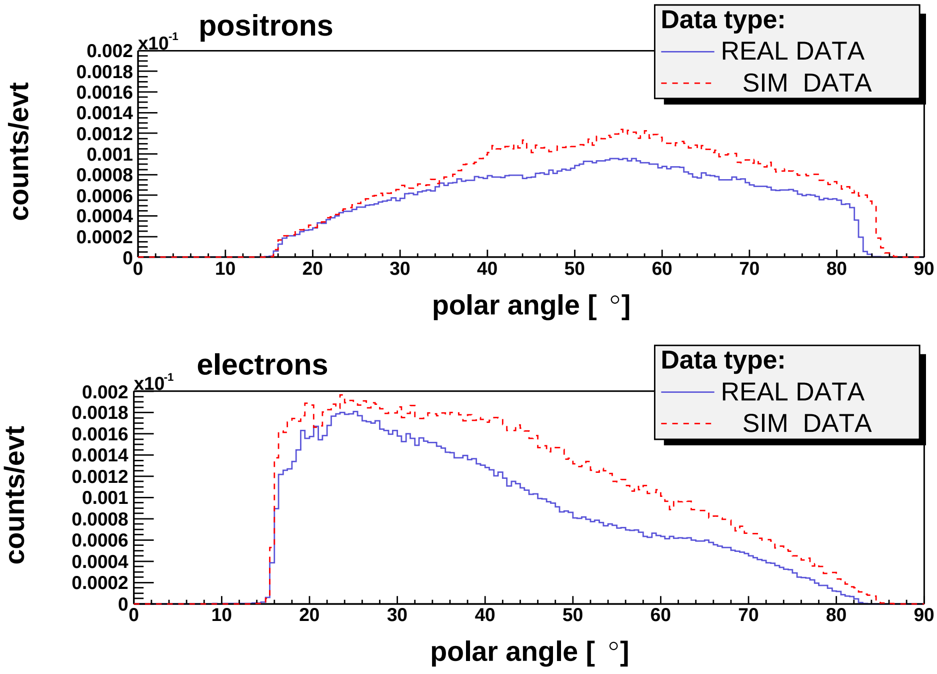

Figure 6.13: The polar angle distribution of e$^-$ and e$^+$ from analysis of measured and simulated data.

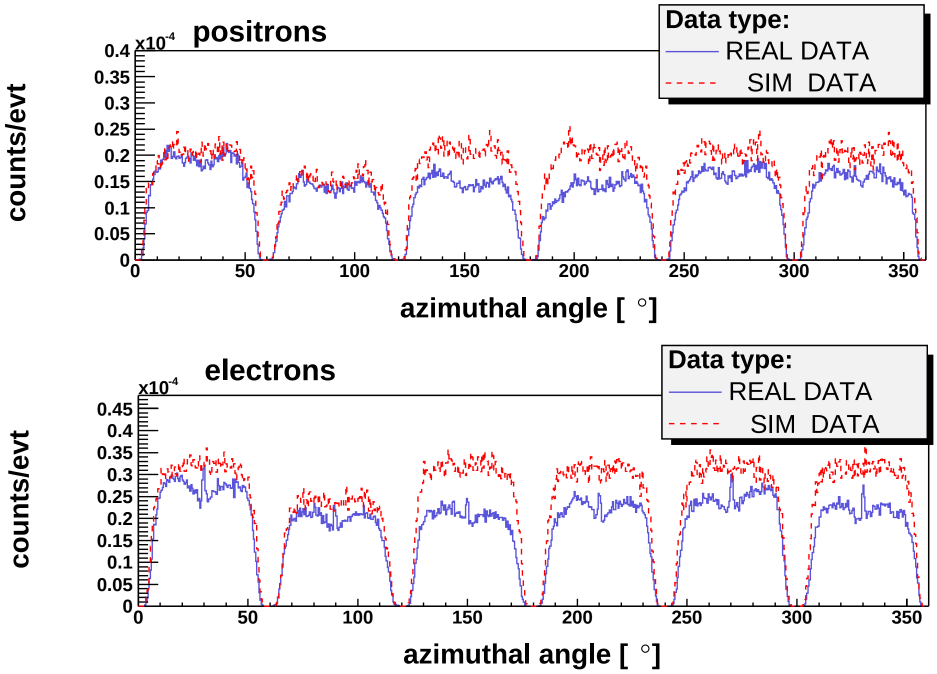

Figure 6.14: The azimuthal angle distribution of e$^-$ and e$^+$ from analysis of measured and simulated data.

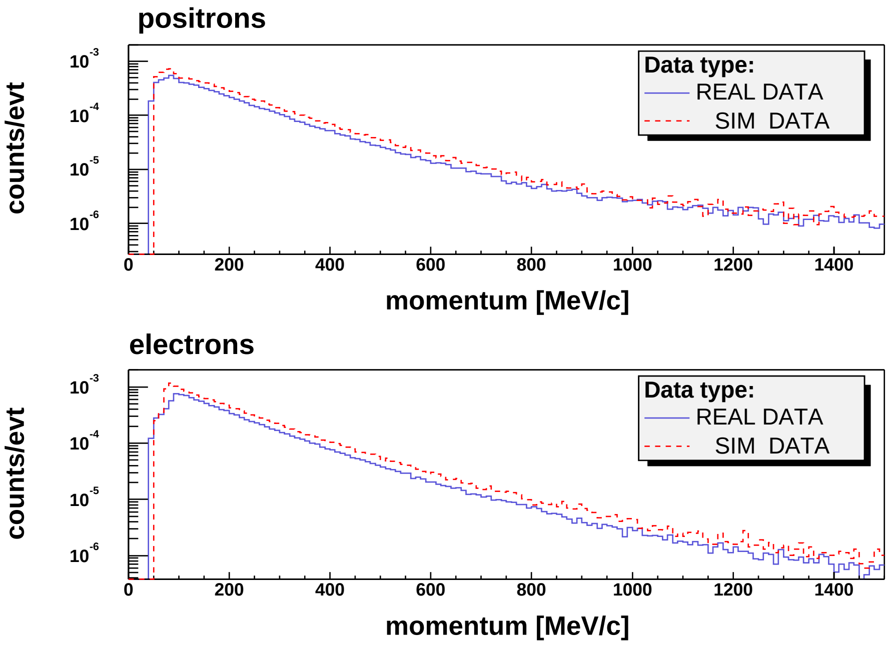

Figure 6.15: The momentum distribution of e^- and e^+ from analysis of measured (blue) and simulated data (red) after all lepton cuts.

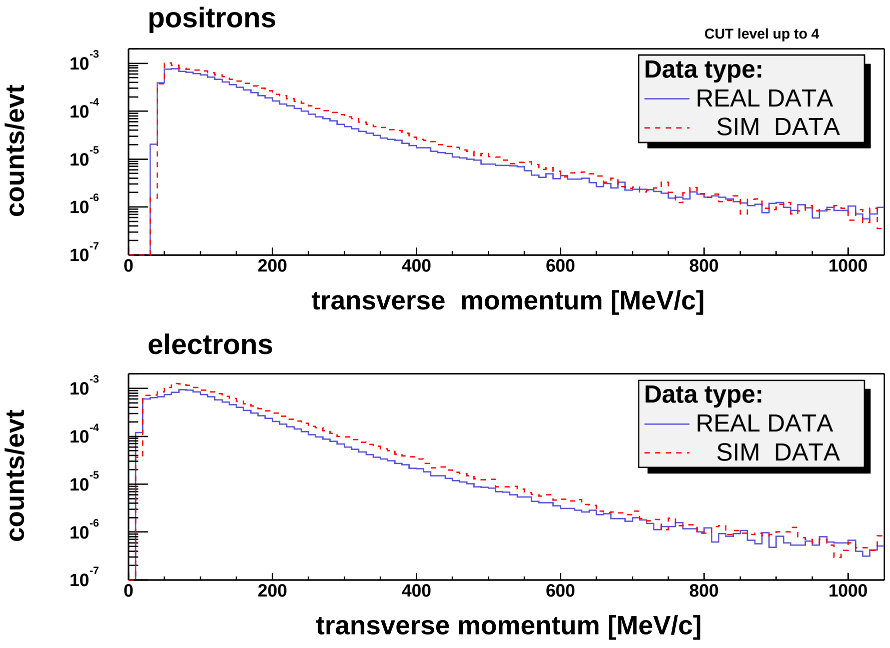

Figure 6.16: The total transverse momentum distribution of leptons from analysis of measured and simulated data. The lepton candidates pass all lepton cuts.

	REAL DATA			SIM DATA			SIM/REAL		
	All 10^{-3}	TOF 10^{-3}	TOFINO 10^{-3}	All 10^{-3}	TOF 10^{-3}	TOFINO 10^{-3}	All	TOF	TOFINO
e^-	12.7	8.4	4.3	17.0	11.8	5.2	1.34	1.40	1.20
e^+	9.1	4.3	4.8	11.5	5.7	5.8	1.26	1.34	1.21
SUM	21.8	12.7	9.1	28.5	17.5	11.0	1.31	1.38	1.21

Table 6.8: The multiplicity of e^- and e^+ per event with at least one charged particle from analysis of real and simulated data, also for TOF and PreSHOWER/TOFINO systems separately.The lepton candidates fulfilled all lepton analysis cuts.

	REAL DATA		SIM DATA	
	e^+	e^-	e^+	e^-
$< \theta >$	51.8	39.3	53.3	41.5
$< p >$	196.2	206.6	208.7	213.6
$< y >$	0.77	1.11	0.74	1.05
$< p_T >$	143.3	126.1	149.3	131.1

Table 6.9: The comparison of the mean values of polar angle θ, momentum p, rapidity y, and transverse momentum p_T for leptons in measured and simulated data.

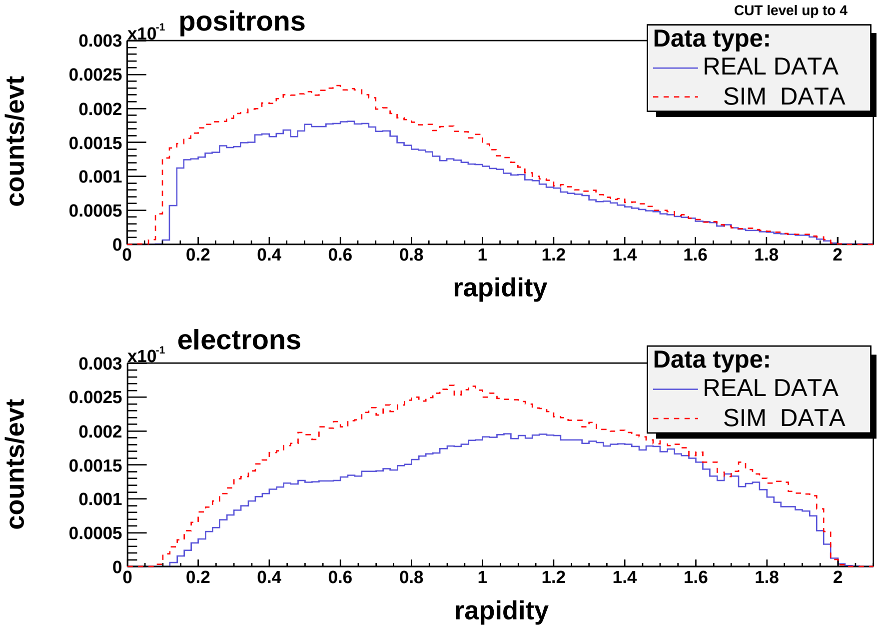

Figure 6.17: The total rapidity distribution of leptons from analysis of measured and simulated data. The lepton candidates pass all lepton cuts.

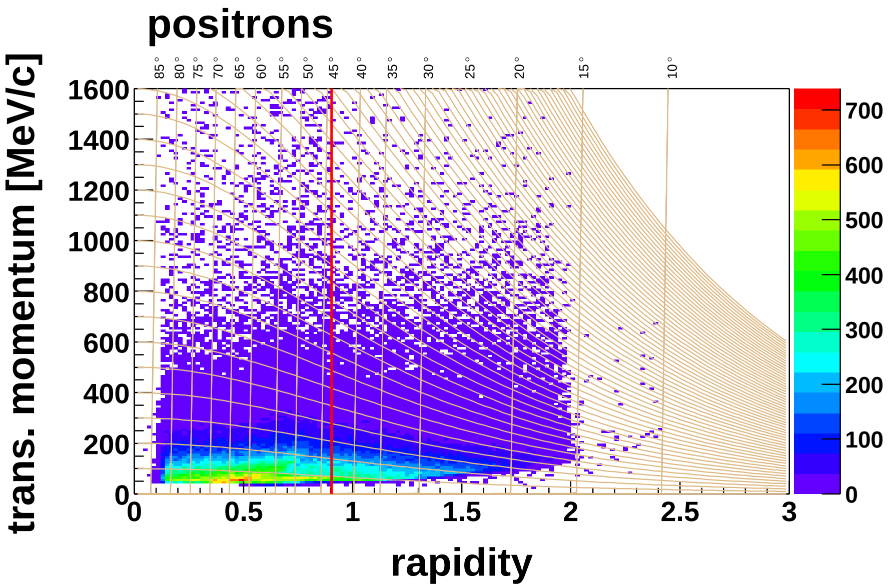

Figure 6.18: Transverse momentum versus rapidity spectrum for positrons from analysis of the measured data after all lepton cut.Red line indicates the midrapidity.

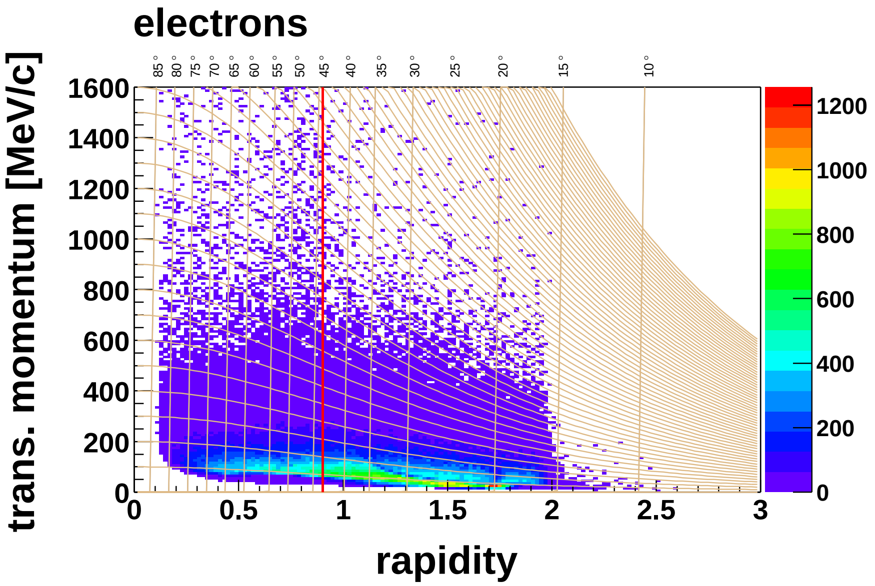

Figure 6.19: Transverse momentum versus rapidity spectrum for electrons from analysis of the measured data after all lepton cut.Red line indicates the midrapidity.

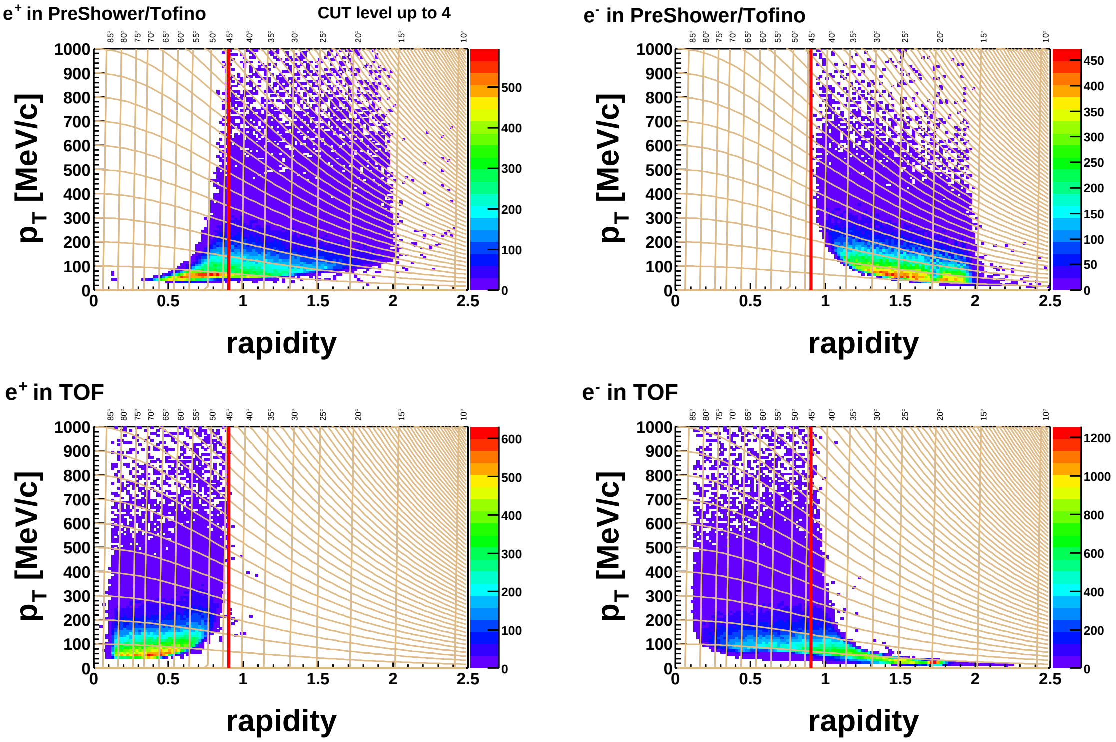

Figure 6.20: The transverse momentum versus rapidity distribution of e$^-$ and e$^+$ from analysis of measured data for TOF and PreSHOWER/TOFINO systems separately for candidates after all lepton analysis cuts.

6.7 Dilepton spectra

From the events that contain more than one lepton we have constructed the lepton pairs (dileptons) combining all leptons in one event. Unlike-sign pairs do not contain only correct combinations of leptons from a decay of one particle but also uncorrelated combinations of not corresponding leptons as it was described in *Chapter 5*. The yield of this combinatorial background can be constructed by several methods. We have chosen the like-sign pair method. The reconstructed combinatorial background should be subtracted from all reconstructed $\mathrm{e}^{+}\mathrm{e}^{-}$ pairs and the final spectrum then corresponds to the yield of the pairs from the physics signal. In the dilepton analysis several cuts have been applied to clean up pairs from fake combinations and suppress pairs from γ conversion . The cuts are listed in *Tab. 6.1* as cuts 5-9.

6.7.1 The rejection of the pairs with common hits

In an ideal case there would be only one $\mathrm{e}^{+}\mathrm{e}^{-}$ pair reconstructed for each existing pair. It is indeed possible that the hits in the detectors are used several times in tracking procedure and consequently more than one pair can be reconstructed for each pair.

The absence of MDC modules after the magnetic field makes matching of the hits before and after magnet less precise compared to a set-up with all MDC modules. It happens that one hit from the inner MDC modules is combined with several hits in the META detector, because they all fall into the matching window. If these META hits fulfill the lepton selection criteria, there will be more than one MDC-META track piece reconstructed for one lepton track. If the MDC hit of the MDC-META track piece is matched with a RICH ring, then more than one corresponding lepton is reconstructed. Combining all the leptons in the event, some of the pairs are combinations of leptons with a common hit in one of the detectors. The combinations with a common hit can not correspond to true pairs from the decay of particles, except the case of pairs with small opening angle and unresolved in RICH and/or MDC, but resolved in magnetic field, because of the different bending of positive and negative particles.

In *Fig. 6.21* and *Fig. 6.22* different topologies of pairs with a common hit in one of the detectors for unlike-sign and like-sign pairs is shown. Most frequent case for measured or simulated data is for $\mathrm{e}^{+}\mathrm{e}^{-}$ pairs the RM case (common RICH and MDC hits) and R case (common RICH hit). These cases are 70% (RM case) and 20% (R case) of all $\mathrm{e}^{+}\mathrm{e}^{-}$ pairs. The most of the R and RM cases are unresolved conversion and Dalitz pairs. The average multiplicities of the different cases are shown in *Fig. 6.23* for measured or simulated $\mathrm{e}^{+}\mathrm{e}^{-}$, $\mathrm{e}^{-}\mathrm{e}^{-}$ or $\mathrm{e}^{+}\mathrm{e}^{+}$ pairs. For the like-sign pairs the most frequent cases are RMe (common RICH and META hits), RM and R case. The RMe case is consequence of the bad matching of the 2 MDC hits to the same META hit after magnetic field, due to the low granularity of META detector. These cases will be suppressed in full set-up with all MDC.

For both like-sign and unlike-sign pairs, the pairs with leptons that do not have in common any of the hits are $6 - 13\%$ of all pairs.

For further analysis only the pairs with different hits in both leptons have been selected in *cut6*. The rejection of the RM and R cases for unlike-sign pairs is effectively also rejection of close pairs unresolved (in 75% conversion pairs) in RICH and/or MDC, because part of these unresolved cases have this topology. More than 50% of the pairs that pass this cut are π^0 Dalitz pairs. This selection reduces the content of fake pairs in the sample. S/B ratio between the reconstructed signal and the background increases from 0.174 to 1.017 after this cut (see *Tab. 6.11*).

In the measured data less pairs is reconstructed with no common hits in leptons (9.21%) than in simulated data (12.86%), see *Tab. 6.10*. Therefore the number of the reconstructed pairs per event in the measured data is smaller after applying of this cut than in simulated data. The ratio between the number of the $\mathrm{e^+e^-}$ pairs in simulated and measured data per event becomes 2.1, see *Tab. 6.14*. More resolved pairs in simulated data can be explained by a better two track resolution in the simulated data in RICH and MDC detectors, respectively

Common hits	$\mathrm{e^+e^-}$			$\mathrm{e^-e^-}$			$\mathrm{e^+e^+}$		
	REAL [%]	SIM [%]	S/R	REAL [%]	SIM [%]	S/R	REAL [%]	SIM [%]	S/R
0	9.21	12.86	2.07	5.95	7.91	1.70	6.44	8.45	1.75
R	20.56	18.90	1.36	6.32	7.33	1.49	8.38	8.04	1.27
M	0.06	0.04	0.96	0.03	0.02	0.70	0.04	0.01	0.45
RM	69.65	67.77	1.44	32.57	39.25	1.54	40.01	45.14	1.50
Me	0.42	0.35	1.25	3.82	3.82	1.28	2.52	2.63	1.39
RMe	0.11	0.07	1.02	50.81	41.28	1.04	42.35	35.51	1.11
MMe	0.00	0.00	0.00	0.52	0.41	1.03	0.27	0.22	1.07

Table 6.10: The occurrence of the different common hit pairs topologies (see *Fig. 6.21* and *Fig. 6.22*) for $\mathrm{e^+e^-}$, $\mathrm{e^-e^-}$, $\mathrm{e^+e^+}$ pairs in measured and simulated data as shown in *Fig. 6.23*. The first column list various possibilities 0: no common hit, R: common RICH hit, M: common MDC hit, RM: common RICH and MDC hit, Me: common META hit, RMe: common RICH and META,MMe: common MDC and META hit. The second and third column give the percentage of the specific type of pairs in all pairs for measured, respectively simulated data.The fourth column give the ratio of the reconstructed pairs of the specific type per event of simulated and measured pairs. The other columns give this values for $\mathrm{e^-e^-}$ and $\mathrm{e^+e^+}$ pairs.

6.7.2 The rejection of the pairs with double tracks

As it was described in *Chapter 4* some of the hits in the MDC correspond to an unresolved close pair. Such hits can be identified based on the MDC hit cluster size and the number of contributing wires to the cluster described in *Chapter 4*. From all pairs only such pairs are selected in which both leptons contain only single MDC hits. A pair has been

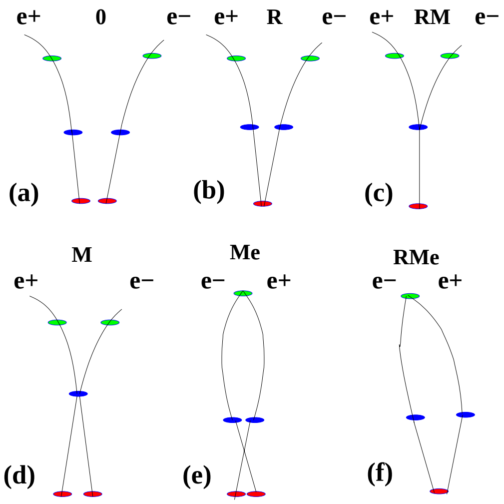

Figure 6.21: Schematic picture of different topology of the e^+e^- pairs. The leptons in the pairs can have one or two common hit in RICH (red), MDC (blue) or META (green) detectors. (a) two separated tracks, (b) common RICH hit, (c) common RICH and MDC hits, (d) common MDC hit, (e) common META hit (f) common RICH and META hits.

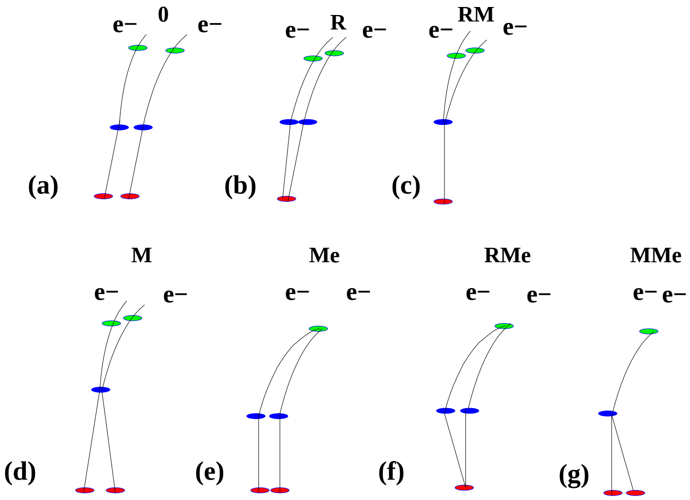

Figure 6.22: Schematic picture of different topology of the e^-e^- (e^+e^+) pairs. The leptons in the pairs can have one or two common hit in RICH (red), MDC (blue) or META (green) detectors. (a)two separated tracks, (b) common RICH hit, (c) common RICH and MDC hits, (d) common MDC hit, (e) common META hit (f) common RICH and META hits (g) common MDC and META hits.

selected for further analysis if the probability of the hit in module 0 or module 1 of MDC was larger than 0.9 for both leptons in the pair. Otherwise the pair was rejected. This selection could be performed also as the last part of the lepton analysis, but it is easier

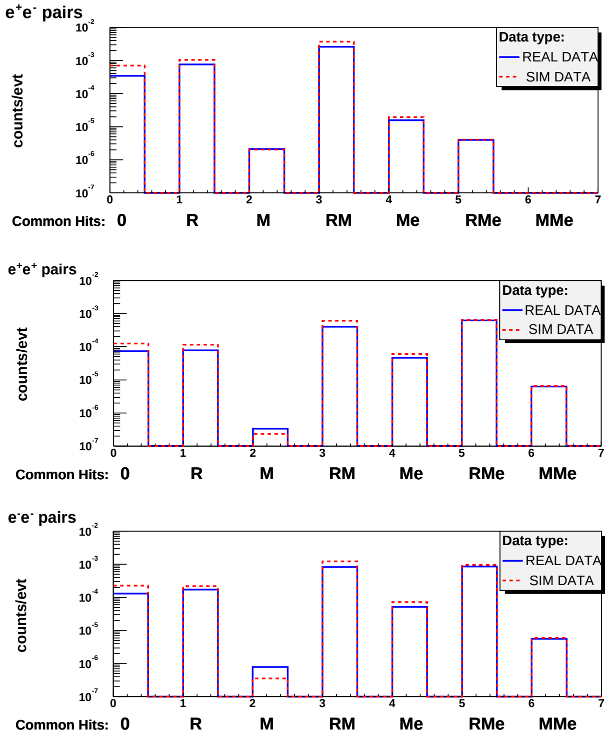

Figure 6.23: Comparison of the multiplicity of the pair topologies in measured (blue line) and simulated (red line) data for e^+e^- , e^+e^+ and e^-e^- pairs. For definition of the various topologies, see *Fig. 6.21* and *Fig. 6.22*

to demonstrate the reduction of the combinatorial background after this rejection for the pairs if it is applied here. After applying this selection, S/B ratio for the invariant masses of the e^+e^- spectrum increases from 1.017 to 2.078 because combinatorial background is suppressed, see *Tab. 6.14*. After this cut the ratio of simulated and measured data increase, while in measured data the number of pairs with one lepton with double hit is larger than in simulated data. This is the observation consistent with those in previous paragraph.

6.7.3 The rejection of the pairs with small opening angle

The dilepton pairs from π^0 induced γ conversion have on average smaller opening angles than π^0 Dalitz decays and other Dalitz decays. Therefore, an additional cut has been applied to suppress the conversion signal in the final spectrum: a small opening angle cut. The dileptons with opening angle smaller than $\alpha < 4°$ have been rejected. Obviously also the π^0 Dalitz pairs with small opening angles will be rejected by this cut, but in the surviving sample remain mostly the pairs from Dalitz decays and therefore the signal to background ratio is improved. After removing the pairs with small opening angle also all other combinations of the leptons from this pair with other leptons were removed, even if such combinations had large opening angle. This is done because if a pair with the small opening angle is from γ conversion then the combinations of leptons from this pair with other leptons in the event are necessarily fake combinations. The matching of the inner MDC hits and the META hits in the kickplane algorithm produces correlated like-sign pairs with small opening angles when to a true $\mathrm{e}^+\mathrm{e}^-$ pair also a combination with a false META hit is matched; such a pair looks like a like-sign pair. This happens up to $8^\circ - 10^\circ$ (see *Fig. 5.2* in *Chapter 5*) and therefore to remove all such correlated like-sign pairs, an opening angle cut of 8° has been applied. For sake of comparison both opening angle cuts are treated separately. In *Fig. 6.24* the opening angle distribution of the pairs before any opening angle cut is shown. The simulated distribution shows a bit sharper peak but application of this cut does not change the ratio between the simulated and measured $\mathrm{e}^+\mathrm{e}^-$ pairs. However S/B ratio is improved after this cut, see *Tab. 6.14*..

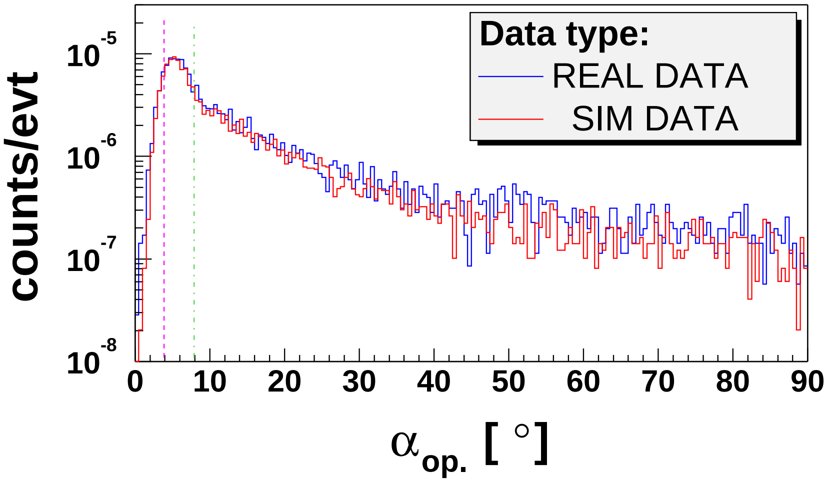

Figure 6.24: The opening angle spectrum of the all $\mathrm{e}^+\mathrm{e}^-$ pairs from the analysis of measured (blue line) and simulated (red line) data of C+C at 2 AGeV. The spectra are normalized to the same π^0 Dalitz pairs yield of the $\mathrm{e}^+\mathrm{e}^-$ signal after combinatorial background subtraction.The dilepton cuts 5-7, without opening angle cut have been applied. The dashed and dot-dashed lines show the 4° and 8° cuts.

6.7.4 The reduction of the true physical pairs

In the GEANT simulations it is possible to identify which reconstructed pair corresponds to a true pair from the decay of some particle: both leptons should have as parent the same particle. This allows to estimate the efficiency of reduction of the background pairs and signal sources after each analysis step. From the analysis of the simulated data it is possible to conclude (see *Tab. 6.13*), that from all π^0 Dalitz pairs that are in geometrical acceptance of HADES and both leptons have been reconstructed 17% survived all the dilepton cuts, from the η Dalitz pairs with invariant mass 160-600 MeV/c^2 21% survived, and from γ conversion , only less than 1% survived. It is also possible to determine the acceptance and reconstruction efficiency of the π^0 Dalitz pairs in simulation. From all produced π^0 Dalitz pairs in simulation 5% have been reconstructed in $cut5$ of the dilepton analysis and from these 17% passed all dilepton cuts, giving 0.9% from all produced π^0 Dalitz pairs.

6.7.5 The invariant mass spectra

In the sample of the measured data from the November 2001 run an amount of 3381±58 $\mathrm{e}^+\mathrm{e}^-$ pairs has been reconstructed after applying all dilepton criteria. The given errors in this paragraph are purely statistical. From like-sign pairs a combinatorial background has been constructed as it was described in *Chapter 5*. The combinatorial spectrum has been subtracted bin-wise from the invariant mass spectrum of $\mathrm{e}^+\mathrm{e}^-$ pairs and the resulting spectrum is the measured signal of true $\mathrm{e}^+\mathrm{e}^-$ pairs from physical particle decays. The yield of $\mathrm{e}^+\mathrm{e}^-$ pairs after subtraction was 2165±68 pairs. Most of the pairs from reconstructed signal have invariant mass up to 160 $\mathrm{MeV/c^2}$, it is 2092±61 pairs. There are 72±29 pairs in the region from 160-600 $\mathrm{MeV/c^2}$, relevant for η-Dalitz. The values for each cut of analysis are listed in *Tab. 6.11* for measured data. The reconstructed $\mathrm{e}^+\mathrm{e}^-$ pairs for simulated data are listed in *Tab. 6.12*.

cut level	$N_{e^+e^-}$	$N^{sig}_{e^+e^-}$	$N^{sig}_{e^+e^-}$	$\frac{N^{sig}_{e^+e^-}}{N_{cb}}$	$N^{sig}_{e^+e^-}$	$\frac{N^{sig}_{e^+e^-}}{N_{cb}}$
	0-1000 $[MeV/c^2]$	0-1000 $[MeV/c^2]$	0-160 $[MeV/c^2]$	0-160 $[MeV/c^2]$	160-600 $[MeV/c^2]$	160-600 $[MeV/c^2]$
5	130257	19157	18949	0.174	208	0.106
6	11928	5133	4939	1.017	194	0.100
7	6658	4147	4058	2.078	89	0.160
8	5094	3465	3393	2.804	71	0.171
9	3381	2165	2092	2.590	72	0.178

Table 6.11: The analysis of the measured data for C+C at 2 AGeV with 35 325 966 evt with Mult.char.part > 0. Following quantities are tabulated as a function of the applied dilepton cuts 5-9: the number of e^+e^- pairs $N_{e^+e^-}$ that passed the cut,the reconstructed e^+e^- signal after subtraction of the combinatorial background $N^{sig}_{e^+e^-}$, both is tabulated for all pairs with invariant mass up to 1000 MeV/c^2 and then for the ranges: (0-160) MeV/c^2 (dominated by π^0 Dalitz decay), 160-600 $\mathrm{MeV/c^2}$ (dominated by η Dalitz decay). For both last ranges also ratio between reconstructed signal and combinatorial background $\frac{N^{sig}_{e^+e^-}}{N_{cb}}$ is given. The cut 5 means that no dilepton cut is performed;cut 6 means that all pairs that contain a common hit are removed; cut 7 means that all the pairs that contain one double track are removed; cut 8 means that all pairs that have opening angle less than 4° are removed and cut 9 means that all pairs that have opening angle less than 8° are removed. Applying a particular cut means that all previous cuts were already applied.

In the analysis of the measured data there were (0.96 ±0.02)$\cdot 10^{-4}$ $\mathrm{e}^+\mathrm{e}^-$ pairs per event with at least one charged particle and after subtraction of the combinatorial background there have been found (0.61±0.01)$\cdot 10^{-4}$ $\mathrm{e}^+\mathrm{e}^-$ pairs per event. In the analysis of

cut level	$N_{e^+e^-}$	$N^{sig}_{e^+e^-}$	$N^{sig}_{e^+e^-}$	$\frac{N^{sig}_{e^+e^-}}{N_{cb}}$	$N^{sig}_{e^+e^-}$	$\frac{N^{sig}_{e^+e^-}}{N_{cb}}$
	0-1000 $[MeV/c^2]$	0-1000 $[MeV/c^2]$	0-160 $[MeV/c^2]$	0-160 $[MeV/c^2]$	160-600 $[MeV/c^2]$	160-600 $[MeV/c^2]$
5	92575	23066	22947	0.339	119	0.069
6	11867	6254	6125	1.574	128	0.075
7	8291	5779	5690	3.006	88	0.143
8	6316	4888	4792	4.581	95	0.251
9	3976	2931	2839	4.179	91	0.250

Table 6.12: The analysis of simulated data for C+C at $2A$GeV with 16 973 392 evt with Mult.char.part > 0. The tabulated variables are identical to *Tab. 6.11* for real data.

the simulated data it was factor 2.5 (2.8 for signal) more reconstructed $\mathrm{e^+e^-}$ pairs per event. In *Tab. 6.14* the multiplicity of reconstructed $\mathrm{e^+e^-}$ pairs before and after combinatorial background subtraction is listed for each analysis step. In the lepton analysis it was found that in simulated data factor 1.34 more electrons and factor 1.26 positrons have been found. It is therefore expected that after combining of the leptons to unlike-sign pairs, factor 1.26x1.34=1.69 more $\mathrm{e^+e^-}$ pairs in simulated data than in real one in a case of uncorrelated pairs and 1.26 in a case of correlated pairs. The difference between measured and simulated data after combining the leptons to dileptons in $cut5$ is 1.5. This difference increases after applying the additional cuts up to a factor 2.8 in the reconstructed yield. The increase of the difference between simulation and data in $cut6$ and $cut7$ can be understood as different performance of the close tracks tracking in the simulated and measured data. The difference of yield after subtraction of the combinatorial background is not the same as difference of reconstructed pairs, while the ratio of the reconstructed like-sign pairs between simulated and measured data is smaller than for unlike-sign, see *Tab. 6.15*, therefore also difference of the reconstructed combinatorial background is smaller and consecutive the difference in the yield of the signal is larger than difference of the unlike-sign pairs.

The invariant mass spectrum of all the $\mathrm{e^+e^-}$ pairs, combinatorial background and $\mathrm{e^+e^-}$ signal is shown in *Fig. 6.25*. The part of the spectrum up to 100 $\mathrm{MeV/c^2}$ shows high S/B ratio. In the rest of the spectrum the reconstructed combinatorial background is larger than the yield of the signal. In *Fig. 6.28* the invariant mass spectrum of the signal after each step of analysis is shown. The shape of the spectrum above 40 $\mathrm{MeV/c^2}$ does not change during the analysis.

The spectrum of reconstructed yield is dominating in the region from 0-160 $\mathrm{MeV/c^2}$ that corresponds to expected signal from π^0 Dalitz decay. In the region from 160-600 $\mathrm{MeV/c^2}$ the most dominating source is η Dalitz decay. The spectrum in 0-160 $\mathrm{MeV/c^2}$ is reconstructed with a large S/B ratio of 2.59.

In *Fig. 6.26* the comparison of the reconstructed yield in measured and simulated data is shown. The spectra differ up to 160 $\mathrm{MeV/c^2}$ of invariant mass but above the

	0-160 MeV/c^2							160-600 MeV/c^2		
cut level	$N^{sig}_{e^+e^-}$	$\frac{N_{\pi^0 Dal}}{N^{sig}_{e^+e^-}}$	[%]	$\frac{N_{\eta Dal}}{N^{sig}_{e^+e^-}}$	[%]	$\frac{N_{\gamma conv}}{N^{sig}_{e^+e^-}}$	[%]	$N^{sig}_{e^+e^-}$	$\frac{N_{\eta Dal}}{N^{sig}_{e^+e^-}}$	[%]
5	22947	0.64	100	0.01	100	2.56	100	119	0.27	100
6	6125	0.86	36	0.01	34	0.18	2	128	0.25	100
7	5690	0.85	33	0.01	32	0.17	2	88	0.32	88
8	4792	0.85	28	0.01	28	0.11	1	95	0.26	78
9	2839	0.89	17	0.02	21	0.02	0	91	0.27	78

Table 6.13: The analysis of simulated data November 2001 C+C at 2 AGeV sample 16 973 392 evt with Mult.char.part > 0. In the second column the reconstructed yield of $\mathrm{e^+e^-}$ signal is tabulated after the applying the cut in the first column. In the third column the ratio of the true π^0 Dalitz pairs to reconstructed signal is given for invariant masses of the pairs up to 160 $\mathrm{MeV/c^2}$. In the fourth column the part of the true π^0 Dalitz pairs that survive the cuts is given (100% is the value after cut 5) . The column 5, 6 gives the same for the pairs from η Dalitz pairs and columns 7, 8 for γ conversion pairs. In the columns 9, 10, 11 is the same information about pairs from η Dalitz decay for invariant masses 160-600 $\mathrm{MeV/c^2}$.

160 $\mathrm{MeV/c^2}$ within the errors bars no difference is observed. In the *Fig. 6.27* the simulated and measured spectra are normalized to the same integral for comparison of the shapes. Within the errors the shapes of the spectra do not differ, although the tendency of larger yield in measured data in region above 160 $\mathrm{MeV/c^2}$ can not be excluded.

From simulated data (*Tab. 6.13*) it is concluded that 89% of the reconstructed yield of the signal up to 160 $\mathrm{MeV/c^2}$ corresponds to the yield of the π^0 Dalitz pairs, 2% correspond to η Dalitz and 2% to γ conversion pairs. The remaining 7% are fake pairs. The $\mathrm{e^+e^-}$ pairs from π^0 Dalitz ,η Dalitz and γ conversion are shown as lines in *Fig. 6.27*. The reconstructed signal describes the yield from simulated sources in π^0 Dalitz region.

In the region of 160-600 $\mathrm{MeV/c^2}$ the spectrum from simulations should describe the η Dalitz yield, but it overestimates the yield of the true η Dalitz pairs by a factor of 3.7. This means that the combinatorial background in this region was not subtracted correctly and the reconstructed signal overestimates the true yield.

The opening angle distribution of the reconstructed $\mathrm{e^+e^-}$ pairs of simulated and measured pairs in *Fig. 6.30* after all dilepton cuts is very similar. This means that pair topology after the dilepton analysis is in the simulated data close to the real data. In *Fig. 6.29* opening angle distribution of $\mathrm{e^+e^-}$ pairs after each step of the analysis is shown.

It can be concluded that the reconstructed $\mathrm{e^+e^-}$ yield from measured data is dominated by $\mathrm{e^+e^-}$ pairs from π^0 Dalitz decay with high S/B ratio. However, a difference of the reconstructed yield in simulation and data by a factor 2.8 is observed.

The difference of the yield of the simulated and measured data can be related to the following reasons. The first reason is the difference in production multiplicity of the dilepton sources in the UrQMD and in the measured data. The most important aspect for this analysis is the ability of the UrQMD model to describe π production for C+C at 2 AGeV. The comparison with other experimental data summarized in *Chapter 3* , shows that there are discrepancies up to 50%.

Another reason is the stability of the detector performance in various sectors. From *Fig. 6.14* it is possible to deduce that the lepton multiplicity in various sectors differs to each other, and therefore also the agreement with simulated data differs for various sectors. Sectors 0 ($\phi \in (60^\circ - 120^\circ)$) and 5 ($\phi \in (0^\circ - 60^\circ)$) show a very good agreement between measured and simulated data.

The increase of the difference between simulated and measured data in $cut6$ and $cut7$ indicate the different efficiency in reconstruction of the close tracks. In simulated data less unresolved pairs in RICH and MDC have been found. This can be related also to misalignment of the detectors for measured data. The simulated data has been generated with an ideal geometry.

Next, there could be a problem with the simulation of the LVL1 trigger of HADES. UrQMD contains no coalescence and the nucleus is treated as a set of individual nucleons. Light fragments are not produced during the collision. There are no fragments produced during collision. This leads to different particle multiplicities in the HADES acceptance that could influence the trigger decision and therefore also the centrality of the triggered events.

The hadron analysis of the November 2001 data [51] shows that the difference of the reconstructed yield of the charged π in simulation and data is only about 5%. This means that UrQMD describes the π yields rather well. One can speculate that the observed difference of the dilepton yield can be accounted to higher lepton reconstruction efficiency of RICH in simulation than in data. However this is not compatible with agreement of the single lepton yield up to 30%. The difference of the factor 2.8 is specific to dilepton analysis. The reconstructed pairs are dominantly from π^0 Dalitz decays and the inefficiency can be mass dependent. The observed inefficiency of reconstruction is probably related to reconstruction of the tracks with small opening angle.

The discrepancy between the efficiencies in simulated and measured data has to be further investigated. The measurement of elementary reactions with proton beams brings further possibility to determine the efficiencies of the HADES detectors. The analysis of high-resolution data (from November 2002 beamtime) will also shed new light on this problematic.

It is not possible to compare directly the reconstructed yield of dileptons from November 2001 data to the C+C data measured by DLS [14]. First of all DLS measured C+C collisions at beam energy of 1 AGeV and HADES at 2 AGeV. The simulation presented in *Chapter 3* (see *Fig. 3.10* and *Fig. 3.11*) shows the difference of the dilepton spectra for both energies. Another reason preventing the direct comparison is the different acceptance of the detectors. Both spectra would have to be corrected for it. However, the following observation can be done. It was discussed in *Chapter 1* that DLS data can not be described by any known model. In [19] the calculation of the DLS dilepton spectrum for C+C at 1 AGeV within the UrQMD model has been presented. Additional artificial enhancement of the η yield by factor 10 led to description of the DLS data. Such an enhancement of the η production, however, leads to a contradiction with TAPS measurements [20], violates m_T scaling and is excluded by η photon production as it is shown in [17]. In case of HADES data, an enhancement of the η yield by a factor 10 with respect to UrQMD would be very well visible in the mass range from 160-600 $\mathrm{MeV/c^2}$. In this region the dilepton spectrum of C+C at 2 AGeV is dominated by η Dalitz decays. The enhancement of the η yield by a factor of 10 would lead to an enhancement of the reconstructed yield of the dileptons as shown in *Fig.* 6.26 and in *Fig.* 6.27, particularly in the 3 bins covering masses from 160-600 $\mathrm{MeV/c^2}$ by this factor. Let us now suppose that the observe inefficiency to reconstruct the π^0 Dalitz pairs in measured data is invariant mass independent and the spectra can be normalized to the same π^0 Dalitz yield as in *Fig.* 6.27. Then it is possible compare the η Dalitz yield (it means also η yield) in measured and simulated data in region 160-600 $\mathrm{MeV/c^2}$. After such assumed 'η enhancement' the tendency that the simulation underestimates the data in *Fig.* 6.27 by factor about 2-3 would be turned to an overestimation by a factor about 4-6. The agreement of the measured and simulated data would get worse.

Similar consideration can be done fro the unnormalized yields in *Fig.* 6.26. Now one would assume that the observed ineficiency of the π^0 Dalitz pairs is not present for η Dalitz pairs in the region 160-600 $\mathrm{MeV/c^2}$. Consequently, the difference between simulation and data would increase by a factor 10.

It seems that the HADES data from the analysis of the November 2001 beamtime do not support an enhancement of the η yield by factor 10, as it is necessary to describe the DLS data. However due to limited statistics, a somewhat smaller enhancement about 3-5 of the dileptons in region 160-600 $\mathrm{MeV/c^2}$ over UrQMD simulation would be compatible with the data.

cut level	REAL DATA				SIM DATA				SIM/REAL	
	$N_{e^+e^-}$ $[10^{-4}]$	[%]	$N^{sig}_{e^+e^-}$ $[10^{-4}]$	[%]	$N_{e^+e^-}$ $[10^{-4}]$	[%]	$N^{sig}_{e^+e^-}$ $[10^{-4}]$	[%]	$N_{e^+e^-}$	$N^{sig.}_{\pi^0 Dal.}$
5	36.9	100.0	5.4	100	54.9	100.0	13.7	100	1.5	2.5
6	3.4	9.2	1.4	31	7.1	13.0	3.7	29	2.1	2.6
7	1.9	5.1	1.2	26	4.9	8.7	3.4	28	2.6	2.9
8	1.4	3.9	1.0	22	3.8	6.8	2.9	24	2.6	3.0
9	1.0	2.6	0.6	14	2.4	4.3	1.7	14	2.5	2.8

Table 6.14: The multiplicity of the reconstructed $\mathrm{e^+e^-}$ pairs, $\mathrm{e^+e^-}$ signal per event with at least one charge particle for measured and simulated data for November 2001 and the ratio between them.

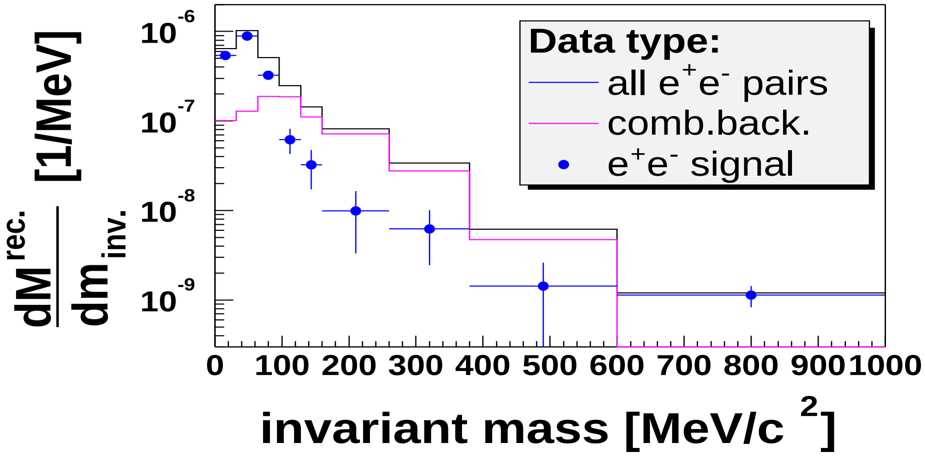

Figure 6.25: The reconstructed invariant mass spectrum of the e^+e^- pairs from the full analysis of the measured data of C+C at $2A$GeV. A sample of 35 325 966 events with mult. of charged particles > 0 have been analyzed. All e^+e^- pairs are shown in black, the reconstructed combinatorial background from like-sign method is shown as pink and subtracted spectrum is red line. The error in y direction is statistical error and the line in x direction shows the bin size. The binsize is $32MeV/c^2$ for first 5 bins, 100 MeV/c^2, 120 MeV/c^2, 220 MeV/c^2 and 400 MeV/c^2 in next bins. The spectra are normalized to total number of analyzed events and divided with binsize.

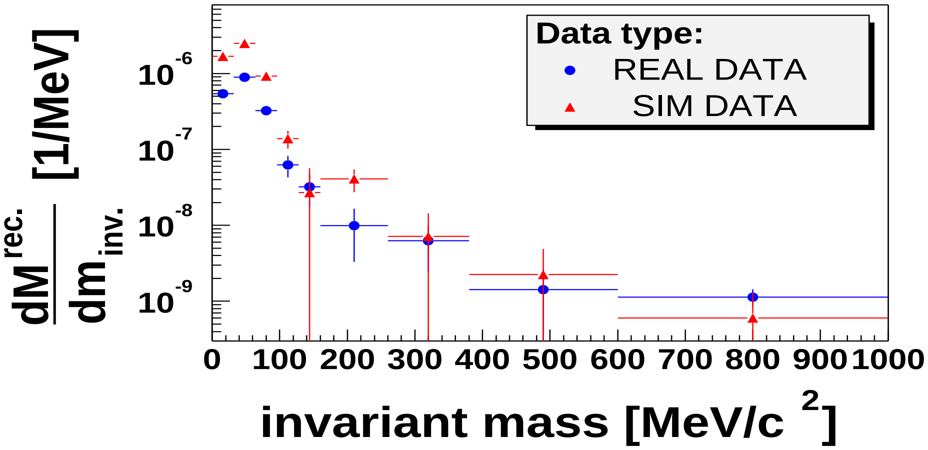

Figure 6.26: The reconstructed invariant mass spectrum of the e^+e^- signal from analysis of the measured (blue circles) and simulated (red triangles) data of C+C at 2 AGeV. The spectra are normalized to the number of the events with at least one charged particle.The binning is the same as in *Fig.* 6.25. The error in y direction is a statistical error and the line in x direction shows the bin size.

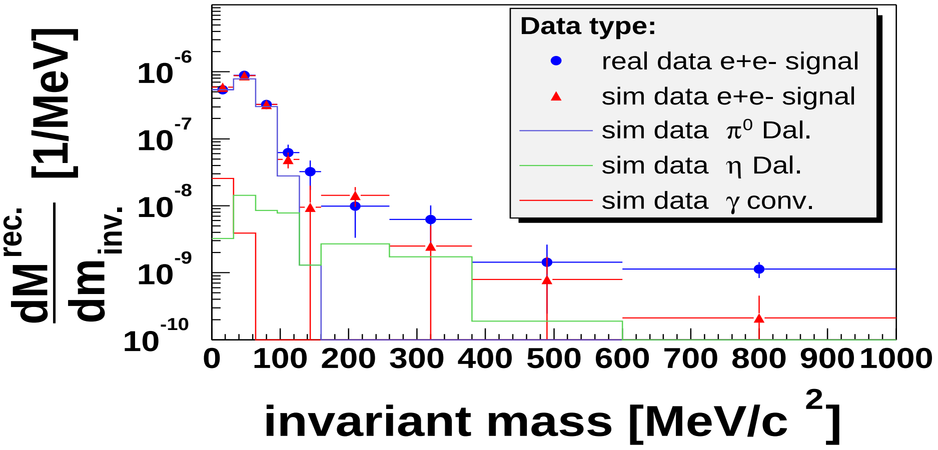

Figure 6.27: The invariant mass spectrum of the e^+e^- signal from analysis of the measured (blue circles) and simulated (red triangles) data of C+C at 2 AGeV. The spectra are normalized to the same π^0 Dalitz pairs yield and with the binning as in *Fig.* 6.25. The spectra corresponding to the true π^0 Dalitz (blue), η Dalitz (green) and γ conversion pairs in simulated data are shown.The error in y direction is a statistical error and the line in x direction shows the bin size.

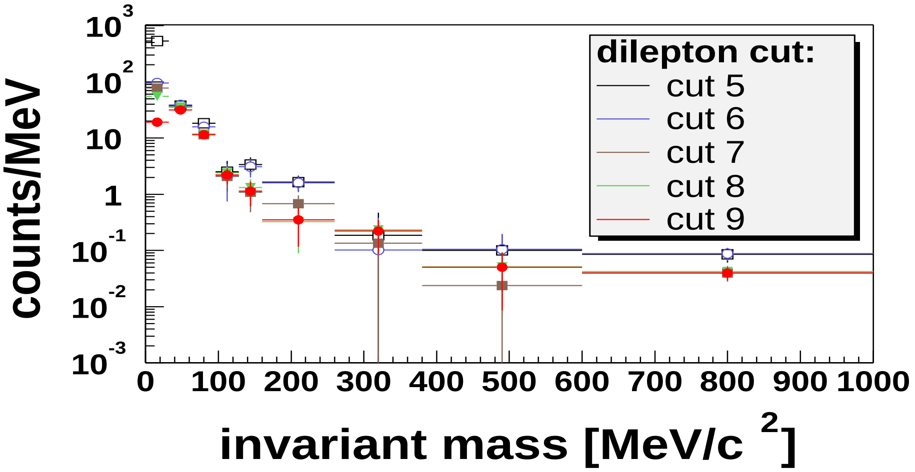

Figure 6.28: The invariant mass spectrum of the reconstructed e^+e^- signal from the analysis of the measured data of C+C at 2 AGeV after each dilepton cut separately. The error in y direction is the statistical error and the line in x direction shows the bin size. The binning is the same as in *Fig.* 6.25. The spectra are divided by the total number of analyzed events and the bin size.

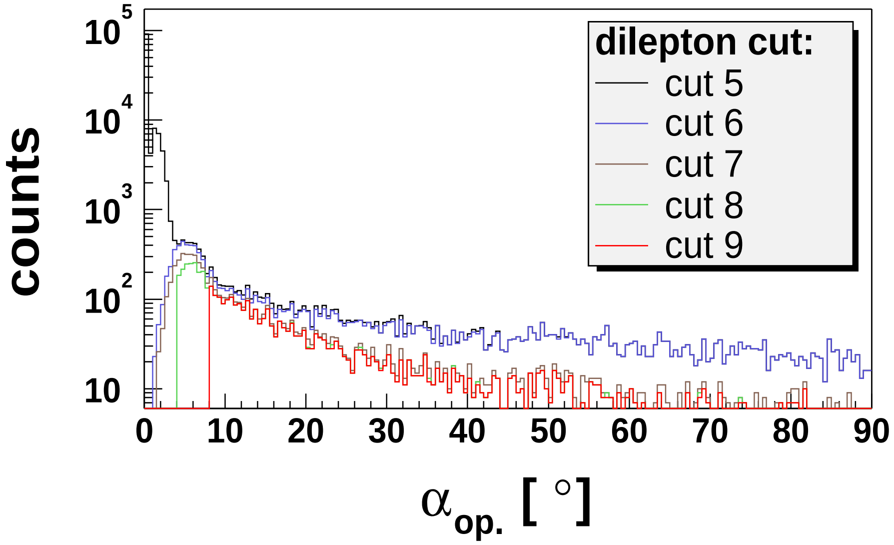

Figure 6.29: The opening angle spectrum of the all e^+e^- pairs from analysis of measured data of C+C at 2 AGeV after each dilepton cut separately.

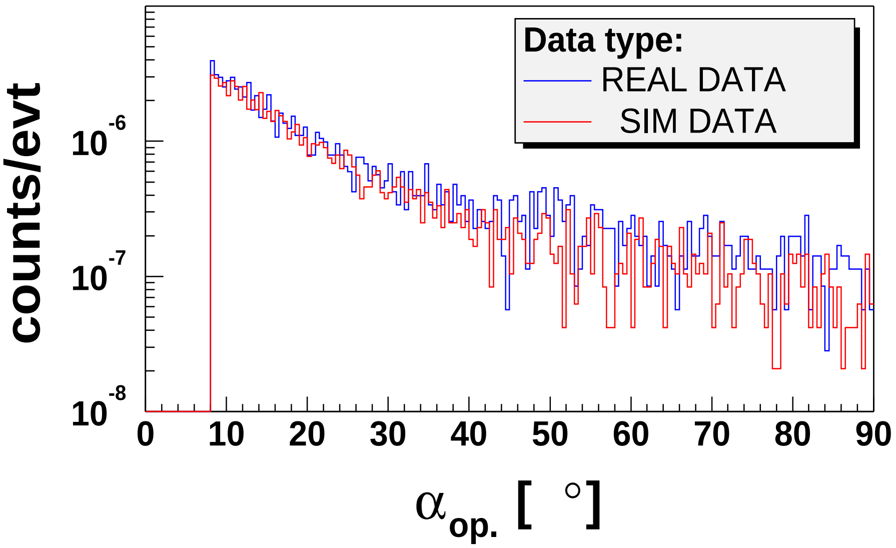

Figure 6.30: The opening angle spectrum of the all e^+e^- pairs from analysis of measured (blue line) and simulated (red line) data of C+C at 2 AGeV. The spectra are normalized to the same π^0 Dalitz pairs yield of the e^+e^- signal after combinatorial background subtraction.

cut level	REAL DATA				SIM DATA				SIM/REAL	
	$N_{e^+e^+}$ $[10^{-5}]$	[%]	$N_{e^-e^-}$ $[10^{-5}]$	[%]	$N_{e^+e^+}$ $[10^{-5}]$	[%]	$N_{e^-e^-}$ $[10^{-5}]$	[%]	e^+e^+	e^-e^-
5	121.8	100.0	203.1	100.0	156.7	100.0	271.3	100.0	1.29	1.34
6	7.2	5.9	13.0	6.4	12.3	7.8	22.8	8.4	1.72	1.75
7	2.9	2.4	4.4	2.2	6.1	3.9	9.3	3.4	2.11	2.10
8	1.7	1.4	3.1	1.5	3.1	2.0	5.8	2.1	1.79	1.89
9	1.3	1.1	2.3	1.1	2.2	1.4	4.3	1.6	1.72	1.89

Table 6.15: The multiplicity of the reconstructed $\mathrm{e^+e^+}$ and $\mathrm{e^-e^-}$ pairs per event for measured and simulated data for November 2001 and the ratio between them.

7

Summary

The dilepton production in the C+C collisions at 2 AGeV measured with the HADES spectrometer during the commissioning beamtime in November 2001 has been investigated. Altogether 45 million events have been selected for analysis. A full scaled simulation with the UrQMD event generator and the HADES geometry has been performed to understand the detector performance. The simulation of the dilepton cocktail from all dilepton sources has also been performed with the Pluto++ generator for HADES beam request proposal.

A lepton analysis strategy has been proposed, developed, tested and applied. The sample of lepton tracks has been identified with high purity of about 90$\%$.

A dilepton analysis strategy has been developed and $\mathrm{e^+e^-}$ pairs have been studied. The combinatorial background has been reconstructed with the like-sign method.

The sources of the combinatorial background have been investigated. As the most important source of combinatorial background the pairs from external γ conversion has been identified. These pairs with small opening angles are mostly unresolved in the RICH and the inner MDC modules. A method for recognition and rejection of the unresolved close pairs has been developed, improving the the S/B ratio of the reconstructed pairs by 100%.

The invariant mass spectrum of $\mathrm{e^+e^-}$ pairs after subtraction of the combinatorial background, constructed with like-sign pairs method, shows a peak for the masses less than 160 $\mathrm{MeV/c^2}$. These pairs have been identified in simulated data as π^0 Dalitz pairs in 89%. There is an additional contribution of 4% from η Dalitz and γ conversion pairs in this peak. This part of the spectrum is for measured data reconstructed with S/B ratio of 2.6. The shape of the reconstructed $\mathrm{e^+e^-}$ invariant mass spectrum in measured and simulated data is within error bars identical. However the yield of the reconstructed pairs in the π^0 Dalitz invariant mass region is a factor 2.8 smaller in measured data than in simulated data.

The spectrum of reconstructed pairs with invariant masses from 160$\mathrm{MeV/c^2}$ to 600 $\mathrm{MeV/c^2}$ does not differ within the error bars in shape, nor yield between measured and simulated data. The S/B ratio in this region is 1:4. About 25% of the reconstructed yield corresponds to expected signal from η pairs in simulated data. The large error bars in this region of invariant mass spectrum, due to small statistics, can not give unambiguous information about possible differences related to a dilepton enhancement.

The detector performance and analysis efficiency in simulated data do not describe the measured performance with sufficient precision. The observed difference of the yield is subject for further investigations.

The reconstructed invariant mass spectrum shows clear signatures that it is dominated by the π^0 Dalitz pairs. The investigation of the other part of the spectra is the prime focus of the analysis from November 2002 beamtime with factor 20 larger statistics and the high momentum resolution set up. Present data do not allow direct comparison to DLS data, however it seems that it does not support factor 10 enhancement of the η yield over UrQMD, that it is necessary to describe the DLS data.

The measurement of elementary reactions with proton beams brings the possibility to determine directly the efficiencies of the HADES detectors via $pp \rightarrow pp\pi^0$ and $pp \rightarrow pp\eta$ reactions. The analysis of high-resolution data (from November 2002 beamtime) will also shed new light on this problematic.

Appendix A

Single lepton spectra for TOF and TOFINO

In this appendix the single lepton spectra from the analysis of measured and simulated data are presented separately for each META subsystem after all lepton cuts. For the measured data also spectra after each lepton cut are shown. For definition of the lepton cuts, see *Tab.6.1* in *Chapter 6*.

In *Fig. A.1* and *Fig. A.2* the comparison of measured and simulated polar and azimuthal angles, respectively is shown. In *Fig. A.3* and *Fig. A.4* the lepton polar and azimuthal angle distributions are shown after each lepton cut of the analysis for measured data.

Most of the fake combinations of the MDC-META track pieces with a hot spot on the RICH pad plane, that produced more fake rings with $\theta \backsimeq 50^{\circ}$ and $\phi \backsimeq 350^{\circ}$, are removed after applying all the cuts (red line) .

In *Fig. A.6* the comparison of the momentum of measured and simulated leptons is displayed. In *Fig. A.5* momentum spectra are shown after each lepton cut for measured data. The contamination from high momentum hadrons is significantly reduced after all cuts are applied, especialy for the positrons.

In *Fig. A.7* and *Fig. A.8* the polar angle versus azimuthal angle and polar angle versus momentum spectra are shown for measured leptons after all cuts.

The rapidity and transverse momentum spectra of measured and simulated data are shown in *Fig. A.12* and *Fig. A.11*, respectively. These spectra after each step of analysis for measured data are shown in *Fig. A.10* and *Fig. A.9*.

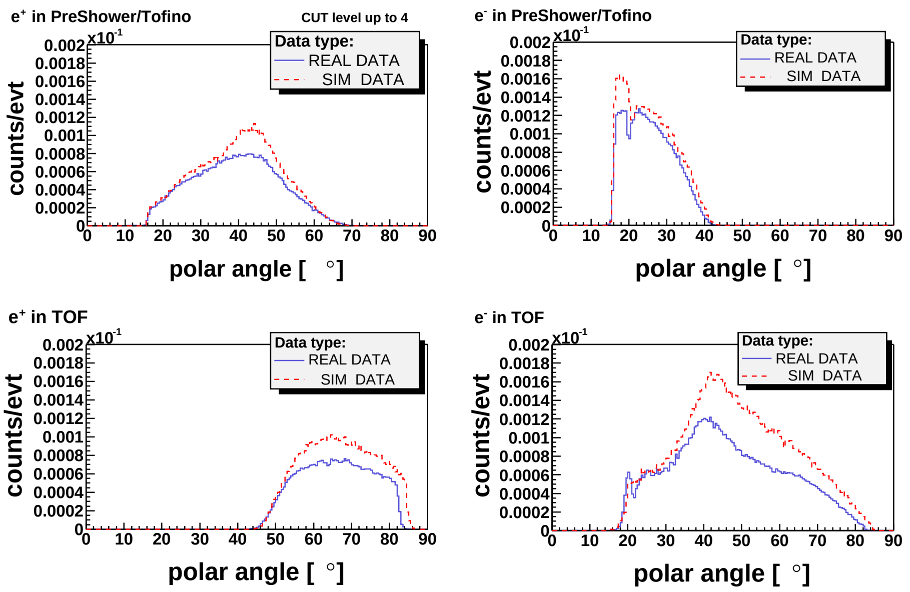

Figure A.1: The azimuthal angle distribution of e^- and e^+ from analysis of measured and simulated data for TOF and PreShower/TOFINO systems separately for candidates after applying all lepton cuts.

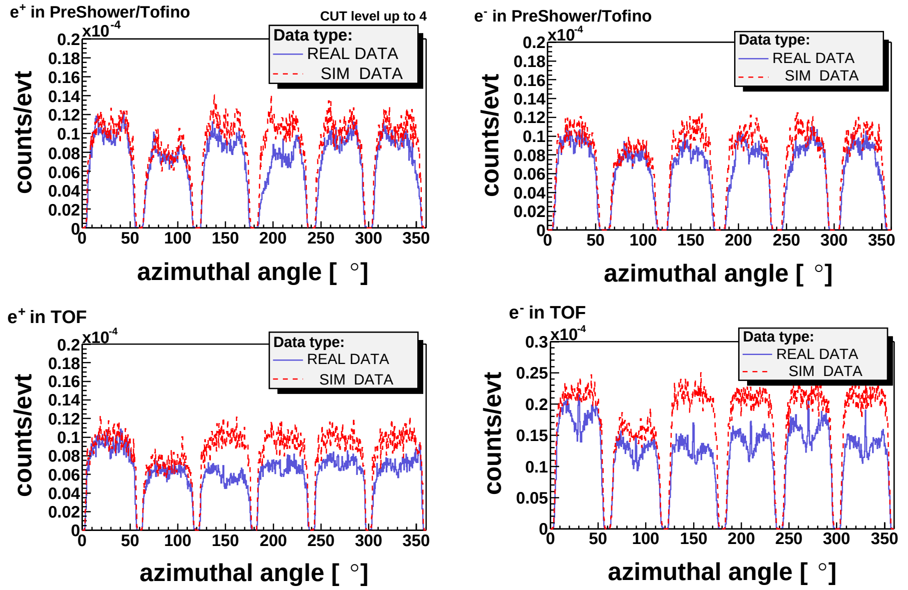

Figure A.2: The polar angle distribution of e^- and e^+ from analysis of measured and simulated data for TOF and PreShower/TOFINO systems separately for candidates after applying all lepton cuts.

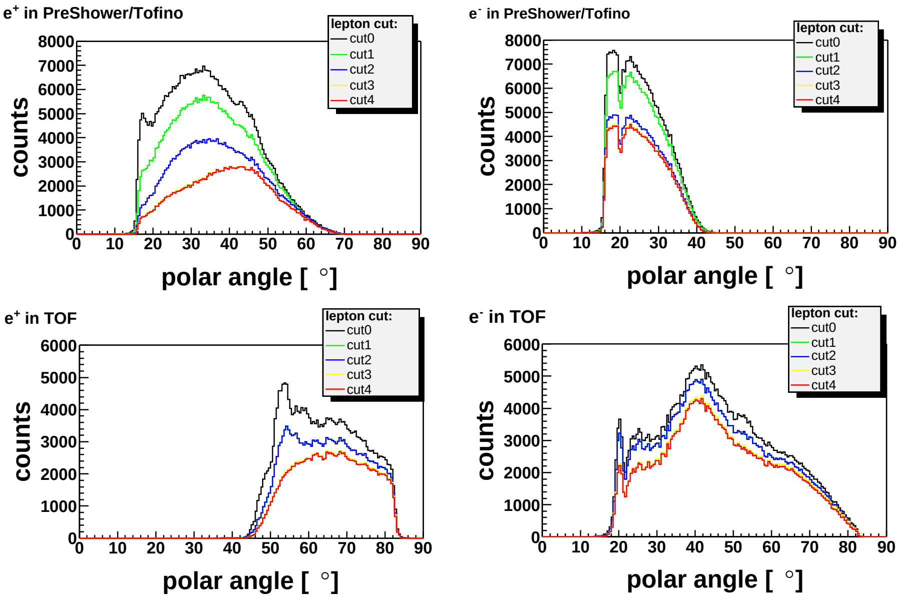

Figure A.3: The azimuthal angle distribution of e$^-$ and e$^+$ from analysis of measured data for TOF and PreShower/TOFINO systems separately for each analysis step.

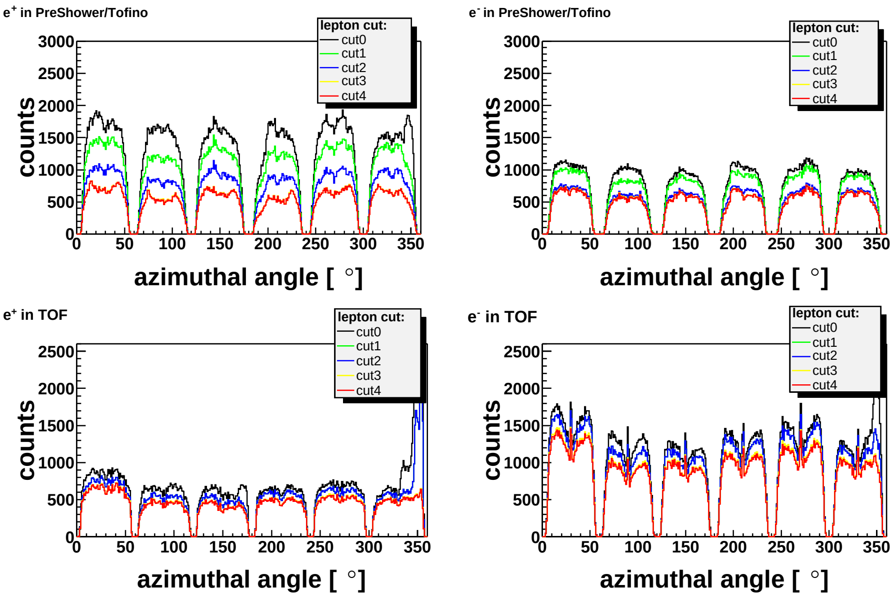

Figure A.4: The polar angle distribution of e$^-$ and e$^+$ from analysis of measured data for TOF and PreShower/TOFINO systems separately for each analysis step.

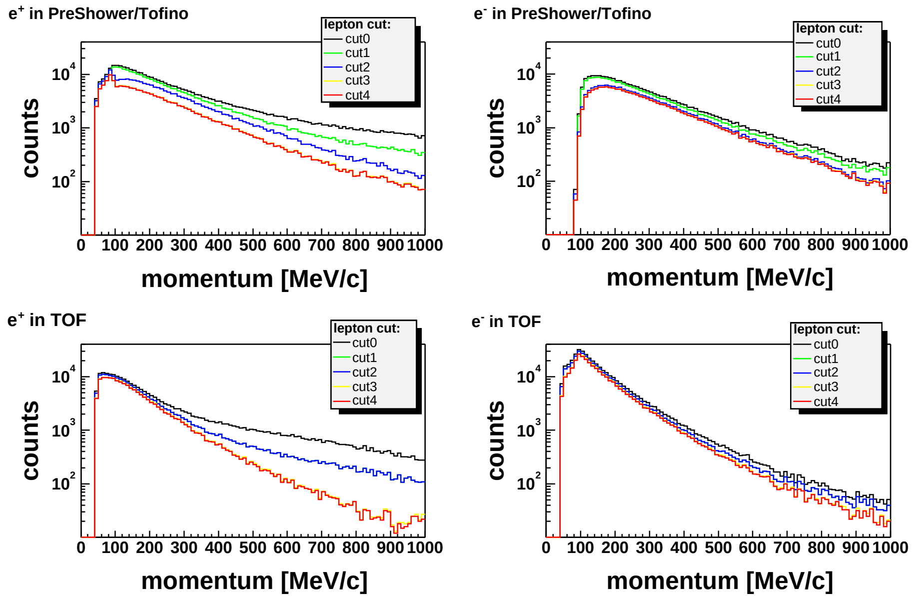

Figure A.5: The momentum distribution of e$^-$ and e$^+$ from analysis of measured data for TOF and PreShower/TOFINO systems separately for each analysis step.

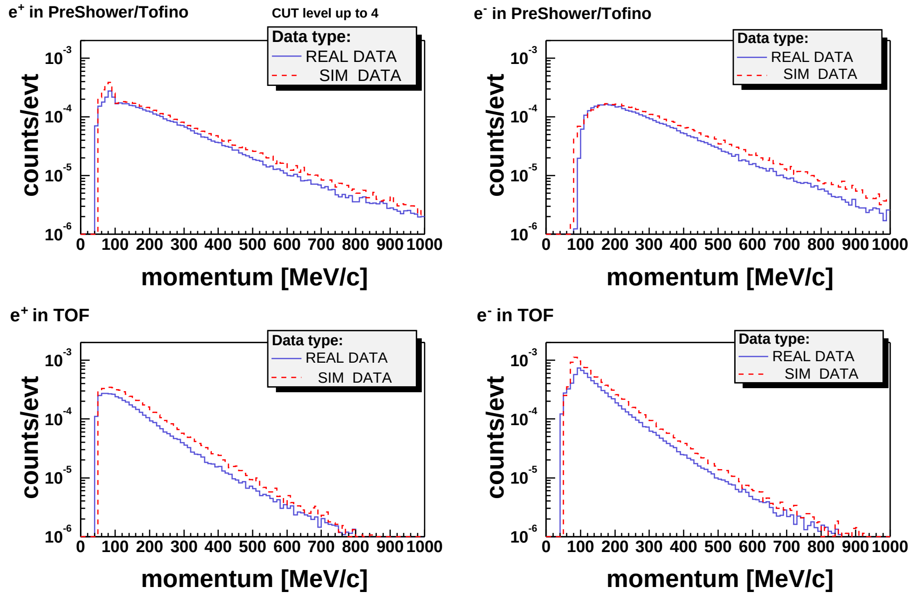

Figure A.6: The momentum distribution of e$^-$ and e$^+$ from analysis of measured and simulated data for TOF and PreShower/TOFINO systems separately for candidates after applying all lepton cuts.

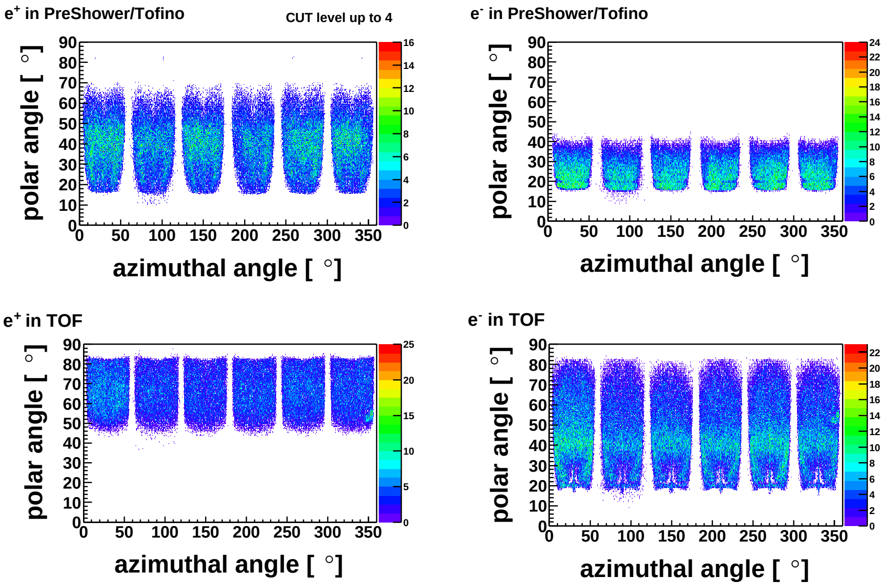

Figure A.7: The azimuthal versus polar angle distribution of e^- and e^+ from analysis of measured data for TOF and PreShower/TOFINO systems separately for candidates after applying all lepton cuts.

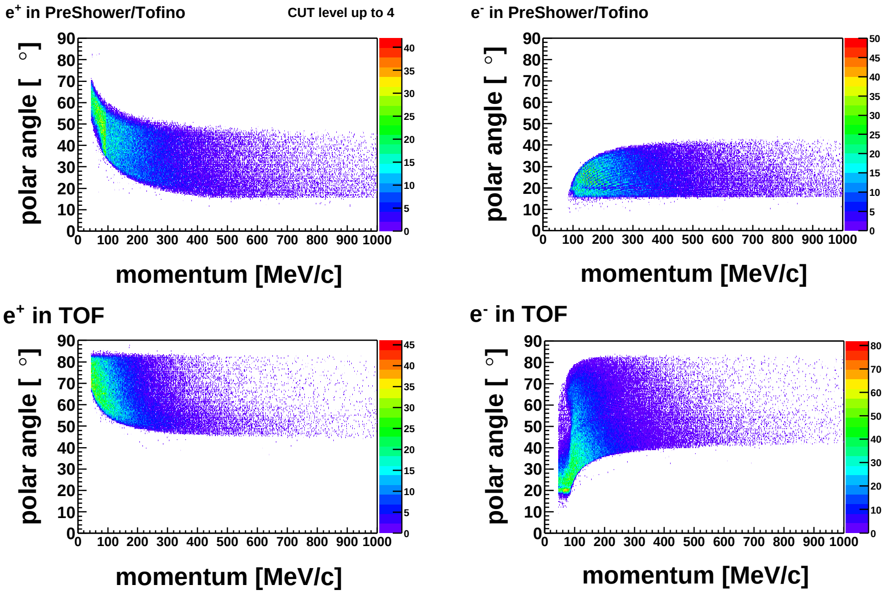

Figure A.8: The azimuthal angle versus momentum distribution of e^- and e^+ from analysis of measured data for TOF and PreShower/TOFINO systems separately for candidates after applying all lepton cuts.

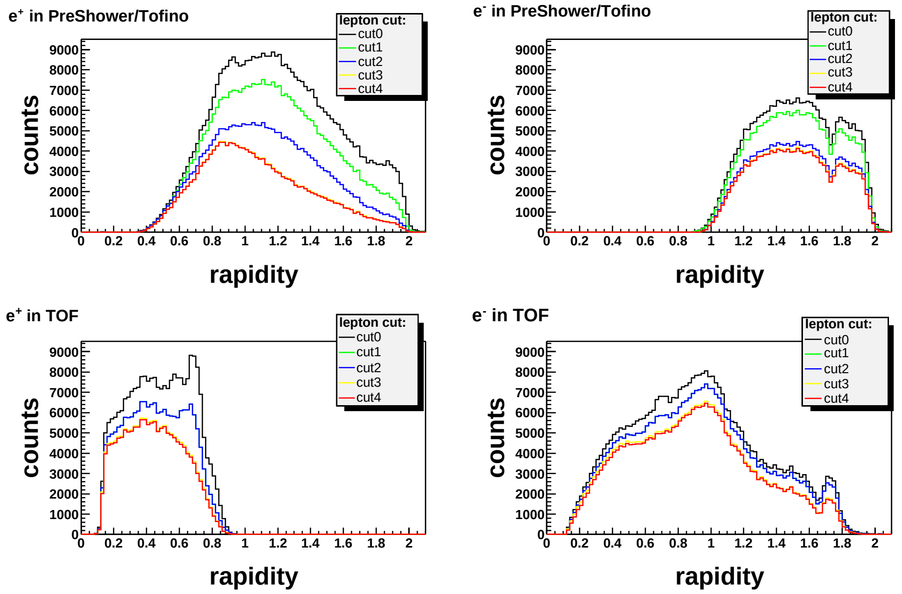

Figure A.9: The transverse momentum distribution of e$^-$ and e$^+$ from analysis of measured data for TOF and PreShower/TOFINO systems separately for candidates after each analysis cut.

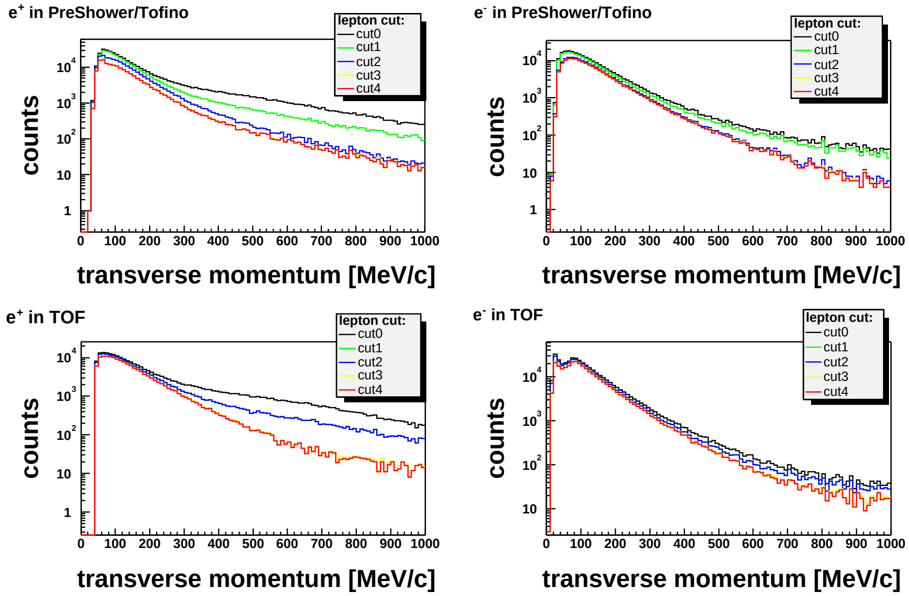

Figure A.10: The rapidity distribution of e$^-$ and e$^+$ from analysis of measured data for TOF and PreShower/TOFINO systems separately for candidates after each analysis cut.

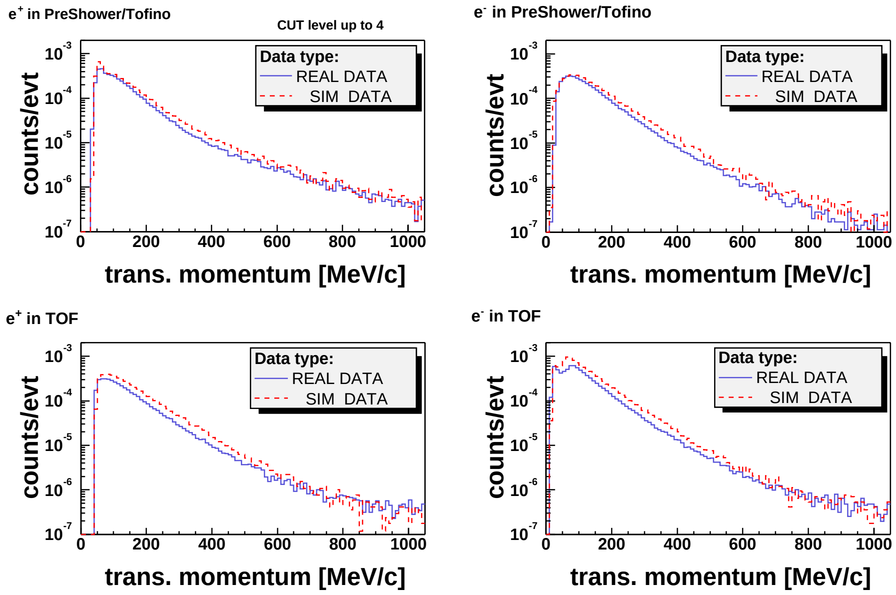

Figure A.11: The transverse momentum distribution of e$^-$ and e$^+$ from analysis of measured and simulated data for TOF and PreShower/TOFINO systems separately for candidates after all lepton analysis cuts.

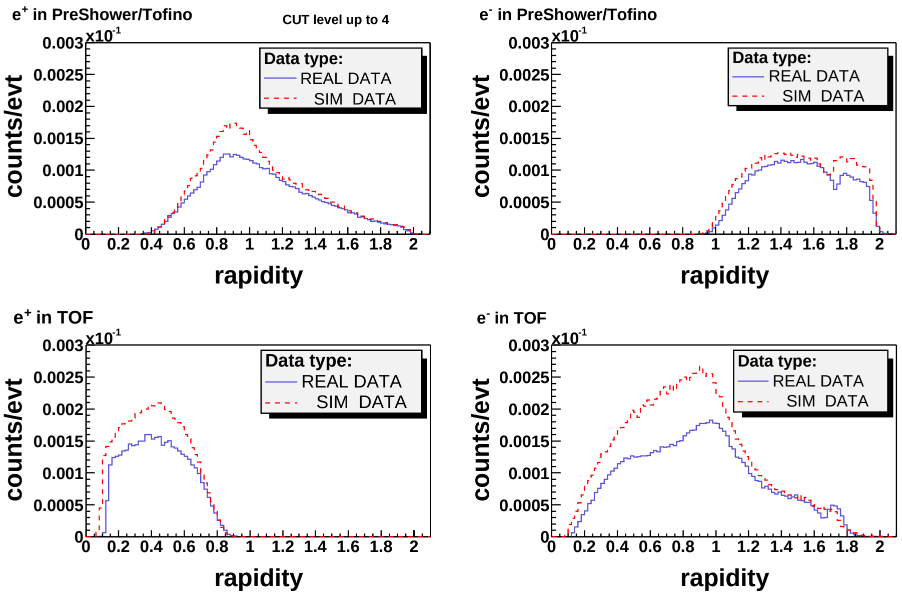

Figure A.12: The rapidity distribution of e$^-$ and e$^+$ from analysis of measured and simulated data for TOF and PreShower/TOFINO systems separately for candidates after all lepton analysis cuts.

Bibliography

[1] R. Rapp and J. Wambach, *Chiral symmetry restoration and dileptons in relativistic heavy-ion collisions,* Adv. Nucl. Phys. **25**, 1 (2000), hep-ph/9909229.

[2] G. E. Brown and M. Rho, *Scaling effective Lagrangians in a dense medium,* Phys. Rev. Lett. **66**, 2720 (1991).

[3] B. Friman and H. J. Pirner, *P-wave polarization of the rho meson and the dilepton spectrum in dense matter,* Nucl. Phys. **A617**, 496 (1997), nucl-th/9701016.

[4] S. A. Bass *et al.*, *Microscopic models for ultrarelativistic heavy ion collisions,* Prog. Part. Nucl. Phys. **41**, 225 (1998), nucl-th/9803035.

[5] W. Ehehalt, W. Cassing, A. Engel, U. Mosel, and G. Wolf, *Resonance properties in nuclear matter,* Phys. Rev. **C47**, 2467 (1993).

[6] K. Hagiwara *et al.* (Particle Data Group Collaboration), *Review of particle physics,* Phys. Rev. **D66**, 010001 (2002).

[7] W. Cassing and E. L. Bratkovskaya, *Hadronic and electromagnetic probes of hot and dense nuclear matter,* Phys. Rept. **308**, 65 (1999).

[8] G. Wolf *et al.*, *Dilepton production in heavy ion collisions,* Nucl. Phys. **A517**, 615 (1990).

[9] G. Roche *et al.* (DLS Collaboration), *DIELECTRON PRODUCTION IN Ca + Ca COLLISIONS AT 1-A/GeV AND 2-A/GeV,* Phys. Lett. **B226**, 228 (1989).

[10] L. Xiong, Z. G. Wu, C. M. Ko, and J. Q. Wu, *Dielectron production from nucleus-nucleus collisions,* Nucl. Phys. **A512**, 772 (1990).

[11] W. Cassing *et al.*, *Energetic particle production in heavy ion collisions,* Prepared for Workshop on Physics Related to TAPS, Schiermonnikoog, Germany, 10-14 Sep 1990.

[12] V. D. Toneev, A. I. Titov, and K. K. Gudima, *Hadronic sources of dileptons from nuclear collisions at intermediate-energies and relativistic energies,* Phys. Lett. **B287**, 302 (1992).

[13] E. L. Bratkovskaya, W. Cassing, and U. Mosel, *Dilepton anisotropy from $p + Be$ and $Ca + Ca$ collisions at BEVALAC energies,* Phys. Lett. **B376**, 12 (1996), nucl-th/9601018.

[14] R. J. Porter *et al.* (DLS Collaboration), *Dielectron cross section measurements in nucleus nucleus reactions at 1.0-A-GeV,* Phys. Rev. Lett. **79**, 1229 (1997), nucl-ex/9703001.

[15] E. L. Bratkovskaya and C. M. Ko, *Low-mass dileptons and dropping rho meson mass,* Phys. Lett. **B445**, 265 (1999), nucl-th/9809056.

[16] W. Ehehalt and W. Cassing, *Relativistic transport approach for nucleus nucleus collisions from SIS to SPS energies,* Nucl. Phys. **A602**, 449 (1996).

[17] E. L. Bratkovskaya, W. Cassing, R. Rapp, and J. Wambach, *Dilepton production and m(T)-scaling at BEVALAC/SIS energies,* Nucl. Phys. **A634**, 168 (1998), nucl-th/9710043.

[18] K. Shekhter, C. Fuchs, A. Faessler, M. Krivoruchenko, and B. Martemyanov, *Dilepton production in heavy ion collisions at intermediate energies,* Phys. Rev. **C68**, 014904 (2003), nucl-th/0305015.

[19] C. Ernst, S. Bass, M. Belkacem, H. Stocker, and W. Greiner, *Intermediate mass excess of dilepton production in heavy ion collisions at relativistic energies,* Phys. Rev. **C58**, 447 (1998).

[20] R. Holzmann *et al.* (TAPS Collaboration), *Contribution of pi^0 and η Dalitz decays to the dilepton invariant-mass spectrum in 1-A-GeV heavy-ion collisions,* Phys. Rev. **C56**, 2920 (1997).

[21] H.Schoen, *HADES ,Ein Dielektronenspektrometer hoher Akzeptanz fur relatovistische Schwerionenkollisionen.,* PhD thesis, University of Frankfurt, 1995.

[22] K. Zeitelhack *et al.* (HADES Collaboration), *The HADES RICH detector,* Nucl. Instrum. Meth. **A433**, 201 (1999).

[23] W. Przygoda, *Identyfikacja czstek e+/e- za pomoca detektora RICH w spektrometrze HADES,* PhD thesis, University of Krakow, 2002.

[24] J. Markert, *Dilepton spectroscopy with HADES Spectrometer,* PhD thesis, University of Frankfurt, 2004.

[25] C. Garabatos *et al.*, *Optimisation of low-mass drift chambers for HADES,* Nucl. Instrum. Meth. **A412**, 38 (1998).

[26] C. Muentz, *The Di-Electron Spectrometer HADES at GSI: a Status Report,* Nucl.Phys. **B78** (1999).

[27] T. Bretz, *Magnetfeldeigenschaften des Spektrometers HADES*, Diploma thesis, TU Muenchen, 1999.

[28] C. Agodi *et al.*, *The HADES time-of-flight wall*, Nucl. Instrum. Meth. **A492**, 14 (2002).

[29] P. Tlusty, Hades trigger., Privat communication.

[30] R. Brun *et al.*, *GEANT*.

[31] M. Kargalis, *Pluto++*, GSI Report, 2000-03.

[32] T. Schuck, *Pionenproduktion in Au+Au-Stossen bei 1.5 AGeV im Experiment und im UrQMD-Modell*, Diploma thesis, Johann Wolfgang Goethe-Universitet Frankfurt/Main, 2002.

[33] R. Averbeck *et al.* (TAPS Collaboration), *Production of pi0 and eta mesons in carbon-induced relativistic heavy ion collisions*, Z. Phys. **A359**, 65 (1997).

[34] M. Sudol, *Dilepton production in C+C at 2AGeV*, PhD thesis, University of Frankfurt, 2004.

[35] E. Schnedermann, J. Sollfrank, and U. W. Heinz, *Thermal phenomenology of hadrons from 200-A/GeV S+S collisions*, Phys. Rev. **C48**, 2462 (1993), nucl-th/9307020.

[36] R. Brun and F. Rademakers, *ROOT: An object oriented data analysis framework*, Nucl. Instrum. Meth. **A389**, 81 (1997).

[37] L. Fabietti, *Studies of the e+e- pair acceptance in the dilepton spectrometer HADES.*, PhD thesis, TU Muenchen, 2003.

[38] J. Otwinowski, *Pomiar widm par e+e- wyprodukowanych przy energii* $E_{kin} \leq 2\ AGeV$ *przy pomocy sepktrometru HADES.*, PhD thesis, IF UJ Krakow, 2003.

[39] J. Friese, Dilepton production in cc and πp reactions., HADES proposal, 2001.

[40] J. Stachel and G. R. Young, *Relativistic heavy ion physics at CERN and BNL*, Ann. Rev. Nucl. Part. Sci. **42**, 537 (1992).

[41] R. Holzmann, Private communication, The temperature of thermal source for CC collision at 1 A GeV and 2 A GeV.

[42] R.Holzmann, The π^0 and η production as function of collision system., Privat communication.

[43] A. R. Wolf *et al.*, *Multistep production of eta and hard pi0 mesons in subthreshold Au Au collisions*, Phys. Rev. Lett. **80**, 5281 (1998).

[44] F. D. Berg *et al.*, *Transverse momentum distributions of eta mesons in near threshold relativistic heavy ion reactions,* Phys. Rev. Lett. **72**, 977 (1994).

[45] A. Marin *et al.*, *Exclusive pi0- and eta-meson production in Ar-40 + Ca-nat at 800-A-MeV,* Phys. Lett. **B409**, 77 (1997).

[46] R. Averbeck, R. Holzmann, V. Metag, and R. Simon, *Neutral pions and eta mesons as probes of the hadronic fireball in nucleus-nucleus collisions around 1 AGeV,* Phys. Rev. **C67** (2003).

[47] G. Hering, *Dielectron production in heavy-ion collisions at 158 GeV/c per nucleon,* PhD thesis, Technical University Darmstadt, Germany, 2002.

[48] M. Gazdzicki and M. I. Gorenstein, *Background subtraction from the dilepton spectra in nuclear collisions,* (2000), hep-ph/0003319.

[49] H. A. Pol, *On the Multiwire Drift Chambers alignment of the HADES dilepton spectrometer,* PhD thesis, The University of Santiagio de Compostela, 2002.

[50] M. S. Garcia, *Momentum Reconstruction and Pion Production Analysis in the HADES Spectrometer at GSI,* PhD thesis, The University of Santiagio de Compostela, 2003.

[51] P. Zumbruch, *Thesis in preparation,* PhD thesis, TU Darmstadt, 2004.

Acknowledgements

At this place, I would like to express my gratitude to many people who have been important for me during this work.

Foremost, I am deeply thankful to Prof.Dr. Peter Braun-Munzinger for being a supervisor and for inviting me to work in the HADES collaboration. His interest and experience helped me to make the research interesting and enjoyable.

I would like to thank Andrej Kugler who induced my interest in the field of heavy ion physics.

Next, I would like to thank my closest consultants, Romain Holzmann and Joachim Stroth for their support during my research. Especially, I am thankful to Romain Holzmann for introducing me to the HADES analysis and simulation. I am thankful for his patience, encouraging words and willingness to recompile the HYDRA one more time. I would like to thank Joachim Stroth for his invitation to work with the MDC group and his interest in close pairs in the chambers. I thank them also for carefully reading the manuscript.

I would like to thank also the other members of the HADES crew, Wolfgang Koenig, Prof.Dr. Herbert Stroebele, Prof. Helmut Bokemeyer, Christian Müntz, Christian Sturm, Ilse Koenig, Burkhard Kolb and Reinhard Simon, that they did not mind to suffer hearing my regular presentation about DST, leptons and close pairs during the group meetings at GSI. I am thankful for their interest and support.

For nice working atmosphere, cheerful spirit, teaching me the language and culture of W.Goethe and S.Raab, many encouraging words, I would like to thank my colleagues with whom I shared the room during my studies: Jochen Markert, Peter Zumbruch, Jörn Wüstenfeld, Klaus Rosenkranz, Yvonne Pachmayer, Anar Rustamov, Thomas Bretz, Christian Lippmann, Walter Schön and Walter Karig.

I thank also the other HADES students at GSI Darmstadt, especially Gosia Sudol that she joined the jogging lunch breaks and Katarzyna Tyminska that she always made a friendly smile, anytime I met her. I would like also to thank Denis Bertini (alias Mr.DeBug) for great help with debugging my code.

I would like also to thank the other HADES members for their support, mainly Laura Fabbietti, Thomas Eberl and Jacek Otwinowski.

Last but not least, I want to thank my wife Jana and my family for their love, constant support and patience.

It was a long and difficult way to go from the first simulations of C+C at 2 AGeV that I have done in 1998, when the HADES cave was still an empty hall, to the first dilepton spectra short after the beamtime of November 2001 and finally to the encouraging results presented in this work. It was a honour to be a part of it.

Resume

Name: Bielcik, Jaroslav

Date of Birth: July 27, 1973 - Hnusta-Likier, Slovakia

Address:

Gesellschaft für Schwerionenforschung mbH
Planckstrasse 1
D-64921 , Germany
Tel.: +49 6159 712885
Email: J.Bielcik@gsi.de

Education:

1/99 - present	Technical University of Darmstadt · Ph.D. in Physics · Title of Thesis: Dilepton spectroscopy with HADES, advisor: Prof. Peter Braun-Munzinger
9/95 - 12/97	University of Bergen, Norway · Master of Science · Major: Physics, Concentration: Theoretical physics · Title of Thesis: Atoms in the intense laser fields, advisor: Prof. Ladislav Kocbach
9/91 - 6/97	Charles University,Prague, Czech Republic · Diplom in Physics · Major: Physics, Concentration: Nuclear physics · Title of Thesis: The study of ^{99}Ru nucleus by the methods of in-beam spectroscopy, advisor: Dr. Milan Honusek
9/87 - 6/91	Special school for mathematics at Banska Bystrica, Slovakia (senior high school) · School leaving examinations with HONOR

Darmstadt, December 12, 2003